

## Monte Carlo model for analysis of thermal runaway electrons in streamer tips in transient luminous events and streamer zones of lightning leaders

Gregory D. Moss,<sup>1</sup> Victor P. Pasko,<sup>1</sup> Ningyu Liu,<sup>1</sup> and Georgios Veronis<sup>2</sup>

Received 3 August 2005; revised 9 October 2005; accepted 16 November 2005; published 16 February 2006.

[1] Streamers are thin filamentary plasmas that can initiate spark discharges in relatively short (several centimeters) gaps at near ground pressures and are also known to act as the building blocks of streamer zones of lightning leaders. These streamers at ground pressure, after  $1/N$  scaling with atmospheric air density  $N$ , appear to be fully analogous to those documented using telescopic imagers in transient luminous events (TLEs) termed sprites, which occur in the altitude range 40–90 km in the Earth's atmosphere above thunderstorms. It is also believed that the filamentary plasma structures observed in some other types of TLEs, which emanate from the tops of thunderclouds and are termed blue jets and gigantic jets, are directly linked to the processes in streamer zones of lightning leaders. Acceleration, expansion, and branching of streamers are commonly observed for a wide range of applied electric fields. Recent analysis of photoionization effects on the propagation of streamers indicates that very high electric field magnitudes  $\sim 10 E_k$ , where  $E_k$  is the conventional breakdown threshold field defined by the equality of the ionization and dissociative attachment coefficients in air, are generated around the tips of streamers at the stage immediately preceding their branching. This paper describes the formulation of a Monte Carlo model, which is capable of describing electron dynamics in air, including the thermal runaway phenomena, under the influence of an external electric field of an arbitrary strength. Monte Carlo modeling results indicate that the  $\sim 10 E_k$  fields are able to accelerate a fraction of low-energy (several eV) streamer tip electrons to energies of  $\sim 2$ – $8$  keV. With total potential differences on the order of tens of MV available in streamer zones of lightning leaders, it is proposed that during a highly transient negative corona flash stage of the development of negative stepped leader, electrons with energies 2–8 keV ejected from streamer tips near the leader head can be further accelerated to energies of hundreds of keV and possibly to several tens of MeV, depending on the particular magnitude of the leader head potential. It is proposed that these energetic electrons may be responsible (through the “bremsstrahlung” process) for the generation of hard X rays observed from ground and satellites preceding lightning discharges or with no association with lightning discharges in cases when the leader process does not culminate in a return stroke. For a lightning leader carrying a current of 100 A, an initial flux of  $\sim 2$ – $8$  keV thermal runaway electrons integrated over the cross-sectional area of the leader is estimated to be  $\sim 10^{18} \text{ s}^{-1}$ , with the number of electrons accelerated to relativistic energies depending on the particular field magnitude and configuration in the leader streamer zone during the negative corona flash stage of the leader development. These thermal runaway electrons could provide an alternate source of relativistic seed electrons which were previously thought to require galactic cosmic rays. The duration of the negative corona flash and associated energetic radiation is estimated to be in the range from  $\sim 1 \mu\text{s}$  to  $\sim 1 \text{ ms}$  depending mostly on the pressure-dependent size of the leader streamer zone.

**Citation:** Moss, G., V. P. Pasko, N. Liu, and G. Veronis (2006), Monte Carlo model for analysis of thermal runaway electrons in streamer tips in transient luminous events and streamer zones of lightning leaders, *J. Geophys. Res.*, *111*, A02307, doi:10.1029/2005JA011350.

<sup>1</sup>Communications and Space Sciences Laboratory, Pennsylvania State University, University Park, Pennsylvania, USA.

<sup>2</sup>Ginzton Laboratory, Stanford University, Stanford, California, USA.

### 1. Introduction

#### 1.1. Streamers in Transient Luminous Events and Lightning Leaders

[2] Transient luminous events (TLEs) are large-scale optical events in the Earth's atmosphere that are directly

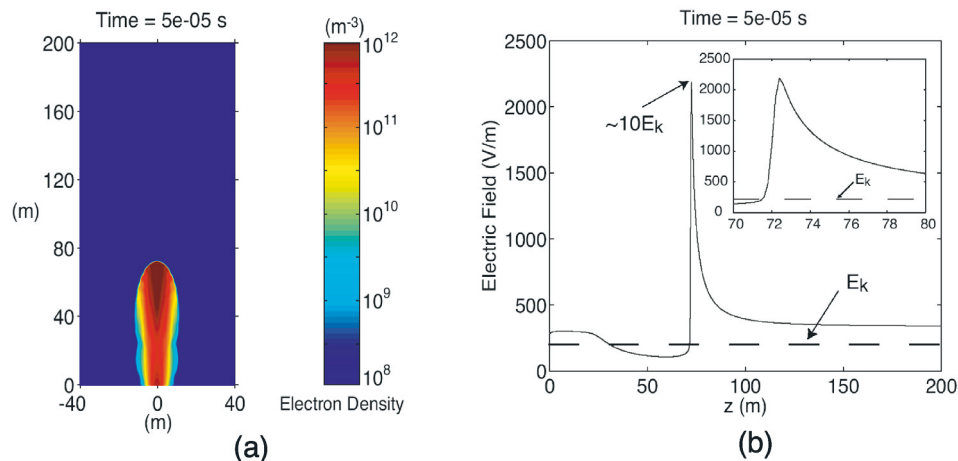


**Figure 1.** (a) A cross-sectional view of the distribution of the electron number density for a model negative streamer at 70 km altitude immediately preceding branching and (b) the electric field in the streamer tip immediately preceding branching.

related to electrical activity in underlying thunderstorms. Several types of TLEs are known: relatively slow-moving fountains of blue light, known as “blue jets,” that emanate from the top of thunderclouds up to an altitude of 40 km [e.g., *Wescott et al.*, 1995, 2001; *Lyons et al.*, 2003]; “sprites” that develop at the base of the ionosphere and move rapidly downward at speeds up to 10,000 km/s [e.g., *Sentman et al.*, 1995; *Lyons*, 1996; *Stanley et al.*, 1999]; “elves,” which are lightning-induced flashes that can spread over 300 km laterally [e.g., *Fukunishi et al.*, 1996; *Inan et al.*, 1997], and recently observed “gigantic jets,” which propagate upward, connecting thundercloud tops with the lower ionosphere [e.g., *Pasko et al.*, 2002; *Su et al.*, 2003].

[3] Since their discovery, there have been numerous imaging campaigns in an effort to better understand the physical phenomena behind these events. Recent imaging campaigns of sprites [*Gerken and Inan*, 2005; *Marshall and Inan*, 2005, and references therein], blue jets [*Wescott et al.*, 2001], and gigantic jets [*Pasko et al.*, 2002] have revealed a wide variety of fine filamentary structures in these events, which have been interpreted as streamers. Streamers are narrow filamentary plasmas, which are driven by highly nonlinear space charge waves [e.g., *Raizer*, 1991, p. 327]. Streamers can exhibit both positive and negative polarities, which is simply defined by the sign of the charge existing in the streamer head. Negative streamers generally propagate in the same direction as the electron drift, whereas positive streamers propagate opposing the electron drift. Negative streamers do not require ambient seed electrons to propagate since electron avalanches originating from the streamer head propagate in the same direction as the streamer [e.g., *Vitello et al.*, 1994; *Rocco et al.*, 2002]. Positive streamers, however, must obtain seed electrons from photoionization to sustain their propagation [e.g., *Dhali and Williams*, 1987; *Raizer*, 1991, p. 335].

[4] Streamers also serve as precursors to a more complicated leader phenomenon, which involves significant heating and thermal ionization of the ambient gas and represents a well known initiation mechanism of break-

down in long gaps [*Raizer*, 1991, p. 363]. Leaders are thin, highly ionized, highly conductive channels which grow along a path prepared by preceding streamers [*Raizer*, 1991, p. 364]. The head of the highly ionized and conducting leader channel is normally preceded by a streamer zone looking as a diverging column of diffuse glow and filled with highly branched streamer coronas [e.g., *Bazelyan and Raizer*, 1998, p. 203, 253]. The leader process is also a well-documented means by which conventional lightning develops in thunderstorms [*Uman*, 2001, p. 82], suggesting the presence of numerous streamers with every lightning discharge.

[5] It has been recently demonstrated that negative streamers developing in high ambient fields can reach an unstable “ideal conductivity” state with approximately equipotential and weakly curved head [*Arrayas et al.*, 2002; *Rocco et al.*, 2002]. This new state exhibits a Laplacian instability which can lead to branching of the streamer [*Arrayas et al.*, 2002; *Rocco et al.*, 2002] and can be realized over a wide range of applied electric fields [*Liu and Pasko*, 2004]. *Liu and Pasko* [2004] also studied the effects of photoionization on the dynamics of streamers and determined that the acceleration and expansion of streamers results in a reduction of the preionization level ahead of the streamers. In order to compensate for this reduction in preionization, the magnitude of the electric field in the streamer tip can reach a value as large as  $10E_k$  at the stage immediately preceding the branching of the streamer, where  $E_k$  is the conventional breakdown threshold field defined by the equality of the ionization and dissociative attachment coefficients in air [e.g., *Raizer*, 1991, p. 135]. Figure 1a shows a negative streamer propagating at an altitude of 70 km in a  $1.5E_k$  ambient field as it reaches an unstable state just prior to branching. It can be seen in Figure 1b that an extremely high electric field exists in the streamer tip prior to branching. This high field  $\sim 2$  kV/m, which spans approximately 1 m (see Figure 1b), could possibly accelerate low-energy electrons ( $\sim$ several eV) to very high energies  $\sim 2$  keV. As discussed in the next section, the acceleration of electrons in these highly overvolted streamer tips could contribute to the

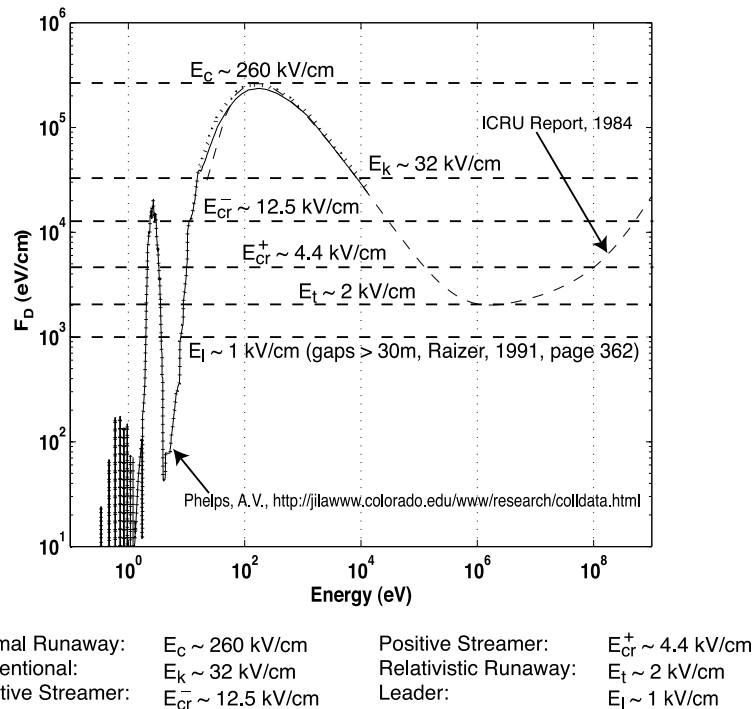


**Figure 2.** The dynamic friction force of electrons in air at ground pressure is plotted as a function of electron energy. A solid line corresponds to a case when a total of 43 inelastic processes were accounted for corresponding to an air mixture of 78.11%  $N_2$ , 20.91%  $O_2$  and .98%  $Ar$  gases using a set of cross sections compiled by A. V. Phelps (<http://jilawww.colorado.edu/www/research/colldata.html>), which excludes dissociation processes. A dotted line corresponds to a case which includes energy losses due to dissociation of  $N_2$  and  $O_2$  molecules.

formation of high-energy electron fluxes needed to explain the recently observed X-ray [Moore *et al.*, 2001; Dwyer *et al.*, 2003, 2004a, 2004b, 2005] and gamma ray [Fishman *et al.*, 1994; Smith *et al.*, 2005] bursts associated with thunderstorm activity.

[6] The model streamer shown in Figure 1 was obtained using the numerical model described by Liu and Pasko [2004] and assuming that no preionization is produced ahead of the streamer due to photoionization effects. These conditions are expected to be close to those realized before streamer branching when the photoionization range becomes shorter than the radius of the expanding streamer (see sections 4.1 and 4.4 in the work of Liu and Pasko [2004] for additional details).

## 1.2. Runaway Electrons and Energetic Radiation

[7] Runaway electrons were discussed by Gurevich [1961] and were defined by Kunhardt *et al.* [1986], who stated “an electron is runaway if it does not circulate through all energy states available to it at a given  $E/N$ , but on average moves toward high-energy states.” The runaway phenomenon is a result of decreasing probability of electron interactions with atomic particles for electron energies in the range from  $\sim 100$  eV to  $\sim 1$  MeV [Gurevich, 1961]. This phenomenon can best be understood by considering the dynamic friction force of electrons in air as a function of electron energy (see Figure 2):

$$F_D(\epsilon) = \sum_j N_j \sigma_j(\epsilon) \delta\epsilon_j, \quad (1)$$

where the summation is performed over all inelastic collision processes of a given gas with partial density  $N_j$  of  $N_2$ ,  $O_2$ , or  $Ar$  in air (in  $m^{-3}$ ) corresponding to a particular collision process defined by the cross section  $\sigma_j$  and energy loss  $\delta\epsilon_j$ . In plotting  $F_D(\epsilon)$  (Figure 2), electron-neutral collision cross sections provided by Phelps (<http://jilawww.colorado.edu/www/research/colldata.html>) and mass radiative and collision stopping powers [International Commission on Radiation Units and Measurements, 1984] were used. Electron energy losses due to nonzero energies of secondary electrons emerging from ionizing collisions with  $N_2$ ,  $O_2$ , and  $Ar$  were accounted for using the differential ionization cross sections provided by Opal *et al.* [1971] (see section 2.3).

[8] Electrons under the influence of an electric field  $\mathbf{E}$  experience a force  $\mathbf{F}_E = -q_e \mathbf{E}$  and an acceleration  $\frac{d\mathbf{v}}{dt}$  according to the Lorentz force law and Newton’s second law, respectively, where  $q_e$  is the absolute value of electron charge. As the electron accelerates through a gas it experiences collisions with the neutral gas molecules and atoms, which give rise to the dynamic friction force  $\mathbf{F}_D$  opposing the force applied by the electric field  $\mathbf{F}_E$ . It can be seen in Figure 2 that the friction force  $\mathbf{F}_D$  varies considerably with electron energy. For example, a maximum exists in  $\mathbf{F}_D$  at  $\sim 100$  eV which is  $\sim 10^3$  the value of  $\mathbf{F}_D$  at 1 eV. Physically speaking, a 100 eV electron experiences many more collisions and loses much more energy per unit length of its trajectory than does a 1 eV electron.

[9]  $\mathbf{F}_D$  has units of eV/cm and can be directly compared to the applied electric field to provide an intuitively simple

**Table 1.** Molecular Nitrogen Collision Processes

Collision Process	Reaction	Threshold Energy, eV
N <sub>2</sub> elastic	$e + N_2 \rightarrow e + N_2$	-
N <sub>2</sub> rotational	$e + N_2 \rightarrow e + N_2(\text{rot})$	0.02
N <sub>2</sub> vibrational	$e + N_2 \rightarrow e + N_2(v=1)$	0.29
	$e + N_2 \rightarrow e + N_2(v=1)$	0.291
	$e + N_2 \rightarrow e + N_2(v=2)$	0.59
	$e + N_2 \rightarrow e + N_2(v=3)$	0.88
	$e + N_2 \rightarrow e + N_2(v=4)$	1.17
	$e + N_2 \rightarrow e + N_2(v=5)$	1.47
	$e + N_2 \rightarrow e + N_2(v=6)$	1.76
	$e + N_2 \rightarrow e + N_2(v=7)$	2.06
	$e + N_2 \rightarrow e + N_2(v=8)$	2.35
	N <sub>2</sub> electronic	$e + N_2 \rightarrow e + N_2(A^3\Sigma_u^+, v=1-4)$
$e + N_2 \rightarrow e + N_2(A^3\Sigma_u^+, v=5-9)$		7.00
$e + N_2 \rightarrow e + N_2(B^3\Pi_u)$		7.35
$e + N_2 \rightarrow e + N_2(W^3\Delta_u)$		7.36
$e + N_2 \rightarrow e + N_2(A^3\Sigma_u^+, v=10+)$		7.80
$e + N_2 \rightarrow e + N_2(B^3\Sigma_u^-)$		8.16
$e + N_2 \rightarrow e + N_2(a^1\Sigma_u^-)$		8.40
$e + N_2 \rightarrow e + N_2(a^1\Pi_g)$		8.55
$e + N_2 \rightarrow e + N_2(w^1\Delta_u)$		8.89
$e + N_2 \rightarrow e + N_2(C^3\Pi_u)$		11.03
$e + N_2 \rightarrow e + N_2(E^3\Sigma_g^-)$		11.88
$e + N_2 \rightarrow e + N_2(a''^1\Sigma_g^+)$		12.25
N <sub>2</sub> sum of singlet states	$e + N_2 \rightarrow e + N_2^*$	13.00
N <sub>2</sub> ionization	$e + N_2 \rightarrow e + e + N_2^+(X^2\Sigma_g^+ + A^2\Pi_u)$	15.60

insight into the expected motion of electrons at various energies. Figure 2 lists electric fields required to initiate various types of electrical breakdown in air (more details and related references may be found in the work of Pasko [2006]) and displays the respective force  $F_E$ , in units of eV/cm, they apply to electrons in relationship to the friction force  $F_D$ . Of particular interest to the theory of runaway electrons is the maximum in  $F_D$  at  $\sim 100$  eV and the corresponding electric field which is known as the thermal [Gurevich, 1961] runaway threshold ( $E_c$ ). Electrons with energies  $\sim 100$  eV moving through air will experience many collisions with neutral particles, which give rise to a high value of  $F_D$ . If an electric field  $E < E_c$  is applied to the electrons, the force  $F_E$  will be less than the force  $F_D$  the electrons will experience from collisions; therefore the electrons will be maintained at energies  $< 100$  eV. However, if an electric field  $E > E_c$  is applied to the electrons, it can be seen from Figure 2 that  $F_E > F_D$ . The electrons will gain more energy from the electric field than they will lose to collisions. It then becomes possible for some of the electrons to be energized to energies  $> 100$  eV. Owing to the reduced probability of collisions of electrons with energies  $> 100$  eV, the electrons will continue to accelerate to very high runaway energies as long as the electric field is present. Electric fields above  $E_c$  are difficult to produce and maintain since the electron runaway is also accompanied by an avalanche multiplication of electrons and strong increase in plasma conductivity, which tends to reduce the applied field. Electric fields  $\sim 10E_k$  around tips of propagating streamers (Figure 1) are one of the unique naturally occurring circumstances when such high fields can be dynamically produced and sustained for relatively extended periods of time.

[10] Also of interest is the minimum in  $F_D$  which occurs at  $\sim 1$  MeV. This is known as the relativistic [Gurevich et al., 1992; Roussel-Dupre et al., 1994] runaway threshold

( $E_t$ ) and is the basis of the Relativistic Runaway Electron Avalanche (RREA) model proposed by Gurevich et al. [1992]. At electron energies around 1 MeV the probability of collisions with neutrals is greatly decreased and any electron with an initial energy in this region (e.g., cosmic ray secondaries with energies 0.1–1 MeV [e.g., Roussel-Dupre et al., 1994; Gurevich and Zybin, 2005]) will run away when an electric field  $> E_t$  is applied. According to the RREA model, as few as one energetic electron ( $\sim 1$  MeV) can trigger an avalanche of runaway electrons, via ionization of air molecules and atoms, which will continue to grow as long as an electric field  $E > E_t$  is present.

[11] Additionally, at lower electric fields comparable to the conventional breakdown field  $E_k$ , electrons are expected to be held to energies  $< 20$  eV by collisional losses since  $F_D > F_E$  for energies  $> 20$  eV. At even lower field values (i.e., fractions of  $E_k$ ) electrons will be trapped by the local maximum in  $F_D$  around 1–2 eV resulting from strong energy losses due to excitation of vibrational degrees of freedom of nitrogen and oxygen molecules. The discrete structure observed at energies  $< 1$  eV also arises from the excitation of rotational degrees of freedom of nitrogen molecules and the excitation of rotational and vibrational degrees of freedom of oxygen molecules.

[12] The production of runaway electrons in the Earth's atmosphere has recently been linked to X-ray and gamma ray bursts observed during lightning discharges [Moore et al., 2001; Dwyer et al., 2003, 2004a, 2004b, 2005]. In addition to these ground-based measurements, intense gamma ray flashes originating from the Earth's atmosphere above thunderstorms have also been observed by the Compton Gamma Ray Observatory (CGRO) and the Reuven Ramaty High Energy Solar Spectroscopic Imager (RHessi) satellites [Fishman et al., 1994; Smith et al., 2005]. While these observations strongly support the existence of extremely high-energy electrons during thunderstorm activity, the exact mechanism producing them remains under debate [e.g., Dwyer, 2005a]. Gurevich [1961] showed that in the presence of extremely strong electric fields, a large number of low-energy electrons can be directly accelerated over the peak of the friction force  $F_D$  and become thermal runaway electrons. This is a relatively straightforward approach to runaway development and is readily accepted. However, since the electric field strengths necessary to achieve thermal runaway ( $E \sim 10E_k$ ) and even conventional ( $E \sim E_k$ ) breakdown are not commonly observed on large spatial scales in thunderclouds [Marshall et al., 1995, 2005], many scientists abandoned thermal runaway breakdown as a source of runaway electrons during thunderstorms and adopted the newer theory of RREA. One of the goals of the present paper is to demonstrate that streamers may represent a realistic source of thermal runaway electrons and discuss circumstances when these electrons can be accelerated to very high ( $> 1$  MeV) energies, thus providing an alternate source of seed electrons to the RREA model previously thought to require galactic cosmic rays.

### 1.3. Purpose of This Paper

[13] This paper presents the formulation of a Monte Carlo model, which is capable of describing electron dynamics in air including the electron thermal runaway phenomena

**Table 2.** Molecular Oxygen Collision Processes

Collision Process	Reaction	Threshold Energy, eV
O <sub>2</sub> elastic	$e + O_2 \rightarrow e + O_2$	-
O <sub>2</sub> rotational	$e + O_2 \rightarrow e + O_2(\text{rot})$	0.02
O <sub>2</sub> vibrational	$e + O_2 \rightarrow e + O_2(v=1, \epsilon < 4 \text{ eV})$	0.19
	$e + O_2 \rightarrow e + O_2(v=2, \epsilon < 4 \text{ eV})$	0.38
	$e + O_2 \rightarrow e + O_2(v=3)$	0.57
	$e + O_2 \rightarrow e + O_2(v=4)$	0.75
	$e + O_2 \rightarrow e + O_2(v=1, \epsilon > 4 \text{ eV})$	0.19
	$e + O_2 \rightarrow e + O_2(v=2, \epsilon > 4 \text{ eV})$	0.38
O <sub>2</sub> electronic	$e + O_2 \rightarrow e + O_2(a^1\Delta_g)$	0.977
	$e + O_2 \rightarrow e + O_2(b^1\Sigma_g^-)$	1.627
	$e + O_2 \rightarrow e + O_2(c^1\Sigma_u^-)$	4.50
	$e + O_2 \rightarrow e + O(^3P) + O(^3P)$	6.00
	$e + O_2 \rightarrow e + O(^3P) + O(^1D)$	8.40
	$e + O_2 \rightarrow e + O(^1D) + O(^1D)$	10.00
	$e + O_2 \rightarrow e + O(^3P) + O(^3S^0)$	14.70
O <sub>2</sub> ionization	$e + O_2 \rightarrow e + e + O_2^+(X^2\Pi_g)$	12.06
O <sub>2</sub> three-body attachment	$e + O_2 + A \rightarrow O_2^- + A$	-
O <sub>2</sub> two-body attachment	$e + O_2 \rightarrow O^- + O$	-

under influence of an external electric field of arbitrary strength. The model is similar in technical details to the model previously developed for  $N_2$  by *Tzeng and Kunhardt* [1986] and incorporates the following features: (1) the “null” collision method to determine time between collisions [*Lin and Bardsley*, 1977]; (2) the remapping of the electron assembly to improve statistics for the high-energy tail of the electron distribution [*Kunhardt and Tzeng*, 1986b]; (3) the differential ionization [*Opal et al.*, 1971] and scattering cross sections for realistic description of energy spectrum of secondary electrons and the forward scattering properties of electrons at high energies. Results for zero-dimensional modeling of the electron distribution under the influence of a uniform electric field are first presented and compared with existing data. At high electric fields the model is validated by comparisons with studies conducted for  $N_2$  by *Tzeng and Kunhardt* [1986] and more recently by *Bakhov et al.* [2000]. At low electric fields, model results are compared to available data from swarm experiments in air [*Davies*, 1983], numerical solutions of the Boltzmann equation based on the two-term spherical harmonic expansion of the electron distribution function [*Morgan and Penetrante*, 1990], and analytical models proposed by *Aleksandrov et al.* [1995] and *Morrow and Lowke* [1997]. The new Monte Carlo model is then applied to a one-dimensional case corresponding to a negative streamer tip immediately preceding branching. The model results demonstrate that the electric fields in streamer tips are strong enough to accelerate low-energy electrons to several keV, initiating thermal runaway in relatively low ambient fields. Streamers have been documented in transient luminous events above thunderclouds and in streamer zones of conventional lightning leaders and may provide a robust source of runaway electrons contributing to the production of recently observed X-ray and gamma ray bursts.

## 2. Model Formulation

### 2.1. Collision and Scattering Cross Sections

[14] Essential to both the numerical Boltzmann equation solution and the Monte Carlo method describing behavior

of electrons in weakly ionized air is the knowledge of electron-atom and electron-molecule collision cross sections for each gas species. Generally, atoms and molecules in a weakly ionized gas are assumed to be heavy and remain stationary; therefore the collision cross section becomes simply a function of the electron energy.

[15] For the Monte Carlo model presented in this paper several different cross section sets were used to determine an electron’s motion through air. A total of 46 collision processes were considered corresponding to the  $N_2$ ,  $O_2$ , and  $Ar$  gases included in the air mixture (see Tables 1, 2, and 3). Each gas has an associated elastic cross section accounting for elastic collisions and a set of inelastic cross sections (24 for  $N_2$ , 17 for  $O_2$  and 2 for  $Ar$ ) accounting for each inelastic collision process (i.e., rotational, vibrational, and electronic excitations, ionization, and attachment).

[16] The 43 inelastic cross sections  $\sigma_{\text{inel}}$  were obtained directly from the compilation of A.V. Phelps (<http://jilawww.colorado.edu/www/research/colldata.html>). The elastic collision cross section  $\sigma_{\text{el}}$  for each gas was then determined by subtracting the summation of inelastic cross sections from the total collision cross sections

$$\sigma_{\text{el},s} = \sigma_{t,s} - \sum_j \sigma_{\text{inel},j,s}, \quad (2)$$

where  $s$  represents a specific gas species and the summation is performed over all inelastic collision processes with  $j$  representing the  $j$ th process. The total collision cross sections were obtained from experimental data reported in literature as summarized in Table 4.

[17] The calculated elastic cross sections and the inelastic cross sections are the fundamental quantities used to determine an electron’s interaction with the gas medium. From these collision cross sections the mean free path, mean time between collisions, and collision frequency of an electron in the gas medium can be calculated as

$$\lambda = \frac{1}{N\sigma} \quad (3)$$

$$\tau = \frac{\lambda}{v} \quad (4)$$

$$\nu \equiv \tau^{-1} = N\sigma v, \quad (5)$$

respectively, where  $N$  is the gas density,  $\sigma$  is the collision cross section, and  $v$  is the electron’s velocity.

[18] In addition to the collision cross sections mentioned above, the differential scattering cross section  $\frac{d\sigma}{d\Omega}$  for each gas must be known to determine the angular scattering of electrons after a collision. Experimental values for the elastic differential scattering cross sections were obtained

**Table 3.** Argon Collision Processes

Collision Process	Reaction	Threshold Energy, eV
Ar elastic	$e + Ar \rightarrow e + Ar$	-
Ar electronic	$e + Ar \rightarrow e + Ar^*$	11.50
Ar ionization	$e + Ar \rightarrow e + e + Ar^+$	15.80

**Table 4.** Total Collision Cross Section Data Sources

Gas	Energy Range, eV	Literature Source
$N_2$	0–0.4	<i>Phelps and Pitchford</i> [1985]
	0.4–250	<i>Szmytkowski et al.</i> [1996]
	250–600	<i>Blaauw et al.</i> [1980]
	600–5000	<i>Garcia et al.</i> [1988]
	5000–10,000	<i>Phelps and Pitchford</i> [1985]
$O_2$	0–0.4	<i>Lawton and Phelps</i> [1978]
	0.4–250	<i>Szmytkowski et al.</i> [1996]
	250–500	<i>Dababneh et al.</i> [1988]
	500–5000	<i>Jain and Baluja</i> [1992]
	5000–10,000	extrapolated from <i>Jain and Baluja</i> [1992]
$Ar$	0–0.4	<i>Yamabe et al.</i> [1983]
	0.5–220	<i>Szmytkowski et al.</i> [1996]
	300–5000	<i>Karwasz et al.</i> [2002]
	5000–10,000	extrapolated from <i>Karwasz et al.</i> [2002]

from literature (see Table 5). The angular scattering of electrons in inelastic collisions was determined using the elastic differential cross sections listed in Table 5. This assumption is reasonable for scattering of electrons on the molecules with excitation of singlet states (predominantly forward) but may introduce error for the scattering involving excitation of the triplet states, which possess a stronger backscatter component [*Tzeng and Kunhardt*, 1986]. Figure 3 shows the elastic differential scattering cross section, for low-energy scattering obtained from sources listed in Table 5 for  $N_2$ ,  $O_2$ , and  $Ar$ . It can be seen from Figure 3 that at electron energies <20 eV the angular scattering of electrons is generally isotropic but quickly becomes forward for electron energies >20 eV. Electrons with energies  $\approx 0$  eV were assumed to demonstrate isotropic scattering and the differential cross section values from 0 to 5 eV for  $N_2$ , 0 to 2 eV for  $O_2$ , and 0 to 3 eV for  $Ar$  were determined using linear interpolation.

[19] For use in the Monte Carlo calculations, differential cross section tables for each gas were generated using linear interpolation of the data from sources listed in Table 5. The tables are then related to a uniform random number  $R_\chi$  from 0 and 1 as

$$R_\chi = \frac{\int_0^\chi 2\pi \frac{d\sigma}{d\Omega} \sin \chi d\chi}{\int_0^\pi 2\pi \frac{d\sigma}{d\Omega} \sin \chi d\chi}, \quad (6)$$

where  $\chi$  is the scattering angle of an electron. The scattering angle  $\chi$  can then easily be found by performing a table lookup using a random number  $R_\chi$  and the electron energy  $\epsilon$ . Angular scattering of electrons with energies in the range 0–500 eV experiencing collisions with  $N_2$ , and in the range of 0–1000 eV colliding with  $O_2$  and  $Ar$  is determined using lookup tables derived from published experimental data from sources given in Table 5.

## 2.2. High-Energy Electron Scattering

[20] For collisions involving electrons with energies greater than those tabulated from the experimental data (>500 eV for  $N_2$  collisions, >1000 eV for  $O_2$  and  $Ar$  collisions), differential scattering cross sections are calculated using several different approximations. It is the shortage of cross section data at high electron energies that remains the largest source of error in Monte Carlo

simulations and there is no commonly accepted approximation which is universally used.

[21] For low-energy electrons, the dominant process is relatively short-range polarization scattering [*Lieberman and Lichtenberg*, 1994, p. 60]. However, the mean collision time (equation (4)) of high-energy electrons is small, not allowing atoms and molecules adequate time to polarize. Therefore high-energy electron scattering from neutral particles (i.e., electron-atom and electron-molecule collisions) resembles Coulomb-like collisions between charged particles (i.e., electron-electron, electron-ion, and ion-ion collisions) [*Lieberman and Lichtenberg*, 1994, p. 60].

[22] The differential cross section for Coulomb-like collisions can be analytically derived as

$$\frac{d\sigma}{d\Omega} = \left[ \frac{b_0}{4 \sin^2(\chi/2)} \right]^2 \quad (7)$$

$$b_0 = \frac{q_1 q_2}{4\pi \epsilon_0 \epsilon}, \quad (8)$$

where  $q_1$  and  $q_2$  are charges of projectile and target particles,  $\epsilon_0$  is the permittivity of free space,  $\epsilon$  is the center-of-mass energy, and  $b_0$  is known as the classical distance of closest approach. Equation (7) is the well known Rutherford cross section for Coulomb scattering [*Lieberman and Lichtenberg*, 1994, p. 57]. In a general case, however, the Rutherford cross section cannot be directly used in Monte Carlo simulations because of the singularity as  $\chi \rightarrow 0$ . For this reason, a wide number of approximations based on screened Coulomb scattering have been implemented to determine the angular scattering of high-energy electrons in Monte Carlo and Boltzmann equation solutions.

[23] A. V. Phelps (<http://jilawww.colorado.edu/www/research/colldata.html>) presents an analytical differential scattering cross section approximation for elastic electron scattering from  $N_2$  based on a screened-Coulomb type scattering

$$\frac{d\sigma}{d\Omega} = \frac{1}{[1 - (1 - 2\beta(\epsilon)) \cos \chi]^2} \quad (9)$$

$$\beta(\epsilon) = \frac{.6}{[1 + \sqrt{\epsilon/50 + (\epsilon/20)^{1.01}}]^{0.99}}, \quad (10)$$

where here and in subsequent equations  $\epsilon$  is in units of eV and  $\beta(\epsilon)$  is an algebraic screening parameter derived to fit experimental angular distributions from *Phelps and*

**Table 5.** Differential Scattering Cross Section Data Sources

Gas	Energy Range, eV	Literature Source
$N_2$	5–90	<i>Shyn et al.</i> [1972]
	100–500	<i>Kambara and Kuchitsu</i> [1972]
$O_2$	2–200	<i>Shyn and Sharp</i> [1982]
	300–1000	<i>Iga et al.</i> [1987]
$Ar$	3–100	<i>Srivastava et al.</i> [1981]
	150–400	<i>Williams and Willis</i> [1975]
	200–500	<i>DuBois and Rudd</i> [1976]
	800–1000	<i>Iga et al.</i> [1987]

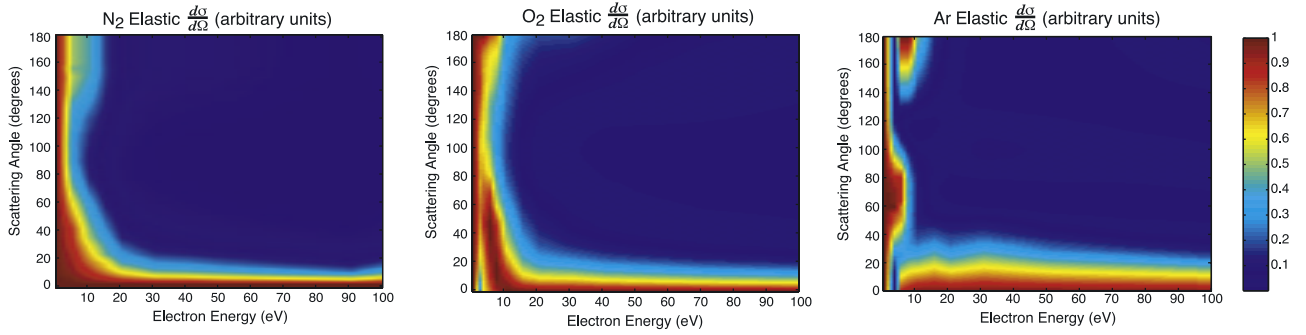


**Figure 3.** Elastic differential scattering cross section of  $N_2$ ,  $O_2$ , and  $Ar$  gases for electron energies ranging from 0 to 100 eV.

*Pitchford* [1985]. Substituting equation (9) into equation (6) and solving for the scattering angle  $\chi$  results in

$$\chi = \arccos \left[ \frac{1 - \beta(\varepsilon) - R_\chi}{1 - \beta(\varepsilon) - R_\chi + 2\beta(\varepsilon)R_\chi} \right], \quad (11)$$

where  $R_\chi$  is a uniform random number between 0 and 1.

[24] *Surendra et al.* [1990] proposed an analytical expression based on screened Coulomb scattering from  $Ar$

$$\frac{d\sigma}{d\Omega} = \frac{\varepsilon}{4\pi[1 + \varepsilon \sin^2(\chi/2)] \ln(1 + \varepsilon)} \quad (12)$$

such that the electron-neutral scattering at low energies is mainly isotropic and becomes increasingly anisotropic as the electron energy increases. Substituting equation (12) into equation (6) and solving for the scattering angle  $\chi$  results in

$$\chi = \arccos \left[ \frac{2 + \varepsilon - 2(1 + \varepsilon)^{R_\chi}}{\varepsilon} \right]. \quad (13)$$

[25] In his study of an electron avalanche development in neon, *Shveigert* [1990] used the differential scattering cross section for the scattering of fast electrons by shielded Coulomb potential of a nucleus as published by *Kol'chuzhkin and Uchaikin* [1978]:

$$\frac{d\sigma}{d\Omega} = \frac{1}{4} \frac{Z(Z+1)}{\varepsilon^2} q_e^4 \frac{1}{(1 - \cos \chi + 2\eta)^2} \quad (14)$$

$$\eta = \frac{20(\varepsilon + 96)}{\varepsilon^2}, \quad (15)$$

where  $Z$  is the number of protons in the atom's nucleus and  $\eta$  is the shielding parameter formulated to fit the calculations of *Thomas* [1969] at  $\varepsilon = 100$  eV. Scattering angles from this approximation are tabulated numerically using equation (6).

[26] A modified Rutherford cross section was also introduced for use in this paper of the form

$$\frac{d\sigma}{d\Omega} = \frac{\varepsilon/\varepsilon_1}{4\pi \arctan(\varepsilon/\varepsilon_1)} \frac{1}{1 + (\varepsilon^2/\varepsilon_1^2) \sin^4(\chi/2)}, \quad (16)$$

where  $\varepsilon_1$  is a shape parameter which is set to  $\varepsilon_1 = 4$  eV to match experimental data of *Kambara and Kuchitsu* [1972] for electron scattering from  $N_2$  at 500 eV. Substituting equation (16) into equation (6) and solving for the scattering angle  $\chi$  results in

$$\chi = 2 \arcsin \left[ \sqrt{(\varepsilon_1/\varepsilon) \tan(R_\chi \arctan(\varepsilon/\varepsilon_1))} \right]. \quad (17)$$

[27] The differential cross section used to approximate high-energy electron scattering can greatly impact the generation of runaway electrons and will be discussed further in sections 3.3, 4.1, and 4.2. Figure 4 shows the differential cross sections described by equations (9), (12), (14), and (16).

[28] It should be noted that while Figures 4a through 4d are plotted for the energy range 0–1000 eV, the cross sections are only used in the model for collisions with  $N_2$  where  $\varepsilon > 500$  eV and collisions with  $O_2$  and  $Ar$  where  $\varepsilon > 1000$  eV. Figure 5a shows a comparison of equations (9), (12), (14), and (16) with experimental data of *Kambara and Kuchitsu* [1972] for electron collisions with  $N_2$  at  $\varepsilon = 500$  eV and Figure 5b shows a similar comparison with experimental data of *Iga et al.* [1987] for electron collisions with  $O_2$  at  $\varepsilon = 1000$  eV. Upon first examination of Figures 4 and 5, the differences between the differential cross sections may appear to be small. However, the forward scattering properties of high-energy electrons are vital in the development of electron runaway and these small variations can drastically hinder or facilitate the runaway process (sections 3.3, 4.1, and 4.2).

### 2.3. Differential Ionization Cross Section

[29] The behavior of the phase-space distribution of electrons is strongly influenced by ionization and the angle and energy of each of the two electrons emerging from the collision [*Tzeng and Kunhardt*, 1986]. *Tzeng and Kunhardt* [1986] placed special emphasis on the energy partitioning used in ionizing collisions and presented results for four separate cases:

[30] In case 1 the secondary electron is assigned zero energy, leaving the primary electron with the difference between initial energy and the ionization energy. In case 2 the energy of the secondary is determined from the differential cross section for ionization determined from experiments by *Opal et al.* [1971]. In case 3 the fraction of half the available energy given to the secondary is a random variable

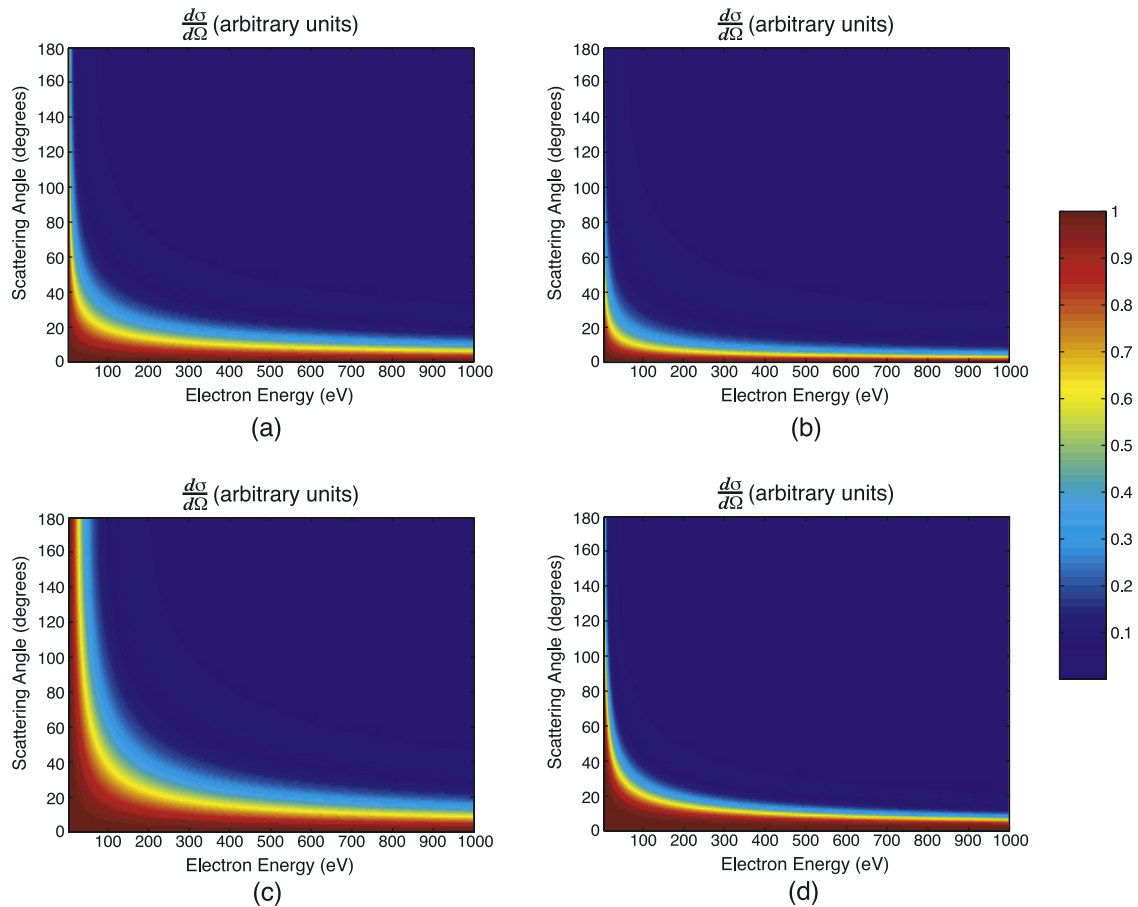


**Figure 4.** Differential scattering cross section of Phelps (a) (<http://jilawww.colorado.edu/www/research/colddata.html>) calculated using equation (9) of *Surendra et al.* [1990] (b) based on equation (12) of *Kolchuzhkin and Uchaikin* [1978] (c) described by equation (14), and (d) as calculated using equation (16).

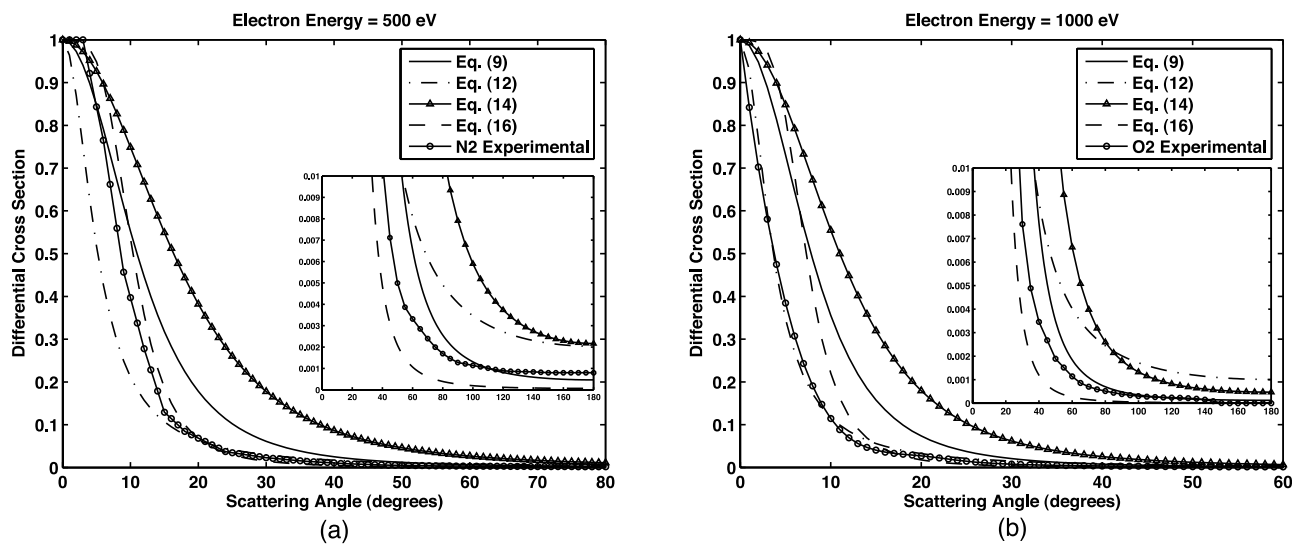


**Figure 5.** The differential scattering cross section for (a) 500 eV and (b) 1000 eV electrons calculated from equations (9), (12), (14), and (16) compared with experimental data of *Kambara and Kuchitsu* [1972] and *Iga et al.* [1987], respectively.

**Table 6.** Ionization Energies  $\varepsilon_{iz}$  and Ejected Electron Spectrum Shape Parameter  $\bar{\varepsilon}$  in eV [*Opal et al.*, 1971]

Gas	$\varepsilon_{iz}$	$\bar{\varepsilon}$
N <sub>2</sub>	15.6	13.0
O <sub>2</sub>	12.2	17.4
Ar	15.7	10.0

uniformly distributed in the interval [0,1]. In case 4 the primary and secondary electrons equally share the available energy.

[31] The differences in the energy distribution functions for each of these cases are significant, especially at high electron energies. The variations can best be explained by considering the energy of the incident electron after an ionizing collision

$$\varepsilon'_p = \varepsilon_p - \varepsilon_{iz} - \varepsilon_s, \quad (18)$$

where  $\varepsilon_p$  is the energy of the incident electron before the collision,  $\varepsilon_s$  is the energy of the secondary electron generated by the collision, and  $\varepsilon_{iz}$  is the ionization potential. For cases 3 and 4 the high-energy incident electrons participating in the ionizing collisions lose a large fraction of their energy to the secondary electron ( $\varepsilon_s$  is large), thus severely reducing the number of electrons which can accelerate to runaway energies. In contrast, incident electrons in case 1 lose only energy equal to the ionization potential,  $\varepsilon_{iz}$ , ( $\varepsilon_s = 0$ ), thus contributing to an overpopulation of electrons existing at very low energies due to the low-energy secondaries as well as an overpopulation of runaway energy electrons due to high-energy incident electrons losing only a small fraction of their energy to ionizing collisions. Among the cases presented, case 2, which makes use of the secondary energy distribution suggested by *Opal et al.* [1971], is the most realistic [Tzeng and Kunhardt, 1986] and is used for all simulations presented in this paper.

[32] *Opal et al.* [1971] measured a quantity proportional to the doubly differential cross section  $\sigma(\varepsilon_p, \varepsilon_s, \chi)$ . Integrating this cross section over the angle  $\chi$ , results in

$$\sigma(\varepsilon_p, \varepsilon_s) = \int_0^\pi \sigma(\varepsilon_p, \varepsilon_s, \chi) 2\pi \sin \chi d\chi. \quad (19)$$

Assuming the ion to be massive and at rest, the kinetic energy imparted to the ion in the collision is negligible and the energies of the two departing electrons must sum to  $\varepsilon_p - \varepsilon_{iz}$  and be symmetrical about  $(\varepsilon_p - \varepsilon_{iz})/2$  [*Opal et al.*, 1971]. The total ionization cross section can then be given by

$$\sigma_i(\varepsilon_p) = \int_0^{(\varepsilon_p - \varepsilon_{iz})/2} \sigma(\varepsilon_p, \varepsilon_s) d\varepsilon_s. \quad (20)$$

From results of their experiments, *Opal et al.* [1971] determined the differential ionization cross section to be

$$\sigma(\varepsilon_p, \varepsilon_s) = \frac{\sigma_i(\varepsilon_p)}{\bar{\varepsilon} \cdot \arctan[(\varepsilon_p - \varepsilon_{iz})/2\bar{\varepsilon}]} \cdot \frac{1}{1 + (\varepsilon_s/\bar{\varepsilon})^2}, \quad (21)$$

where  $\bar{\varepsilon}$  is a shape parameter adjusted to fit the ejected electron spectrum. Values of  $\bar{\varepsilon}$  determined by *Opal et al.* [1971] are listed in Table 6 for N<sub>2</sub>, O<sub>2</sub>, and Ar gases.

[33] The differential ionization cross section of *Opal et al.* [1971] can be used to determine the energy  $\varepsilon_s$  of the secondary electron. Similarly to the determination of the scattering angle from the differential scattering cross section from equation (6),  $\varepsilon_s$  can be related to a uniform random number  $R_{\varepsilon_s}$  by performing the integration

$$R_{\varepsilon_s} = \frac{\int_0^{\varepsilon_s} \sigma(\varepsilon_p, \varepsilon_s) d\varepsilon_s}{\int_0^{(\varepsilon_p - \varepsilon_{iz})/2} \sigma(\varepsilon_p, \varepsilon_s) d\varepsilon_s}. \quad (22)$$

Observing that the denominator of equation (22) is the total ionization cross section  $\sigma_i(\varepsilon_p)$  and substituting the differential ionization cross section of *Opal et al.* [1971] (21), equation (22) can be rewritten as

$$\begin{aligned} R_{\varepsilon_s} &= \frac{1}{\bar{\varepsilon} \arctan[(\varepsilon_p - \varepsilon_{iz})/2\bar{\varepsilon}]} \int_0^{\varepsilon_s} \frac{1}{1 + (\varepsilon_s/\bar{\varepsilon})^2} d\varepsilon_s \\ &= \frac{\arctan(\varepsilon_s/\bar{\varepsilon})}{\arctan[(\varepsilon_p - \varepsilon_{iz})/2\bar{\varepsilon}]}. \end{aligned} \quad (23)$$

Solving equation (23) for the secondary electron energy  $\varepsilon_s$  results in

$$\varepsilon_s = \bar{\varepsilon} \tan \left[ R_{\varepsilon_s} \arctan \left( \frac{\varepsilon_p - \varepsilon_{iz}}{2\bar{\varepsilon}} \right) \right]. \quad (24)$$

[34] Also, as mentioned in section 1.2, the differential ionization cross section of *Opal et al.* [1971] was used in the determination of the dynamic friction force in air (see Figure 2). Using the differential cross section defined by equation (21), the average energy of a secondary electron emerging from an ionizing collision can be found as

$$\begin{aligned} \langle \varepsilon_s(\varepsilon_p) \rangle &= \frac{1}{\sigma_i(\varepsilon_p)} \int_0^{(\varepsilon_p - \varepsilon_{iz})/2} \varepsilon_s \sigma(\varepsilon_p, \varepsilon_s) d\varepsilon_s \\ &= \frac{\bar{\varepsilon}}{2 \arctan \left( \frac{\varepsilon_p - \varepsilon_{iz}}{2\bar{\varepsilon}} \right)} \ln \left[ 1 + \frac{(\varepsilon_p - \varepsilon_{iz})^2}{4\bar{\varepsilon}^2} \right]. \end{aligned} \quad (25)$$

After obtaining the average secondary energy  $\langle \varepsilon_s(\varepsilon_p) \rangle$ , the friction force of ionizing collisions can be calculated as

$$F_I(\varepsilon) = N_j \sigma_j(\varepsilon) [\varepsilon_{izj} + \langle \varepsilon_{s,j}(\varepsilon) \rangle], \quad (26)$$

where the index  $j$  accounts for differences in the ionization potential and the average secondary energy corresponding to different target species with density  $N_j$ .

#### 2.4. Null Collision Method

[35] The Monte Carlo method works by individually tracking each electron in an assembly through a series of time steps until an equilibrium state is attained (e.g., electron mean energy remains constant). In a given time step,  $\Delta t$ , the electron may or may not experience a collision with the probability of a collision being [*Dincer and Govinda Raju*, 1983]

$$P = 1 - e^{-\frac{\Delta t}{\tau}}, \quad (27)$$

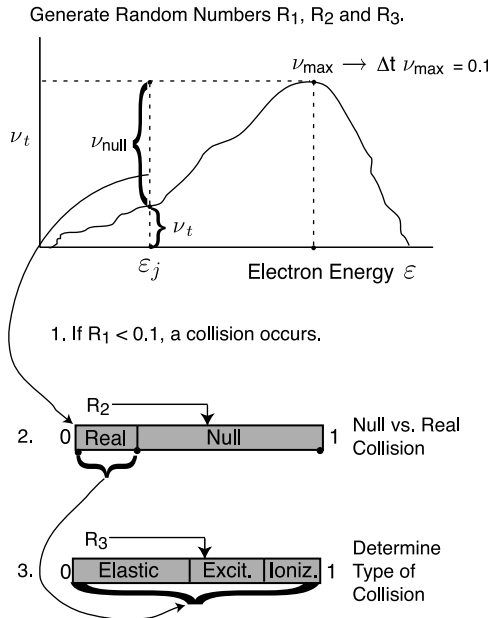


**Figure 6.** Schematic summary of the null collision method used in the Monte Carlo simulation.

where  $\tau$  is the mean time between collisions of an electron defined by equation (4). We note that the mean collision time in equation (4) depends on the electron's velocity. Therefore for a large number of electrons included in a simulation, there will be an equally large number of distinct time steps between collisions. The computation required to support each electron possessing its own mean collision time is a daunting task and can be overcome by adopting a null collision technique [Lin and Bardsley, 1977], which allows a constant mean collision time to be defined for all electrons in the system. The null collision approach first defines the total collision frequency as the sum of all elastic and inelastic collision frequencies

$$\nu_t(\epsilon) = \sum_{j=1}^n \nu_j(\epsilon) = \sum_{j=1}^n N_j \sigma_j(\epsilon) v(\epsilon), \quad (28)$$

where

$$v(\epsilon) = \sqrt{\frac{2q_e \epsilon}{m}}, \quad (29)$$

$m$  is the mass of an electron, and  $N_j$  represents a partial density of target molecules or atoms corresponding to a particular collision process defined by the cross section  $\sigma_j$ . Having plotted  $\nu_j(\epsilon)$  versus electron energy (as schematically shown at the top of Figure 6), the maximum collision frequency  $\nu_{\max}$  can be found

$$\nu_{\max} = \max[\nu_t(\epsilon)]. \quad (30)$$

The constant mean collision time  $\tau_c$  can then be calculated by substituting  $\nu_{\max}$  into equation (5)

$$\tau_c = \frac{1}{\nu_{\max}}. \quad (31)$$

A constant time step  $\Delta t$  can then be defined as

$$\Delta t = \frac{\delta}{\nu_{\max}} = \delta \tau_c, \quad (32)$$

where  $\delta$  is an arbitrary number much less than 1. In all calculations presented in this paper,  $\delta$  is assumed to be equal to 0.1 (see Figure 6).

[36] Now, having obtained a constant time step to be used throughout the simulation, the null collision technique can be viewed as a three step procedure using three uniform random numbers between 0 and 1 to determine if an electron experiences a collision in a time step, and if so, what type of collision it was. An outline of the null collision method is provided in Figure 6.

[37] 1. Substituting  $\tau_c$  and  $\Delta t$  into equation (27) results in a constant probability of a collision in a time step

$$P_{\text{coll}} = 1 - e^{-\frac{\delta \tau_c}{\tau_c}} = 1 - e^{-\delta} \simeq \delta = 0.1. \quad (33)$$

Therefore if a uniform random number  $R_1$  from 0 to 1 is less than 0.1 for a given electron, the electron is said to have experienced a collision in the time step.

[38] 2. Having determined that an electron experienced a collision in step 1, we must now determine whether the collision is a null or real collision. The energy independent maximum collision frequency  $\nu_{\max}$  defined by equation (30) can be represented as the sum of the energy dependent null  $\nu_{\text{null}}(\epsilon)$  and real  $\nu_r(\epsilon)$  collision frequencies (see top of Figure 6)

$$\nu_{\max} = \nu_r(\epsilon) + \nu_{\text{null}}(\epsilon). \quad (34)$$

The probability of a real collision,  $P_{\text{real}}$ , can then be defined as

$$P_{\text{real}}(\epsilon) = \frac{\nu_r(\epsilon)}{\nu_{\max}} \quad (35)$$

and is a function of the electron energy  $\epsilon$ . For each electron which was determined to have experienced a collision in step 1, a second random number  $R_2$  with a uniform distribution between 0 and 1 is generated and compared with the probability  $P_{\text{real}}$  corresponding to the electron's energy. If  $R_2 \leq P_{\text{real}}$  the collision is considered to be real, otherwise ( $R_2 > P_{\text{real}}$ ) the collision is considered to be null and has no effect on the electron's properties (see Figure 6).

[39] 3. If the collision was determined to be real in step 2, then the next step is to determine what type of collision (i.e., momentum transfer, excitation, ionization) occurred. At a given electron energy  $\epsilon_j$ , there is a collection of individual collision frequencies  $\nu_j(\epsilon)$ , which sum to equal the total collision frequency  $\nu_t(\epsilon)$  as shown by equation (28). The probability of each collision process can then be calculated as

$$P_j = \frac{\nu_j(\epsilon)}{\nu_t(\epsilon)} \quad (36)$$

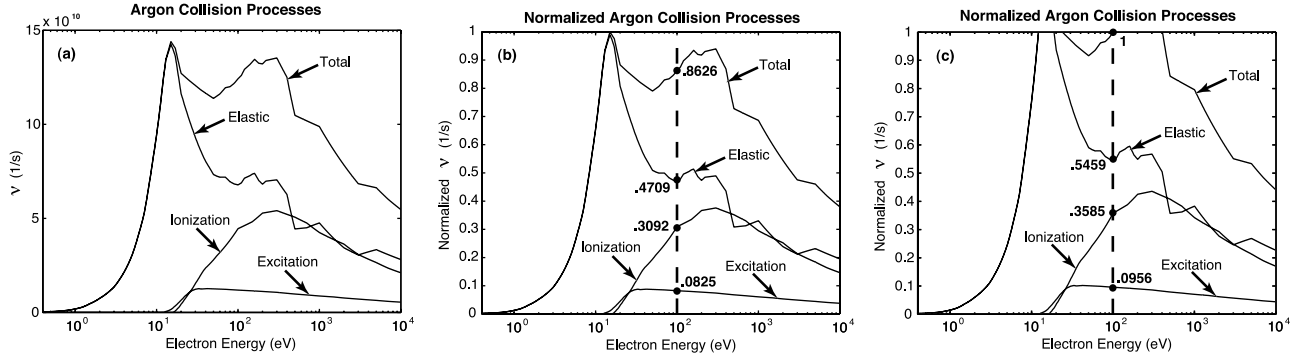


**Figure 7.** (a) *Ar* total, elastic, ionization, and excitation collision frequencies as a function of electron energy, (b) the normalized collision frequencies to determine the occurrence of a null or real collision, (c) and normalized frequencies by the total collision frequency at 100 eV to determine the type of collision (see text for details).

at a given electron energy  $\varepsilon$  such that

$$\sum_{j=1}^n P_j = 1. \quad (37)$$

Each collision process can then be assigned a range of numbers existing between 0 and 1 by performing a cumulative summation of the individual probabilities  $P_j$  such that *Range 1* = 0 to  $P_1$ , *Range 2* =  $P_1$  to  $P_1 + P_2$ , *Range 3* =  $P_1 + P_2$  to  $P_1 + P_2 + P_3$ , etc. A third uniform random number  $R_3$  between 0 and 1 can then be generated and whichever process's range it falls within is determined to be the collision process which occurred (see Figure 6).

[40] To better illustrate the procedures of step 2 and step 3, consider a simple case of only argon gas. The collision frequencies of argon are shown in Figure 7a. Normalizing the collision frequencies according to equation (35) results in values between 0 and 1 as shown in Figure 7b. From Figure 7b it can be seen that for a 100 eV electron, the total normalized collision frequency is  $0.0825 + 0.3092 + 0.4709 = 0.8626$ . A real collision is said to occur if random number  $R_2$  is such that  $0 < R_2 < 0.8626$  and a null collision occurs if  $R_2 > 0.8626$ . If it is determined that a real collision has occurred, then the collision processes must be normalized by the value of the total collision frequency at 100 eV of 0.8626 as shown in Figure 7c. Now random number  $R_3$  will be generated to determine which type of collision occurred. If  $0 < R_3 < 0.5459$ , the collision is said to be elastic. If  $0.5459 < R_3 < 0.6415$  (where  $0.5459 + 0.0956 = 0.6415$ ), the collision is said to be excitation. Finally, if  $0.6415 < R_3 < 1$  (where  $0.6415 + 0.3585 = 1$ ), the collision is said to be ionization. After the type of collision is determined, the electron's properties (i.e., energy, velocity, direction) are modified accordingly as described in section 2.5 below.

[41] After simulating each electron's interactions through a time step as described in steps 1, 2, and 3, the electron velocities are updated to reflect acceleration due to the applied electric field and diagnostic data is saved. If a specified number of electrons has been reached due to ionization processes, a particle remapping scheme (section 2.6) is applied to avoid undesirably long computation times. The procedure above is then repeated until an equilibrium state is reached or until a point in time, which is defined by an investigator.

## 2.5. Energy Loss and Scattering of Electrons

[42] There are four types of collision processes considered in this paper: elastic, excitation, ionization, and attachment. When one of these collision processes occur in a Monte Carlo simulation (see section 2.4), the colliding

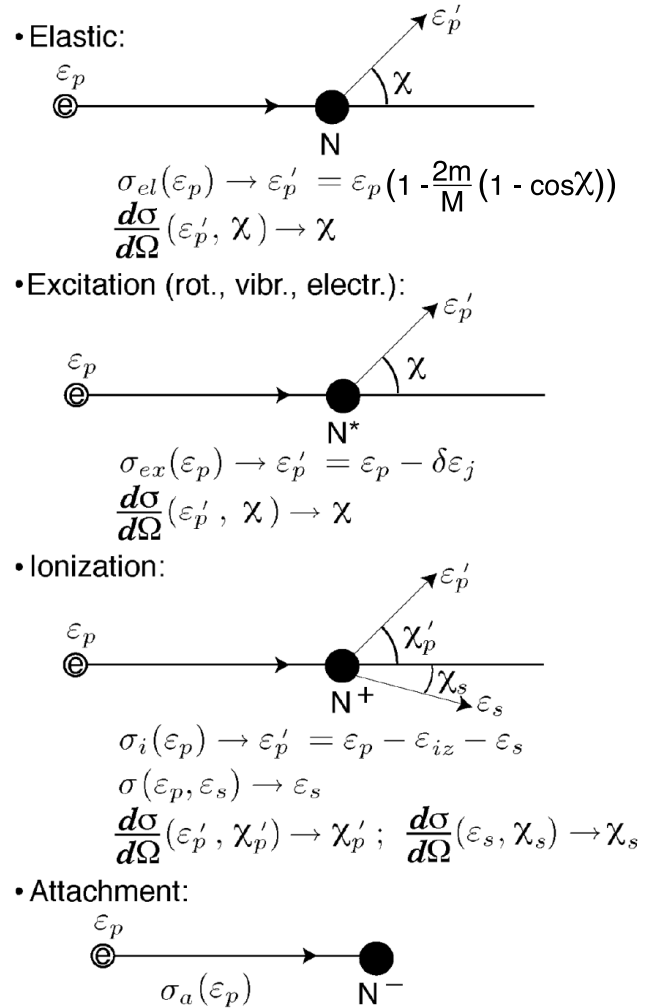


**Figure 8.** Summary of electron-atom/molecule collisions in air.

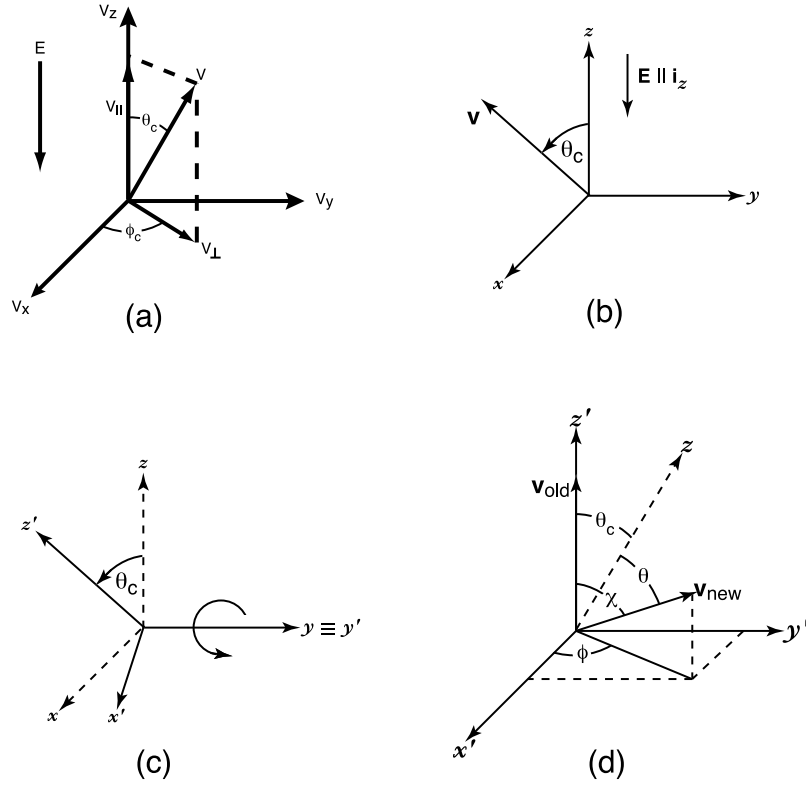


**Figure 9.** (a) Representation of electron velocity  $v$  by components parallel  $v_{||}$  and perpendicular  $v_{\perp}$  to the applied electric field  $E$ ; (b) electron trajectory in  $(x, y, z)$  coordinates; (c)  $(x', y', z')$  coordinates; and (d) the treatment of electron scattering.

electron's energy and trajectory following the collision must be determined. A summary of these collisions is shown in Figure 8.

[43] First, consider an electron characterized by its perpendicular  $v_{\perp}$  and parallel  $v_{||}$  velocity components with respect to the applied electric field and angles  $\theta_c$  and  $\phi_c$  as shown in Figure 9a, where

$$|\mathbf{v}| = \sqrt{v_{||}^2 + v_{\perp}^2} \quad (38)$$

$$v_{\perp} = |\mathbf{v}| \sin \theta_c \quad (39)$$

$$v_{||} = |\mathbf{v}| \cos \theta_c. \quad (40)$$

Since only electron collisions with massive, stationary neutral atoms and molecules are considered, scattering events can be treated in center-of-mass coordinates [Lieberman and Lichtenberg, 1994, p. 51]. For simplicity, the initial angle  $\phi_c$  is assumed to be zero and the electron velocity  $\mathbf{v}$  is always in the  $(x, z)$  plane as shown in Figure 9b. Now envision the electron colliding with neutral particle resting in the line of  $\mathbf{v}$  and scattering at an angle  $\chi$  through a differential solid angle  $d\Omega = \sin \chi d\chi d\phi$ . To find the new trajectory of the electron after the collision, it is useful to define a new coordinate system  $(x', y', z')$  by rotating the initial coordinate system  $(x, y, z)$  about the  $y$ -axis by  $\theta_c$  as shown in Figure 9c. The electron scattering can now easily be treated in the new  $(x', y', z')$  coordinates as shown in Figure 9d where  $\mathbf{v}_{old}$  is the

particle velocity before scattering,  $\theta_c$  is the angle of the particle before scattering in  $(x, y, z)$  coordinates,  $\mathbf{v}_{new}$  is the velocity after scattering,  $\chi$  is the angle after scattering in  $(x', y', z')$  coordinates,  $\theta$  is the angle after scattering in  $(x, y, z)$  coordinates, and  $\phi$  is considered to be random. The new trajectory of the electron in  $(x, y, z)$  coordinates can then be calculated as follows:

$$\cos \theta = \cos \theta_c \cos \chi + \sin \theta_c \sin \chi \cos(2\pi R_{\phi}) \quad (41)$$

$$\sin \theta = \sqrt{1 - \cos^2 \theta}, \quad (42)$$

where  $\cos \theta_c$  and  $\sin \theta_c$  describe the electron's trajectory before the collision,  $\cos \theta$  and  $\sin \theta$  describe the trajectory after the collision, and  $R_{\phi}$  is a uniform random number between 0 and 1.

### 2.5.1. Elastic Collisions

[44] In the case of an elastic collision, the only energy loss mechanism is the momentum transfer between the electron and the neutral particle. This energy loss is a function of the scattering angle of the electron following the collision, therefore the first step when an elastic collision occurs is to determine the scattering angle  $\chi$  from equation (6). After obtaining  $\chi$ , the new trajectory of the electron can be calculated using equations (41) and (42) and the energy loss due to momentum transfer can be determined as [e.g., Liu and Govinda Raju, 1992; Lieberman and Lichtenberg, 1994, p. 54]:

$$\epsilon'_p = \epsilon_p \cdot \left[ 1 - \frac{2m}{M} \cdot (1 - \cos \chi) \right], \quad (43)$$

where  $M$  is the mass of the neutral particle.

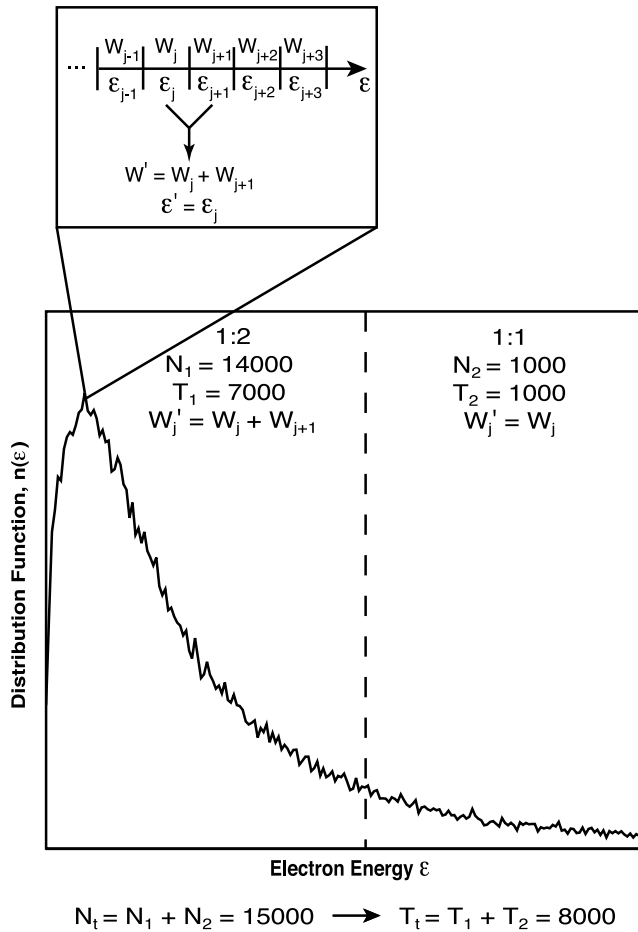


**Figure 10.** Schematic example of a particle remapping calculation reducing the total number of particles from  $N_i = 15,000$  to  $T_i = 8000$ .

### 2.5.2. Excitation Collisions

[45] Although the physics behind excitation collisions is complex, calculating the incident electron's properties after an excitation collision is trivial. The excitation energies and collision cross sections corresponding to many electron-neutral collisions have been well studied and experimental data is readily available in literature. Therefore the new energy of an incident electron after an excitation collision can be simply calculated as

$$\epsilon'_p = \epsilon_p - \delta\epsilon_j, \quad (44)$$

where  $\delta\epsilon_j$  is the energy lost by the electron for the excitation process  $j$ , as schematically illustrated in Figure 8 for a case of excitation collisions. After obtaining the electron's new energy  $\epsilon'_p$ , the scattering angle of the electron can be determined from equation (6) noting that  $\epsilon$  is replaced by  $\epsilon'_p$ . This approach is consistent with that used by *Kunhardt and Tzeng* [1986b]. The electron's new trajectory can then be calculated using equations (41) and (42).

### 2.5.3. Ionization Collisions

[46] When an ionization collision occurs, the first step is to determine the energy of the secondary electron  $\epsilon_s$ , this can be done using the differential ionization cross section of *Opal et al.* [1971] and equation (24). After

finding the energy of the secondary electron  $\epsilon_s$  emerging from the ionizing collision, the new energy of the incident electron  $\epsilon'_p$  can be calculated using equation (18) as also schematically shown in Figure 8 for a case of ionization collisions. The scattering angle of the primary and secondary electrons can then be found using equation (6) substituting  $\epsilon \rightarrow \epsilon'_p$  and  $\epsilon \rightarrow \epsilon_s$ , respectively. This approach is consistent with that used by *Kunhardt and Tzeng* [1986b]. The trajectory of both electrons can then be calculated using equations (41) and (42).

### 2.5.4. Attachment Collisions

[47] Attachment is a process in which an electron collision with an atom, molecule or molecules results in the formation of a negative ion. For the model presented in this paper, two types of electron attachment to  $O_2$  are considered, two-body dissociative attachment and three-body attachment (see Table 2). When electron attachment occurs, the electron is simply removed from the simulation and further effects of negative ions on the electron population (i.e., owing to detachment or scattering) are not considered.

### 2.6. Particle Remapping

[48] A limiting factor associated with Monte Carlo simulation is the long computation times and computer memory required to fully describe a physical system with millions of individual elements and a large number of time steps required to reach a converging solution. In the case of using the Monte Carlo technique to calculate the electron energy distribution in air, this problem arises due to increasing ionization rates at high electric fields leading to an enormous multiplication of particles to be tracked in the simulation. To resolve this issue, a so-called nonanalog Monte Carlo technique of statistical weighting similar to that of *Kunhardt and Tzeng* [1986b] is introduced.

[49] After a predetermined number of particles,  $N_i$  (usually 15,000), is reached in a simulation, a remapping of the electron assembly is performed to reduce the total number of particles to another predetermined number,  $T_i$  (usually 8000), with each new particle being assigned a new particle weight to reflect how many electrons the particle represents. Given the nature of the electron energy distribution function in air (i.e., the bulk of the electron distribution is maintained at lower energies with a small number of electrons constituting a high-energy tail), measures must be taken to maintain appropriate resolution in the high-energy tail of the distribution especially in the study of runaway phenomena. To do this, the initial particles  $N_i$  are first sorted in order of increasing energy. After sorting the particles, they are then partitioned into two groups, one group representing the low-energy body  $N_1$  of the distribution and another representing the high-energy tail  $N_2$  (see Figure 10). The first low-energy group of particles is remapped such that the weights of adjacent particles in energy space ( $W_j$  and  $W_{j+1}$ ) are combined into one particle with a new particle weight  $W'_j$  such that

$$W'_j = W_j + W_{j+1}. \quad (45)$$

The new particle assumes the properties of the  $j$ th particle such that  $\epsilon_{\text{new}} = \epsilon_j$ ,  $v_{\parallel, \text{new}} = v_{\parallel, j}$ , and  $v_{\perp, \text{new}} = v_{\perp, j}$ , which is an adequate assumption since the energy difference between two adjacent particles in energy space after the sorting will be small in the low-energy body of the electron energy

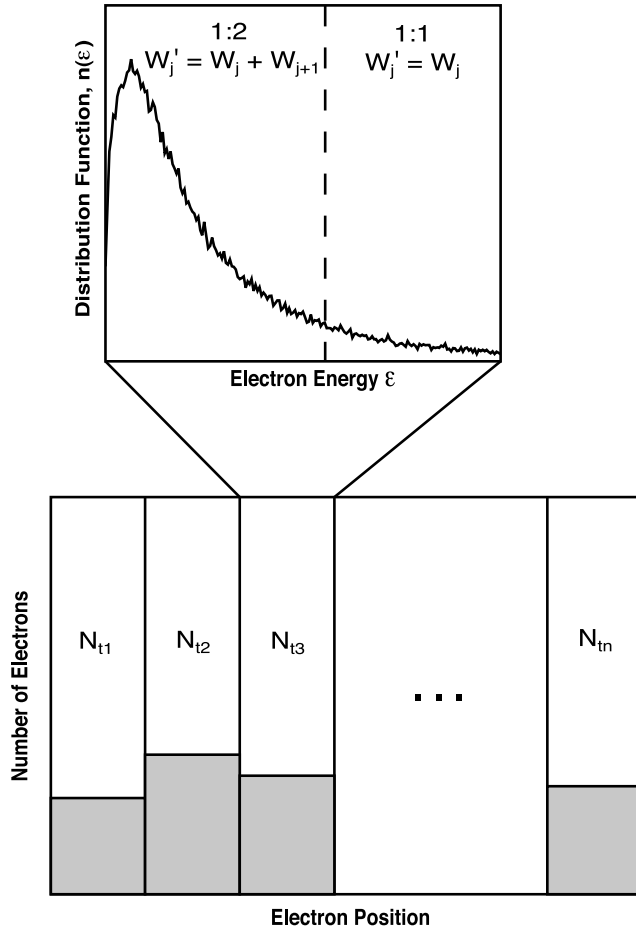


**Figure 11.** Schematic example of a particle remapping calculation when the spatial position of particles is considered.

distribution. This results in the total number of particles in the low-energy region being reduced from  $N_1$  to  $T_1$  (usually 7000) particles. The high-energy tail group is then remapped 1:1 to ensure enhanced resolution at high electron energies such that

$$W'_j = W_j \quad (46)$$

for all particles in the tail and  $N_2 = T_2$  (usually 1000). The procedure is repeated each time the particle count in a simulation exceeds  $N_l$  and is validated by comparing the electron energy distribution function from before and after the remapping events.

[50] For simulations when the spatial distribution of electrons must also be considered, as with the one-dimensional treatment of runaway electrons in a streamer tip (section 4), remapping the particle assembly becomes slightly more complicated. When remapping occurs, the particles are first sorted according to increasing position along the z-axis. The particles are then divided into equally spaced spatial bins (usually 10) and then sorted in order of increasing energy within each bin. The remapping of particles is then performed within each bin according to the same 1:2 for low-energy and 1:1 for high-energy particles as discussed in the previous paragraph (see Figure 11). The remapping

scheme is validated by comparing the electron energy distribution function before and after a remapping event.

## 2.7. Model Initialization and Execution

[51] Figure 12 shows a flow chart representing the execution of the Monte Carlo model. First, the user must input basic simulation parameters such as the initial number of particles to be used (usually 8000), the applied electric field strength, the length of the simulation, the fractional composition of the gas mixture (i.e., 78.11%  $N_2$ , 20.91%  $O_2$ , and 0.98% Ar), and the number of particles at which the particle assembly will be remapped (usually 15,000, see section 2.6).

[52] After the input parameters are entered, the model can then calculate the initial electron distribution and define necessary quantities to be used throughout the simulation such as the collision frequency and the size of the time step. The initial electron set is normally assigned a Maxwellian velocity distribution [Chen, 1984, p. 226; Birdsall and Langdon, 1991, p. 390] corresponding to an initial electron temperature of  $T_e = 5800$  K (i.e., 0.5 eV). To achieve a Maxwellian velocity distribution, each electron is assigned a  $v_x$ ,  $v_y$ , and  $v_z$  velocity component. Using the error function, defined by

$$erf(v) = \frac{2}{\sqrt{\pi}} \int_0^v e^{-t^2} dt, \quad (47)$$

where in the context of the present problem  $0 \leq v \leq 5$  is a generic range normalized by thermal velocity  $v_{th} = \sqrt{\frac{2kT_e}{m}}$ , the normalized  $v_x$  component of an electron's velocity can be related to a uniform random number  $R_j$  between 0 and 1 from the relationship [e.g., Birdsall and Langdon, 1991, p. 390]

$$R_j = \frac{2}{\sqrt{\pi}} \int_0^{v_x} e^{-t^2} dt = erf(v_x). \quad (48)$$

Similarly, the normalized  $v_y$  and  $v_z$  velocity components can also be found for each electron using equation (48). After assigning velocity components to half of the electron population, the remaining electron velocities may be found by mirroring the positive velocity components found from equation (48) to the corresponding negative values. A true three-dimensional (3-D) Maxwellian distribution is then arrived at by multiplying the normalized  $v_x$ ,  $v_y$ ,  $v_z$  components of each electron by the thermal velocity  $v_{th}$ . The 3-D distribution is then transformed to parallel and perpendicular velocity components for use in the Monte Carlo simulation as

$$v_{\parallel} = v_z \quad (49)$$

$$v_{\perp} = \sqrt{v_x^2 + v_y^2}, \quad (50)$$

assuming an electric field in the z-direction (see Figure 9).

[53] The total collision frequency  $\nu_t(\epsilon)$ , the collision frequency for each process  $\nu_j(\epsilon)$ , and the maximum collision frequency  $\nu_{max}$  are calculated from the cross section data

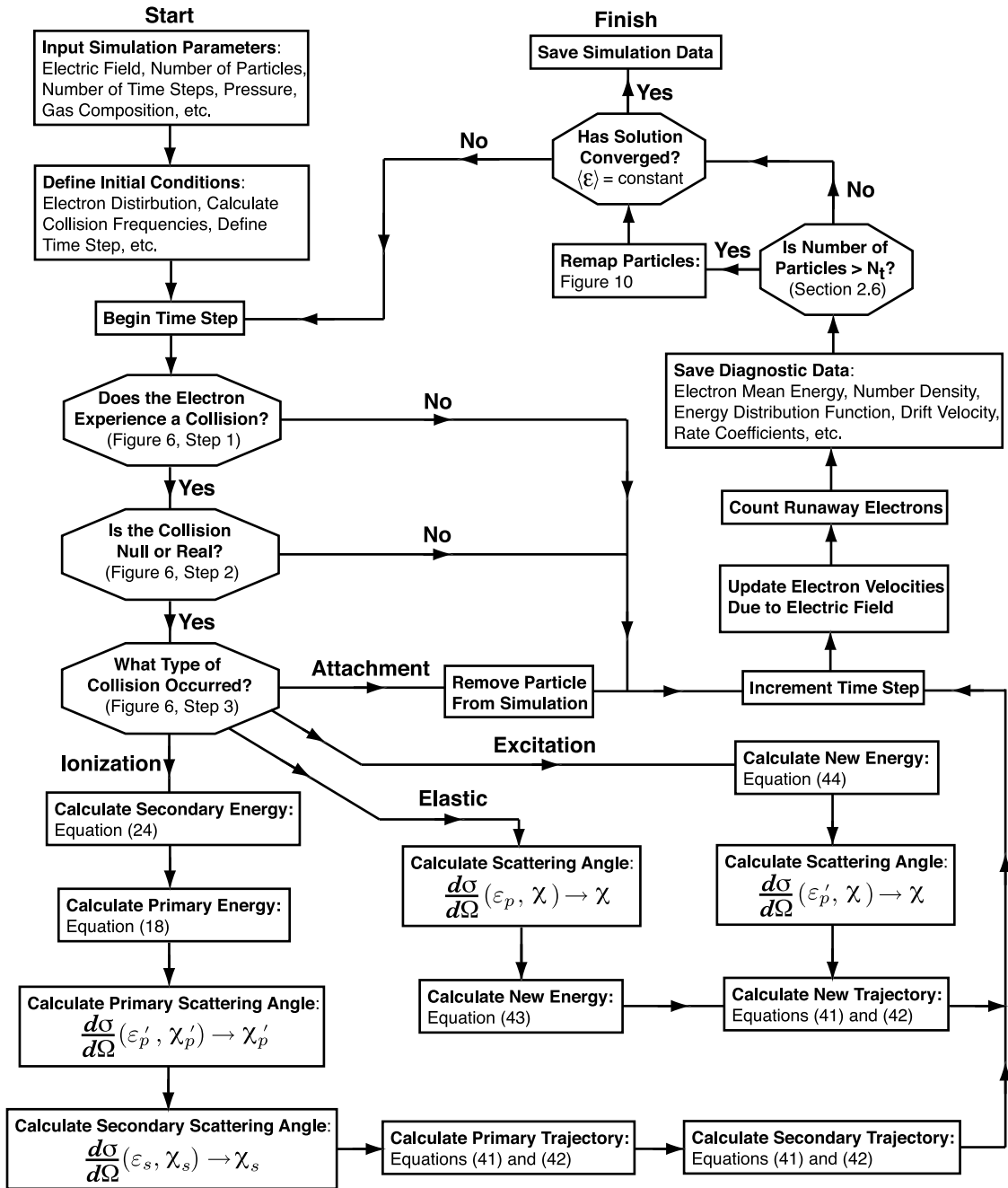


Figure 12. Flow chart depicting the execution of the Monte Carlo model.

sets (section 2.1) prior to the simulation to reduce computation time. These values are then loaded into the simulation at runtime and used to calculate the time step (equation (32)) and to determine if and what type of collision an electron experienced in a time step as outlined in Figure 6. In addition, the differential scattering cross section data discussed in section 2.1 is also tabulated prior to execution, allowing for convenient table lookups during the simulation to determine electron scattering after a collision.

[54] Each particle is then stepped through the “Null Collision Method” as summarized in Figure 6 to determine if it experienced a real collision in the time step, and if so, what type of collision occurred. If the electron experienced a real collision, the electron’s energy and trajectory are

updated corresponding to the type of collision as discussed in section 2.5. After all electrons have been stepped through the collisional part of the model, each electron’s parallel velocity ( $v_{\parallel}$ ) is updated to reflect the acceleration due to the electric field  $E$  during the time step  $\Delta t$  using a first-order finite-difference representation of Newton’s second law as  $v_{\parallel}^{\text{new}} = v_{\parallel}^{\text{old}} - \frac{q_e}{m} E \Delta t$ .

[55] Diagnostic data is then saved to file to allow for time-dependent analysis of certain quantities to be calculated (section 2.8) after the simulation is complete (i.e., mean energy versus time, drift velocity versus time, rate coefficients, etc.). If a certain number of particles has been reached, the particle assembly is then remapped (section 2.6) in order to maintain reasonable computation

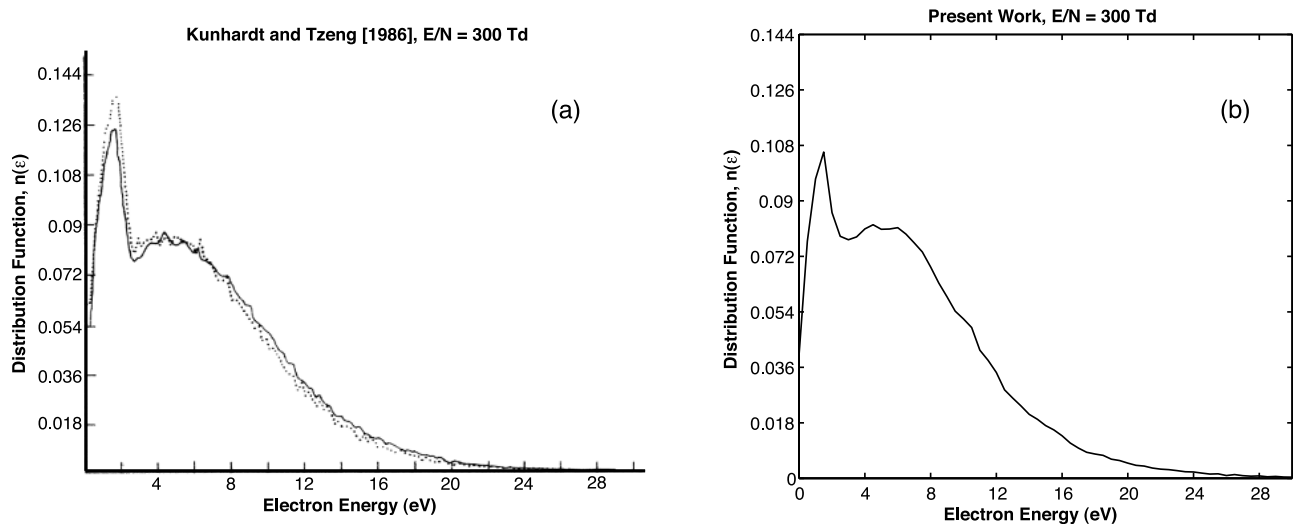


**Figure 13.** (a) Electron energy distribution in  $N_2$  at  $E/N = 300$  Td as presented by *Kunhardt and Tzeng* [1986a] (where the dotted line corresponds to results obtained when electron scattering is considered to be isotropic and the solid line corresponds to results obtained when electron scattering was determined using differential cross sections from experiment and theory) and (b) as calculated in the present work. Figure 13a is reprinted with permission from [Kunhardt and Tzeng, 1986a]. Copyright 1986 by the American Physical Society.

times. It is then checked to determine if the simulation has converged to a steady state (i.e., mean energy and drift velocity remain constant over a certain time span). If the simulation has converged, then the simulation data is saved to file; if not, the simulation returns to the beginning of the next time step and the procedure is repeated until a converging solution is reached.

## 2.8. Model Diagnostics

[56] The electron energy distribution  $n(\varepsilon)$  (normalized as  $\int_0^\infty n(\varepsilon) d\varepsilon = 1$ ) is obtained by sampling and averaging the electron assembly at several moments of time as the simulation reaches equilibrium. At each moment of time, the particles are divided into equally spaced bins along the energy  $\varepsilon$  axis and the particles weights  $W_j$  are summed to obtain the true number of electrons existing in each energy bin. The resulting functions are then normalized and averaged in time and the final distribution function  $n(\varepsilon)$  is normalized again

$$n(\varepsilon) = \frac{n(\varepsilon)}{\int_0^{\varepsilon_{\max}} n(\varepsilon) d\varepsilon} \quad (51)$$

to ensure that  $\int_0^{\varepsilon_{\max}} n(\varepsilon) d\varepsilon = 1$ , where  $\varepsilon_{\max}$  is the maximum electron energy.

[57] The electron mean energy can be simply calculated by summing the energy of each particle included in the simulation

$$\langle \varepsilon \rangle = \frac{\sum_{j=1}^{N_t} W_j \varepsilon_j}{n_t}, \quad (52)$$

where  $W_j$  and  $\varepsilon_j$  are the weight and energy of the  $j$ th particle, respectively,  $N_t$  is the total number of particles in the

simulation, and  $n_t$  is the total number of electrons which can be defined as

$$n_t = \sum_{j=1}^{N_t} W_j. \quad (53)$$

This calculation is performed at every time step and the result is used to determine if the simulation has reached an equilibrium state. Likewise, considering that the electron velocity is represented by its parallel and perpendicular velocity (Figure 9a, equations (38) through (40)), the drift velocity can be found by

$$v_d = \frac{\sum_{j=1}^{N_t} W_j v_{\parallel j}}{n_t}. \quad (54)$$

The electron mobility can then be calculated as

$$\mu_e = \frac{|v_d|}{|E|}. \quad (55)$$

[58] After a simulation has reached a steady state, the rate coefficients for various collision processes can be determined by simple counting procedures over a given time interval. First, consider a dummy variable  $C_i(t)$  which is used to count the occurrences of an ionization process over a given time interval. Each time an ionization collision occurs, the counter  $C_i(t)$  is incremented as

$$C_i(t) = C_i(t) + W_j, \quad (56)$$

where  $W_j$  is the weight of the particle experiencing the collision. The rate coefficient for this ionization process can be obtained by selecting two moments in time  $t_1$  and  $t_2$  after

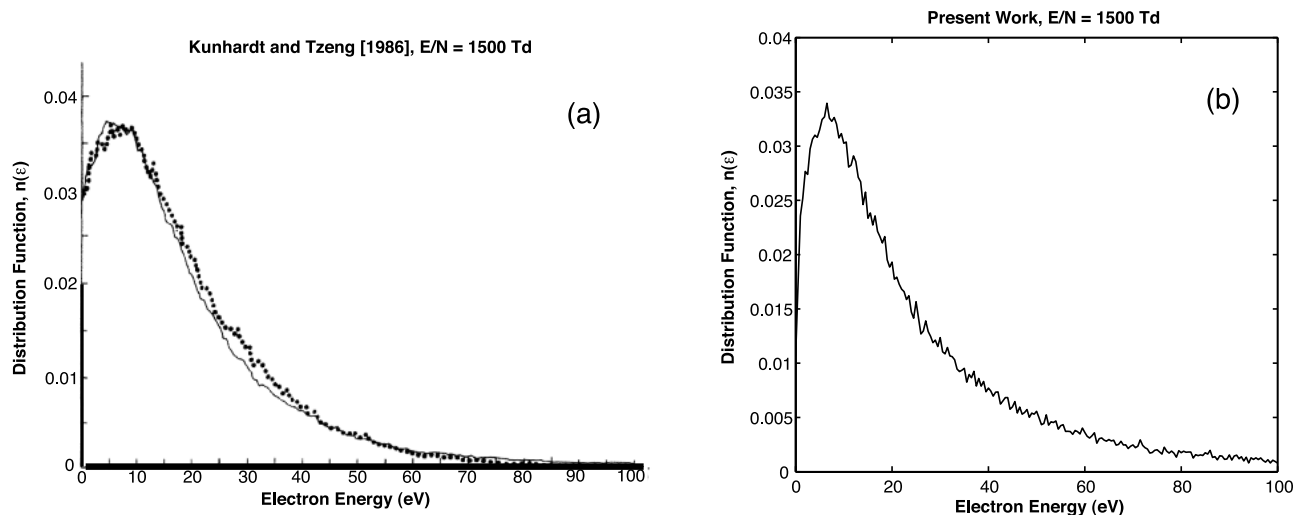


**Figure 14.** (a) Electron energy distribution in  $N_2$  at  $E/N = 1500$  Td as presented by *Kunhardt and Tzeng* [1986a] (where the dotted line corresponds to results obtained when electron scattering is considered to be isotropic and the solid line corresponds to results obtained when electron scattering was determined using differential cross sections from experiment and theory) and (b) as calculated in the present work. Figure 14a is reprinted with permission from [*Kunhardt and Tzeng*, 1986a]. Copyright 1986 by the American Physical Society.

the simulation has reached an equilibrium state. The ionization rate coefficient can then be calculated as

$$v_i = \frac{C_i(t_2) - C_i(t_1)}{\int_{t_1}^{t_2} n_t(t) dt}, \quad (57)$$

where  $n_t(t)$  is the total number of electrons as a function of time defined by equation (53). This calculation can be applied to any collision process (e.g.,  $\nu_{a2}$  two-body attachment,  $B^3\Pi_g$  excitation of  $N_2$ ,  $C^3\Pi_u$  excitation of  $N_2$ , etc.) for which a corresponding counter  $C_k(t)$  was maintained during the simulation. The meaning of the procedures defined by equations (56) and (55) can best be understood by direct integration of the dynamic equations describing the growth of the total number of electrons  $n_t$  due to ionization

$$\frac{dn_t}{dt} = v_i n_t \quad (58)$$

or the growth of the total number of excited species  $n_k$  due to impact excitation by electrons

$$\frac{dn_k}{dt} = \nu_k n_t. \quad (59)$$

### 3. Zero-Dimensional Calculations and Model Validation

[59] To test the precision and accuracy of the newly developed Monte Carlo model, zero-dimensional simulations were performed to compare with previously published Monte Carlo models, numerical solutions of the Boltzmann equation, and existing experimental data. For these compar-

isons the spatial distribution of electrons was ignored with only parallel ( $v_{\parallel}$ ) and perpendicular ( $v_{\perp}$ ) velocity components with respect to the applied electric field being considered.

#### 3.1. Comparisons With Previous Monte Carlo Model Results

[60] Figures 13, 14, and 15 show calculation comparisons of the electron energy distribution function  $n(\epsilon)$  in  $N_2$  gas at ground pressure from the current Monte Carlo model and the Monte Carlo model of *Kunhardt and Tzeng* [1986a]. For each simulation an assembly of 8000 electrons with an initially Maxwellian velocity distribution (electron temperature  $T_e = 0.5$  eV) was placed under the influence of a uniform electric field and the simulation was performed until the assembly reached an equilibrium state. High-energy ( $\epsilon > 500$  eV) angular scattering of electrons was determined using equation (14) and remapping was performed when the total number of particles reached a value  $N_t > 15,000$ .

[61] The electron energy distribution function is shown for  $E/N$  values of 300 Td and 1500 Td ( $1 \text{ Td} = 10^{-17} \text{ V cm}^2$ ). Figures 13a and 14a are results presented by *Kunhardt and Tzeng* [1986a] corresponding to “model 3” of their study in which elastic and inelastic collisions were taken to be anisotropic and differential scattering cross sections were obtained from experiment and theory. For the same scattering consideration, the results of the present model are shown in Figures 13b and 14b. The energy distributions shown in Figures 13a and 13b demonstrate the same shape characteristics with the sharp peak in the number of electrons existing below 2 eV being  $\approx 15\%$  lower in the current calculations. This is most likely due to the use of updated collision cross section and differential cross section data in the current model, as compared to *Kunhardt and Tzeng* [1986a]. Similarly, Figures 14a and 14b also demonstrate the same

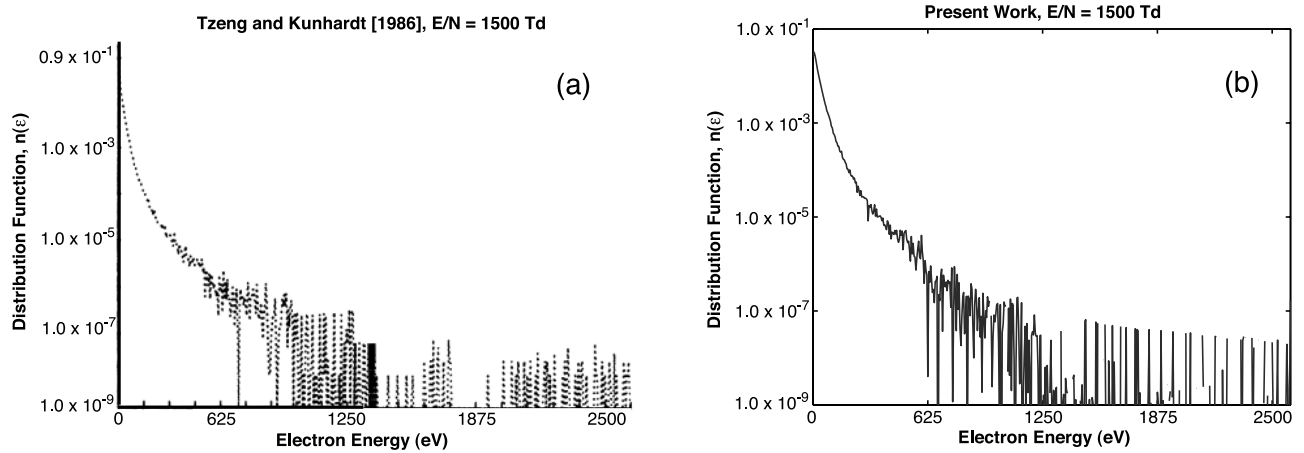


**Figure 15.** (a) High-energy tail of the electron energy distribution in  $N_2$  at  $E/N = 1500$  Td as presented by Tzeng and Kunhardt [1986] and (b) as calculated in the present work. Figure 15a is reprinted with permission from [Tzeng and Kunhardt, 1986]. Copyright 1986 by the American Physical Society.

overall shape with a  $\approx 7\%$  lower peak value for the same reason. It can be seen that for  $E/N = 1500$  Td the high-energy tail of the distribution extends to energies  $\sim 100$  eV and with further inspection of the tail, Figures 15a and 15b show the population of thermal runaway electrons existing at energies  $\gg 100$  eV. The nonsmooth appearance of the distribution seen in Figure 15 is due to the small number of particles being sampled in these high-energy regions. Figure 15a corresponds to “Case 2” presented by Tzeng and Kunhardt [1986] in which the energy of secondary electrons emerging from ionizing collisions is determined from the differential ionization cross section of Opal *et al.* [1971] as discussed in section 2.3. Kunhardt and Tzeng [1986a] emphasize that the treatment of angular scattering

can have a great effect on the electron energy distribution function. While the variations displayed in the low-energy portion of the distribution are small, assumptions about angular scattering of electrons can significantly inhibit or promote the development of runaway as will be shown in sections 3.3, 4.1, and 4.2.

### 3.2. Comparisons With ELENDF, Experimental Results, and Previous Models

[62] Figures 16, 17, and 18 show the energy distribution function  $n(\epsilon)$ , mean energy  $\langle \epsilon \rangle$ , phase space velocity distribution, and drift velocity  $v_d$  of electrons in an air mixture at ground pressure consisting of 78.11%  $N_2$ , 20.91%  $O_2$ , and 0.98%  $Ar$  under the influence of applied

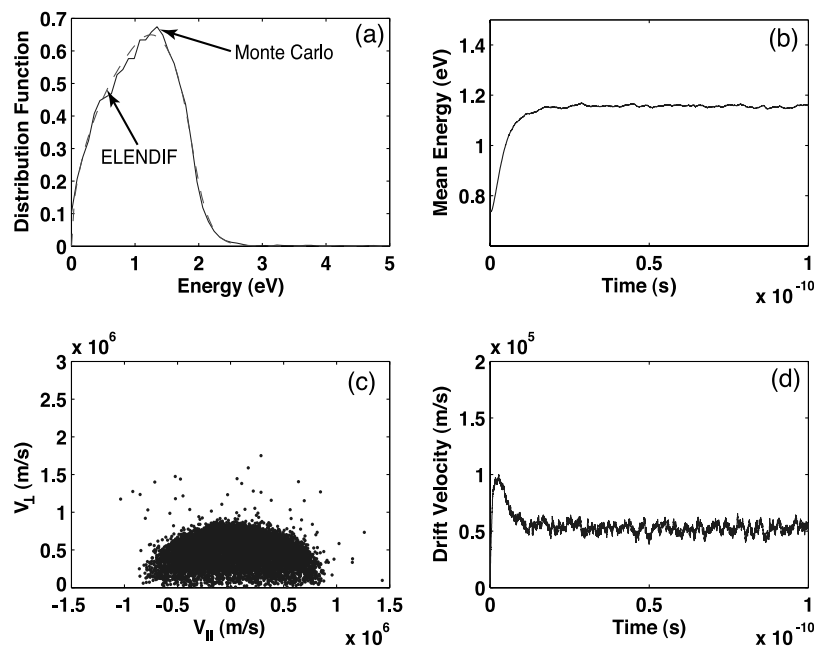


**Figure 16.** (a) Electron energy distribution function, (b) electron mean energy, (c) electron velocity distribution in phase space, and (d) electron drift velocity in air under the influence of an electric field  $E = 0.3E_k$ .

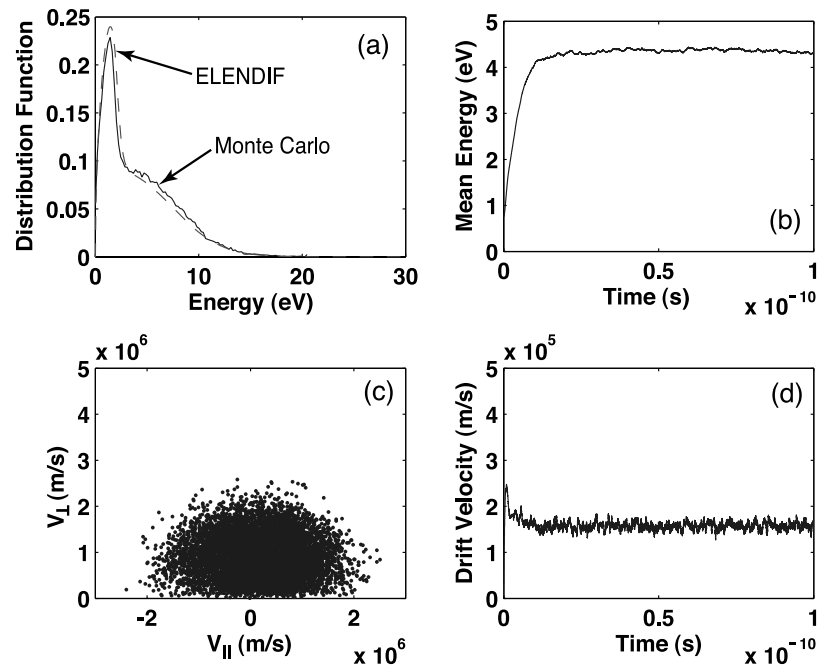


**Figure 17.** (a) Electron energy distribution function, (b) electron mean energy, (c) electron velocity distribution in phase space, and (d) electron drift velocity in air under the influence of an electric field  $E = 1.2E_k$ .

electric fields  $E = 0.3E_k$ ,  $E = 1.2E_k$ , and  $E = 20E_k$ , respectively, where  $E_k$  is the previously defined conventional breakdown field. As in section 3.1, an assembly of 8000 electrons with an initially Maxwellian velocity distribution (electron temperature  $T_e = 0.5$  eV) was used. Equation (14) was utilized to determine high-energy ( $\epsilon > 500$  eV for collisions with  $N_2$  and  $\epsilon > 1000$  eV for collisions with  $O_2$  and  $Ar$ ) angular scattering of electrons and remapping was performed when the number of particles reached  $N_t > 15,000$ .

[63] The electron distribution function in Figures 16a, 17a, and 18a are compared to results obtained from the ELeNDIF Boltzmann equation solver [Morgan and Penetrante, 1990]. It can be seen that for low field values  $E = 0.3E_k$  and  $E = 1.2E_k$  the energy distributions obtained from the current Monte Carlo model are in excellent agreement with results obtained from the ELeNDIF software with differences of  $<5\%$  and  $\approx 5\%$ , respectively. Also, Figures 16a and 17a provide an excellent insight into the dynamic friction force in air (section 1.2, Figure 2). Figure 16a shows that the majority of the electron population under the influence of an electric field  $E = 0.3E_k$  is maintained at energies  $<2$  eV. Electrons are held at these low energies because of the  $N_2$  vibrational processes with threshold energies ranging from 0.28 eV to 2.35 eV (see Table 1) constituting the “first bump” of the dynamic friction force (Figure 2). The electrons lose more energy to these vibrational collisions than they gain from the applied electric field. For an electric field  $E = 1.2E_k$ , however, it becomes possible for electrons to gain more energy from the electric field than they lose to these vibrational processes. As can be seen in Figure 17a, a large population of electrons remain at energies  $<2$  eV due to vibrational collisions, but a significant number is able

to penetrate through the vibrational barrier and is accelerated to energies  $>2$  eV. These electrons, however, do not accelerate to higher energies because of the increased collision frequency and energy loss corresponding to the 100 eV “hump” of the dynamic friction force (Figure 2). Figure 18a shows the energy distribution of electrons when an electric field  $E = 20E_k$ , much greater than the thermal runaway field  $E_c$ , is applied and a large percentage of the total electron population is accelerated to energies  $>100$  eV. It can also be seen in Figure 18a that the two-term spherical harmonic expansion [e.g., Raizer, 1991, chap. 5] used in the ELeNDIF solution fails at this high electric field value and the Monte Carlo and ELeNDIF results no longer agree. Figures 16b, 17b, and 18b show the simulation reaching an equilibrium state as the mean energy converges to a constant value for each of the electric field cases and Figures 16d, 17d, and 18d show the average drift velocity of electrons also converging. It can be seen from Figure 18b that the mean energy of electrons is only  $\sim 60$  eV, showing that even for an extremely high electric field  $E = 20E_k$ , it is still very difficult for electrons to accelerate to energies  $>100$  eV and only a small fraction of them becomes runaway. Figures 16c, 17c, and 18c show the phase space velocity distributions of particles in the system. Figures 16c and 17c confirm that for electric fields  $E = 0.3E_k$  and  $E = 1.2E_k$  the velocity distributions remain largely isotropic, thus justifying the two-term spherical harmonic expansion used in the ELeNDIF solution. On the contrary, Figure 18c shows that for  $E = 20E_k$  the velocity distribution becomes highly anisotropic because of thermal runaway electrons and therefore the two-term spherical harmonic expansion can no longer be utilized in the solution of the Boltzmann equation.

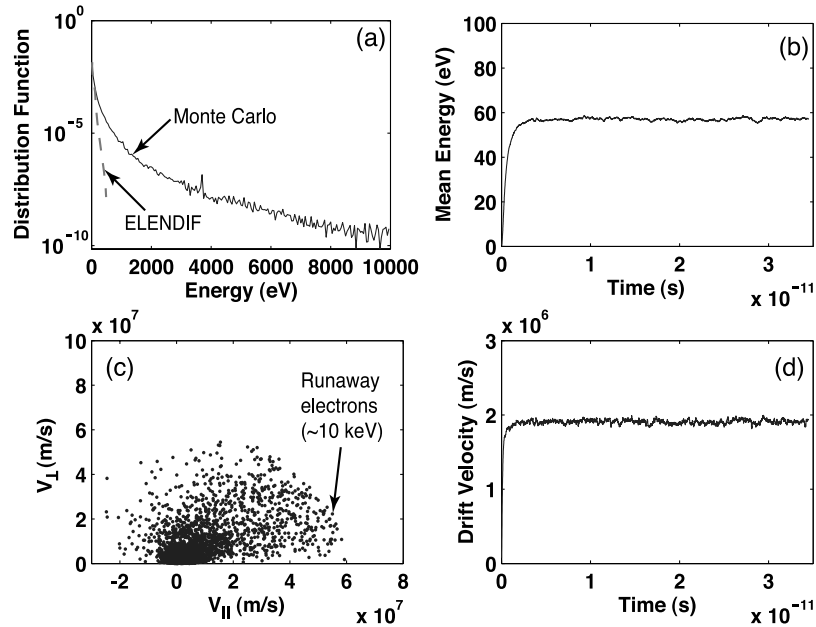


**Figure 18.** (a) Electron energy distribution function, (b) electron mean energy, (c) electron velocity distribution in phase space, and (d) electron drift velocity in air under the influence of an electric field  $E = 20E_k$ .

[64] Figures 19 through 22 show results of Monte Carlo model calculations compared to results obtained from ELENDIF, experimental swarm parameter measurements in dry air reported by *Davies* [1983], and from related analytical model approximations proposed by *Aleksandrov et al.* [1995] and *Morrow and Lowke* [1997] for a range of applied electric fields. Figure 19a shows that the electron mean energy calculated by the Monte Carlo model agrees well with the ELENDIF Boltzmann code at most electric fields, demonstrating only a slight deviation of  $\approx 25\%$  at  $E = 6 \times 10^7$  V/m. The Monte Carlo calculation of electron mobility  $\mu_e$  shown in Figure 19b shows excellent agreement with the experimental values of *Davies* [1983] and ELENDIF calculations for electric fields ranging

from  $E = 5 \times 10^5$  to  $E = 1 \times 10^7$  V/m but demonstrates a percent difference of  $\approx 38\%$  with ELENDIF calculations at  $E = 6 \times 10^7$  V/m. However, the Monte Carlo mobility calculation agrees well with the model approximation of *Morrow and Lowke* [1997] for electric fields  $> 1 \times 10^7$  V/m. It can be seen in Figure 20a that the ionization coefficient calculated by the Monte Carlo model demonstrates excellent agreement with experimental measurements [*Davies*, 1983], ELENDIF calculations, and the model of *Aleksandrov et al.* [1995] at all electric field values, but displays a difference of  $\approx 68\%$  with the model of *Morrow and Lowke* [1997] at  $E = 6 \times 10^7$  V/m. The values calculated and reported for the two body attachment coefficient  $\nu_{a2}$  vary greatly, as can be seen in Figure 20b.

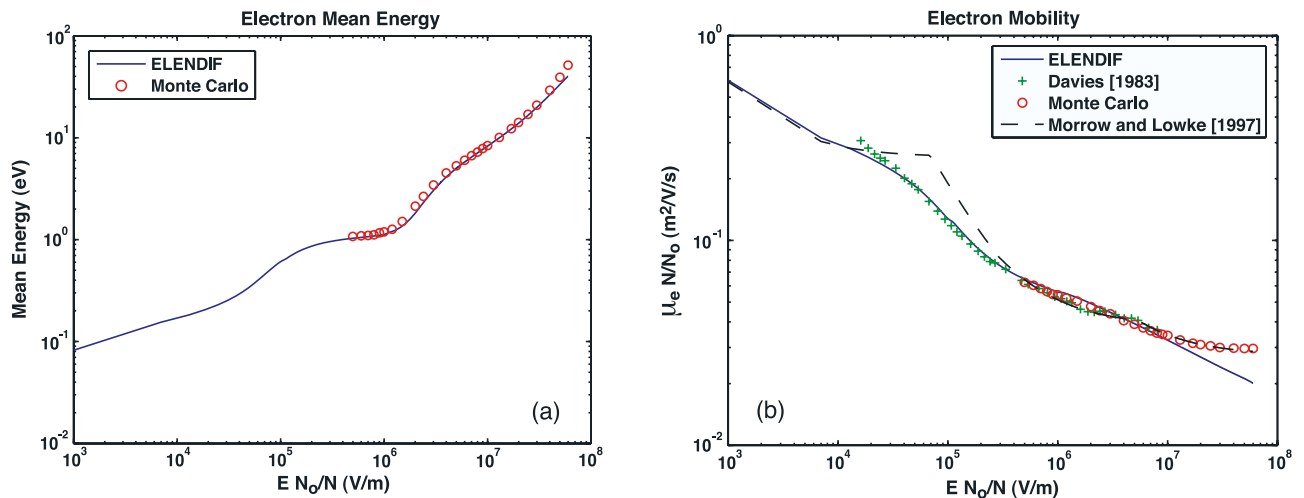


**Figure 19.** (a) The electron mean energy  $\langle \varepsilon \rangle$  and (b) electron mobility  $\mu_e$  in air as a function of applied electric field.

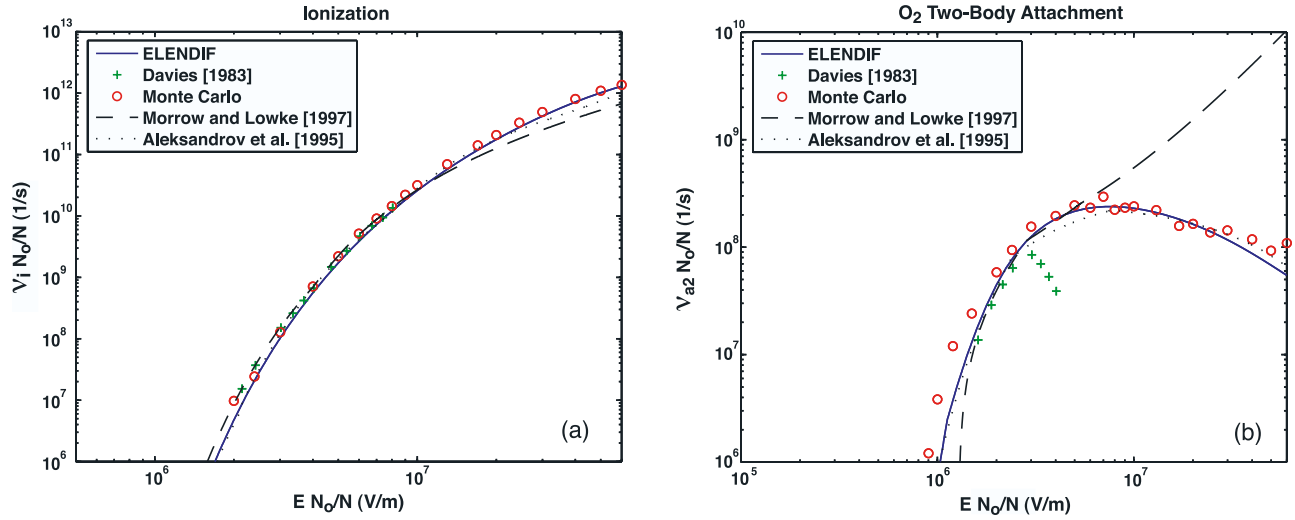


**Figure 20.** (a) The total ionization coefficient  $\nu_i$  and (b)  $O_2$  two-body attachment coefficient  $\nu_{a2}$  in air as a function of applied electric field.

The results of  $\nu_{a2}$  calculated by the Monte Carlo model agree well with the model of *Aleksandrov et al.* [1995] and ELENDIF calculations for electric fields  $> 2 \times 10^6$  V/m but are significantly higher at fields  $< 2 \times 10^6$  V/m. The Monte Carlo  $\nu_{a2}$  calculations demonstrate a difference of up to  $\approx 58\%$  compared to experimental values, with the sharp decline in the  $\nu_{a2}$  values of *Davies* [1983] for  $E > 3 \times 10^6$  V/m not being reproduced by Monte Carlo and ELENDIF solutions. This is most likely due to the presence of collisional detachment, which is not included in the Monte Carlo and ELENDIF calculations, impacting the experimental results [*Davies*, 1983]. It also can be seen from Figures 21 and 22 that the excitation coefficients of the  $B^3\Pi_g$  and  $C^3\Pi_u$  states of  $N_2$  and the  $B^2\Sigma_u^+$  state of  $N_2^+$  obtained from the Monte Carlo model agree well with results obtained from ELENDIF at high electric field values but show better agreement with the calculation of *Aleksandrov et al.* [1995] at lower electric fields. The  $B^2\Sigma_u^+$

optical excitation coefficients shown in Figure 22 were calculated by obtaining the ionization rate coefficients of  $N_2$  from the Monte Carlo model (see section 2.8), ELENDIF calculations, and approximations of *Aleksandrov et al.* [1995], and then multiplying the resulting coefficients by a branching ratio ( $f_B = 0.145$ ) presented by *Van Zyl and Pendleton* [1995].

[65] These results indicate that although the two-term spherical harmonic expansion is not generally valid at high electric field values, the above rate coefficients obtained from ELENDIF remain valid for electric fields up to  $6 \times 10^7$  V/m ( $\approx 20E_k$ ). The differences between Monte Carlo and ELENDIF calculations of electron mean energy and mobility at high electric fields are most likely due to the electron distribution becoming anisotropic.

[66] We note that results of Figures 19 through 22 are presented in a reduced form using the ratio of the air density at ground pressure  $N_0 = 2.688 \times 10^{19} \text{ cm}^{-3}$  to the density at

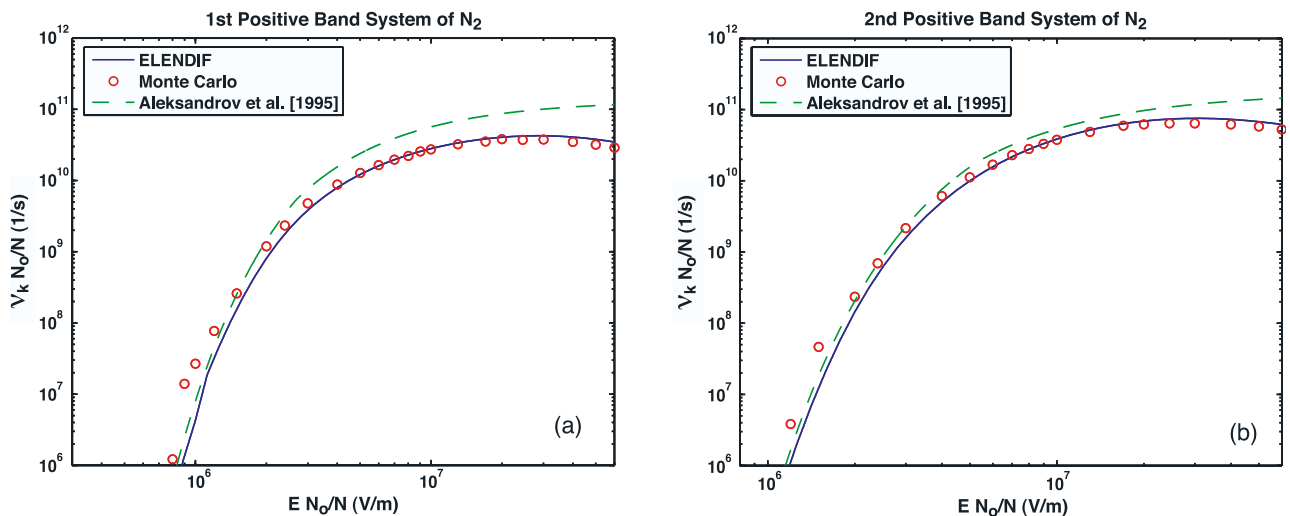


**Figure 21.** (a) The first positive band system of  $N_2$  ( $B^3\Pi_g$  state) and (b) second positive band system of  $N_2$  ( $C^3\Pi_u$  state) optical excitation coefficients in air as a function of applied electric field.

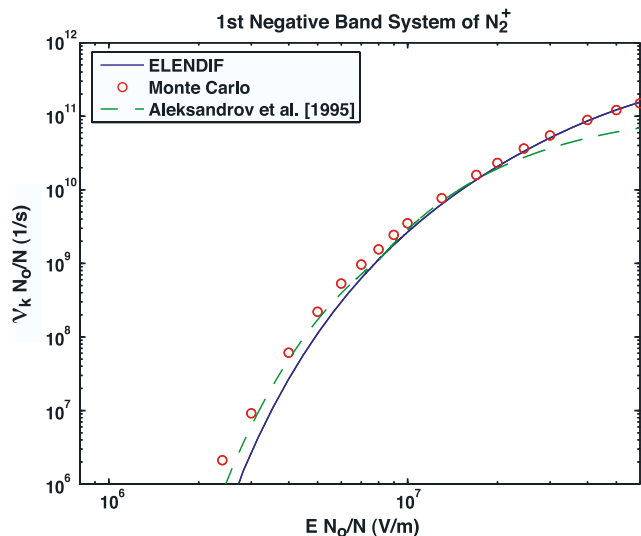


**Figure 22.** First negative band system of  $N_2^+$  ( $B^2\Sigma_u^+$  state) optical excitation coefficient in air as a function of applied electric field.

any other pressure  $N$ . This scaling is justified by the similarity properties of gas discharges [e.g., *Liu and Pasko*, 2004, and references therein] and can be directly used for calculation of physical quantities at any other air density  $N$  of interest.

[67] A MATLAB function, based on ELENDIF solutions, was used in the plotting of Figures 19 through 22. This function allows the calculation of many physical quantities and rate coefficients as a function of the reduced electric field in air and is freely available to readers as a supplement to this paper at <http://pasko.ee.psu.edu/air>.

### 3.3. Runaway Electron Development

[68] To examine the development of runaway electrons for various electric fields, simulations were conducted to perform direct comparisons with recent results presented by *Bakhov et al.* [2000]. An initial assembly of 1 eV electrons ( $N_0 = 5000$ ) with velocities unidirectional with the electric force was placed in  $N_2$  gas at ground pressure with applied electric fields of 400 kV/cm, 350 kV/cm, and 325 kV/cm, and simulated for times of  $t = 1$  ns,  $t = 6$  ns, and  $t = 25$  ns, respectively. In accordance with *Bakhov et al.* [2000], the following nitrogen electronic states were considered (see Table 1):  $A^3\Sigma_u^+$  ( $v = 5-9$  and  $v = 10+$ ),  $B^3\Pi_g$ ,  $W^3\Delta_u$ ,  $B^3\Sigma_u^-$ ,  $C^3\Pi_u$ ,  $w^1\Delta_u$ ,  $a^1\Pi_g$ , and the sum of the remaining singlet states (threshold  $\epsilon = 13$  eV). Elastic and ionization collisions were also considered; however, while ionization was considered as an energy loss mechanism, secondary electrons were not added to the particle assembly. When electrons reached an energy equal to  $\epsilon_{\max} = 4000$  eV, they were considered to be runaway and removed from the simulation.

[69] Figure 23 shows results of the Monte Carlo model of *Bakhov et al.* [2000], in which angular scattering of high-energy electrons after elastic and ionization collisions is determined from the electron data library (EEDL) [Perkins and Cullen, 1994] and is adopted to be forward after excitation collisions. Figure 24 shows similar results

calculated by the Monte Carlo model discussed in this paper, where high-energy angular scattering has been determined by the differential scattering cross section approximation published by *Kol'chuzhkin and Uchaikin* [1978] (equation (14), Figure 24a) and the modified Rutherford cross section introduced in this paper (equation (16), Figure 24b). A direct inspection of the atomic nitrogen data presented in the EEDL library at selected energies of 1, 2.5, and 5 keV indicates that among the models discussed in section 2.2 of this paper the corresponding differential cross sections are closest to the approximation given by equation (9).

[70] Recalling that low-energy ( $\epsilon < 500$  eV) electron scattering is determined by the experimentally determined differential cross sections listed in Table 5 for all simulations, the only difference between the simulations of Figure 24a and 24b is the differential scattering cross section used for energies  $>500$  eV. It is obvious from the major differences shown in Figures 24a and 24b that the high-energy scattering of electrons is critical in the development of electron runaway. Comparison of Figures 4c and 4d show that the differential scattering cross section calculated from equation (16) possesses a much larger forward scattering characteristic than that of equation (14) for all electron energies. The effect of this forward scattering on the development of runaway electrons is well illustrated in Figure 24 and by comparing Figures 23 and 24 it can be seen that results obtained by *Bakhov et al.* [2000] using EEDL data are similar to those obtained with our model using the differential scattering cross section calculated from equation (16). It can also be seen from Figure 24a that assuming forward scattering after excitation collisions drastically increases the production of runaway electrons when equation (14) is used. This is not the case when the same assumption is used with equation (16) since equation (16) already possesses a strong forward scattering characteristic.

[71] Also of interest are the considerable differences in Figures 24a and 24b when forward scattering after excitation collisions is assumed. Since excitation collisions are forward for both cases, the elastic and ionization collisions must be responsible for the large differences in runaway

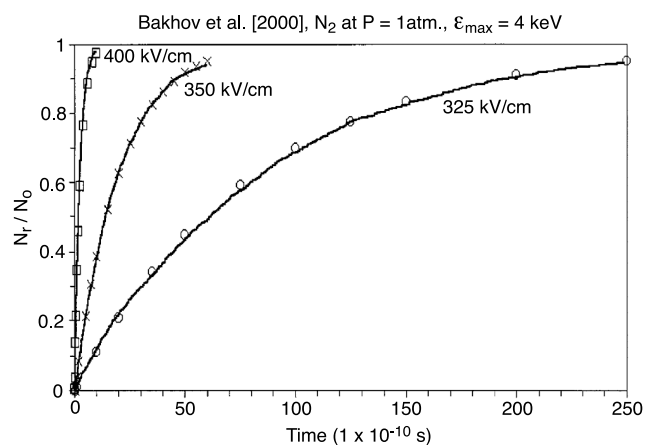


**Figure 23.** The fraction  $N_r/N_0$  of the initial electron assembly to reach energies  $\geq \epsilon_{\max} = 4000$  eV as calculated by *Bakhov et al.* [2000]. Copyright 2000 by the IEEE.

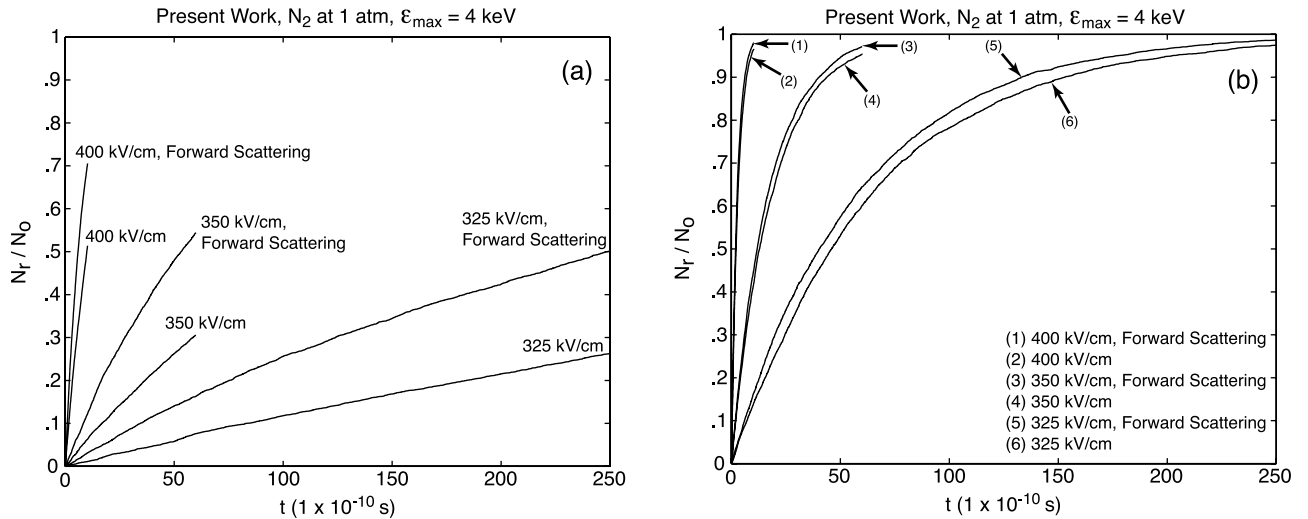


**Figure 24.** The fraction  $N_r/N_0$  of the initial electron assembly to reach energies  $\geq \varepsilon_{\max} = 4000$  eV calculated by the Monte Carlo model developed in this paper with high-energy angular scattering determined from (a) equation (14) and (b) equation (16). Results are shown with and without the assumption of forward scattering after high-energy ( $\varepsilon > 500$  eV) excitation collisions.

electrons observed. While elastic collisions are the dominant collision process at low electron energies, the differences in Figures 24a and 24b are most likely due to the high-energy scattering of the primary electron after ionizing collisions. This leads to an interesting conclusion that the high-energy angular scattering from ionizing collisions is much more important in the development of electron runaway than high-energy scattering from excitation collisions.

#### 4. One-Dimensional Streamer Tip Simulations

[72] In this section the Monte Carlo model discussed in the previous sections is modified to study the production of runaway electrons in streamer tips. The model calculations are conducted for a case of streamers at an air pressure corresponding to 70 km altitude ( $p = 0.05$  Torr). Owing to the similarity properties of streamers [Liu and Pasko, 2004, and references therein] the reported results can be generalized to air streamers existing in systems at any pressure of interest (i.e., those discussed in section 1.1). The electric field is assumed to be unidirectional with the  $z$ -axis and electron velocities are still considered in terms of their perpendicular ( $v_{\perp}$ ) and parallel ( $v_{\parallel}$ ) components with respect to the applied electric field (see Figure 9). The electron positions were tracked along the  $z$ -axis and updated at the end of each time step according to

$$z' = z + v_{\parallel} \cdot \Delta t, \quad (60)$$

where  $z$  is the initial position of the electron and  $z'$  is the new position. All simulations are performed in an air mixture consisting of 78.11%  $N_2$ , 20.91%  $O_2$ , and 0.98% Ar utilizing the cross sections listed in section 2.1.

##### 4.1. Stationary Streamer Tip Model

[73] To demonstrate the importance of high-energy angular scattering in the development of runaway electrons in a

streamer tip, four different cases utilizing the differential scattering cross section of *Kol'chuzkin and Uchaikin* [1978] (equation (14)) and the modified Rutherford cross section of equation (16) were considered. It can be seen from Figures 4 and 5 that these two cross sections possess very different scattering properties which greatly influence the development of runaway electrons as shown in Figure 24. As in section 3.3, simulations were performed for both cross sections with and without the assumption of forward scattering after excitation collisions.

[74] The strong electric field associated with a streamer tip immediately preceding branching (Figure 1) is approximated by a  $10 E_k$  square pulse spanning 1 m in  $z$ -space and is placed in various ambient electric fields  $E_{\text{amb}}$  (Figure 25a). We note that in accordance with similarity laws [e.g., Liu and Pasko, 2004], the streamer spatial scales (i.e., width of the streamer tip) and electric fields scale with air density  $N$  as  $\sim 1/N$  and  $\sim N$ , respectively. Therefore the maximum energy, which can be gained by electrons in the streamer tip, remains the same for similar streamers at different air densities, or pressures (assuming constant gas temperature). The magnitude of the electric field in the streamer tip ( $10E_k = 2170$  V/m) and the tip width (1 m) shown in Figure 25 correspond to a model streamer at 70 km altitude (Figure 1). As mentioned above, all results reported in this section can be easily generalized to streamers at other altitudes (pressures) of interest using similarity laws.

[75] The two quantities of interest are the runaway production rate  $\nu_{\text{run}}$  [1/s] and the runaway flux  $\Gamma_{\text{run}}$  [1/m<sup>2</sup>/s]. The runaway production rate  $\nu_{\text{run}}$  is defined as the rate at which electrons inside the streamer tip volume reach energies greater than a predefined runaway energy  $\varepsilon_{\text{run}}$ . The runaway flux  $\Gamma_{\text{run}}$  represents the number of electrons with energies greater than  $\varepsilon_{\text{run}}$  which pass through a unit area 1 m in front of the streamer tip per unit time. The distance of 1 m in front of the streamer tip was arbitrarily chosen such that the focus of our study is placed on the number of runaway electrons produced by streamer tips and

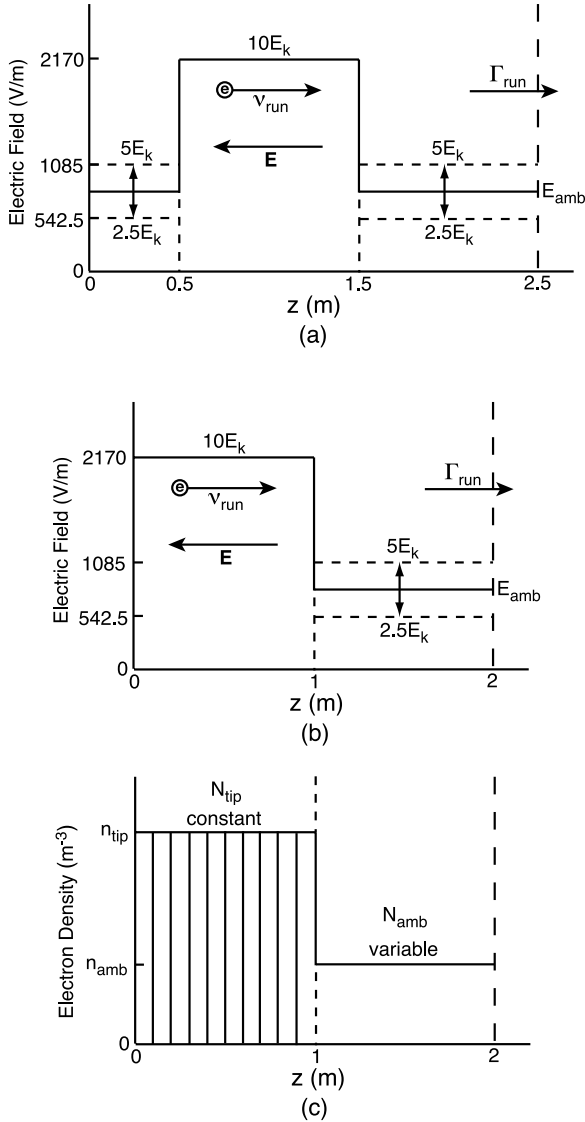


**Figure 25.** (a) and (b) The simplified electric field and (c) electron density configuration corresponding to a model approximation of a streamer tip at 70 km used in one-dimensional Monte Carlo simulations.

not the future evolution of these electrons. Figure 26 shows the geometry and a sample calculation of  $\nu_{run}$  and  $\Gamma_{run}$  for a case when the ambient field is assigned a value of  $E_{amb} = 4E_k$  and equation (16) was used to determine all angular scattering. Plotting the cumulative number of runaway electrons generated within the streamer tip volume  $N_{run}$  and the number of runaway electrons to pass through the unit area 1 m ahead of the streamer tip  $N_{run-flux}$  as functions of time, allows the rates  $\nu'_{run}$  and  $\Gamma'_{run}$  to be calculated (see Figure 26). These rates may then be scaled to realistic values  $\nu_{run}$  and  $\Gamma_{run}$  corresponding to a streamer tip electron density  $n_e$  at 70 km of  $10^{12} m^{-3}$  [Liu and Pasko, 2004] as

$$\nu_{run} = \frac{n_e}{n_{tip}} \times \nu'_{run} \quad (61)$$

$$\Gamma_{run} = \frac{n_e}{n_{tip}} \times \Gamma'_{run}, \quad (62)$$

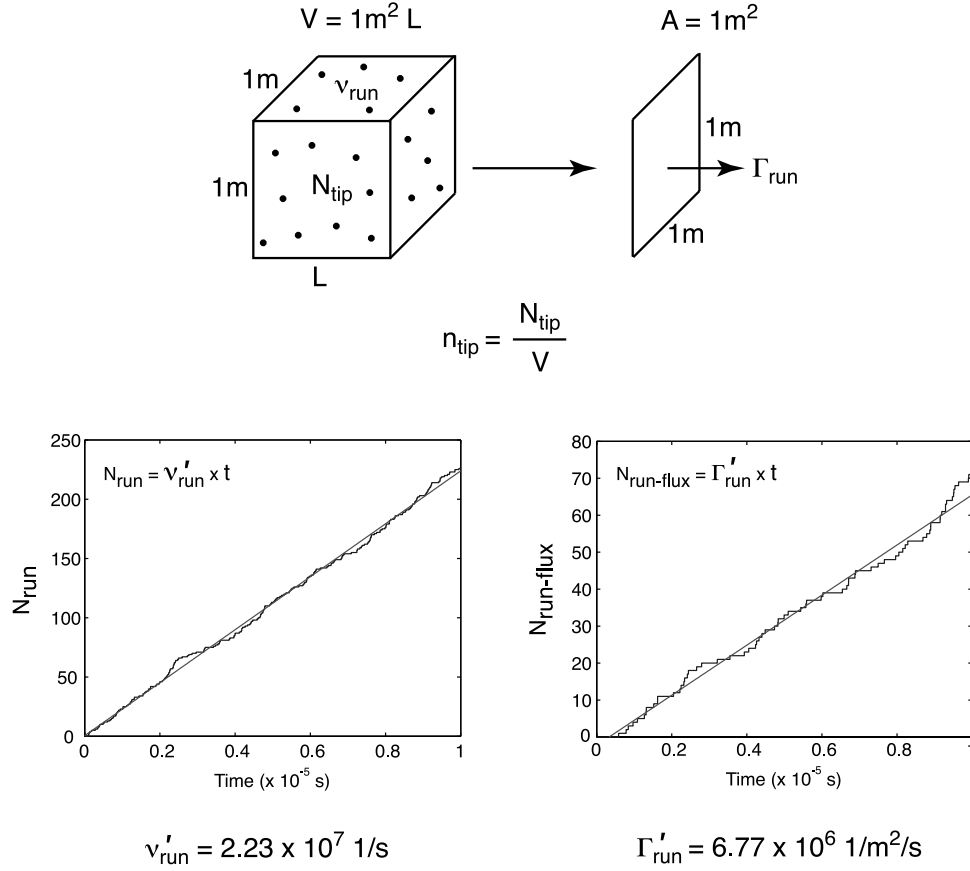
where  $n_{tip}$  is the electron density of the streamer tip in the simulation (see Figure 26). These values can then be generalized to streamers at other altitudes and pressures noting the similarity properties of streamers [Liu and Pasko, 2004, and references therein] following the relationship  $n_e = n_{e0} \frac{N^2}{N_0^2}$ , where  $n_{e0} = 2 \times 10^{20} m^{-3}$  is the reference streamer density at ground level, and  $N_0$  and  $N$  are defined in the paragraph before last of section 3.2.

[76] After performing a number of test simulations, it was determined that  $\nu'_{run}$  and  $\Gamma'_{run}$  are independent of the 0.5 m  $E_{amb}$  field region behind the streamer tip (Figure 25a), thus allowing the simulation domain to be reduced to two electric field regions (Figure 25b). This simplification allows for more electrons to be placed in the  $10E_k$  streamer tip region, which improves the statistics of the  $\nu'_{run}$  and  $\Gamma'_{run}$  calculations.

[77] In order to accurately represent the constant electron density of a propagating streamer tip [e.g., Liu and Pasko, 2004], the electron density was kept constant over the  $10E_k$  region throughout simulations using ten spatial bins (Figure 25c). After performing several test simulations, the electron density in the ambient field region  $n_{amb}$  was found to have no effect on  $\nu_{run}$  and  $\Gamma_{run}$  and therefore was allowed to be variable. At the end of each time step, the density of electrons in each of the ten bins ( $n_{bin}$ ) is calculated. The electron density in each bin is then compared with the desired constant  $n_{tip}$  to determine if there are too many or too few electrons in the bin. If  $n_{bin} > n_{tip}$ , then  $n_{bin} - n_{tip}$  electrons with energies less than 10 eV (ensuring that a runaway electron is not being repositioned) are randomly selected from the bin and 1 m is added to their current  $z$ -position thus moving them into the  $n_{amb}$  region. If  $n_{bin} < n_{tip}$ , then  $n_{tip} - n_{bin}$  electrons with energies less than 10 eV are randomly selected from the  $n_{amb}$  region and placed at the left boundary of the bin in question.

[78] This formulation results in a constant total number of electrons  $N_{tip}$  (see Figure 25c) being exposed to the high electric field of the streamer tip at all times throughout the simulation, but due to two-body and three-body attachment collisions with  $O_2$  (see Table 2) the total number of electrons in the low field region  $N_{amb}$  decreases slightly over time. Initial values of  $n_{tip}$  are normally chosen to be 150,000, 100,000, 75,000, 50,000, or 25,000  $m^{-3}$  depending on the resolution needed to obtain satisfactory statistics for various electric field and scattering cases, and  $n_{amb}$  is initially 20,000  $m^{-3}$  for all simulations.

[79] It should be noted that while ionization is considered as an energy loss mechanism for primary electrons, secondary electrons are not added to the simulation of the stationary streamer tip, and the one-dimensional remapping of particles discussed in section 2.6 was not utilized in the simulations. For an electric field of  $10E_k$  the ionization coefficient is  $\sim 7 \times 10^{11} \frac{N}{N_0} s^{-1}$  (see Figure 20), which leads to an enormous multiplication of electrons. If these secondary electrons are added to the simulation, as with the zero-dimensional model, the particle weights and electron density grow at an extremely fast pace. This fast growth is believed to be an inaccurate representation of the actual physical system in which the electron density in the streamer tip is dynamically maintained at relatively stable levels. The focus of this study is therefore placed on determining the number of initially cold electrons out of



For  $L = 1\text{m}$ ,  $V = 1\text{m}^3$ ,  $N_{\text{tip}} = 25000$ , and  $n_e = 10^{12} \text{ m}^{-3}$  at  $70 \text{ km}$ :

$$v_{\text{run}} = \frac{n_e}{n_{\text{tip}}} \times v'_{\text{run}} = 8.92 \times 10^{14} \text{ 1/s}$$

$$\Gamma_{\text{run}} = \frac{n_e}{n_{\text{tip}}} \times \Gamma'_{\text{run}} = 2.68 \times 10^{14} \text{ 1/m}^2/\text{s}$$

**Figure 26.** Simulation geometry and sample calculations of the runaway production rate  $v_{\text{run}}$  and the runaway flux  $\Gamma_{\text{run}}$  for a case at  $70 \text{ km}$  when  $E_{\text{amb}} = 4E_k$ , the streamer tip length is  $L = 1\text{m}$ , and the streamer tip density used in the simulation is  $n_{\text{tip}} = 25000 \text{ m}^{-3}$ .

a known constant electron density to reach runaway energies. This evolution of individually tracked runaway electrons can therefore be treated without consideration of the avalanche multiplication of electrons due to ionization. This assumption, however, relies heavily on the fact that most secondary electrons emerge from ionizing collisions with low energies. Simulations have shown that a small percentage of secondaries do possess energies  $>200 \text{ eV}$ , thus placing them over the “hump” of the dynamic friction force (Figure 2). These high-energy secondaries entering an electric field  $\sim 10 E_k$  have an increased probability of becoming runaway electrons and would impact the values of  $v_{\text{run}}$  and  $\Gamma_{\text{run}}$ . Several simulations were performed in which secondary electrons emerging from ionizing collisions with energies  $>200 \text{ eV}$  were added to the simulation and values of  $\Gamma_{\text{run}}$  were observed to increase by  $\approx 10\%$ .

[80] The energy required for an electron to be considered runaway  $\varepsilon_{\text{run}}$  is directly determined from the dynamic friction force of electrons in air (Figure 2). Figure 27a shows the values of  $\varepsilon_{\text{run}}$  corresponding to ambient electric fields of  $1 E_k$ ,  $2 E_k$ ,  $3 E_k$ ,  $4 E_k$ , and  $5 E_k$ . It can be seen from Figure 2a that these ambient fields alone are not strong enough to overcome the friction force  $F_D$  and accelerate low-energy electrons to energies  $>100 \text{ eV}$ . An electric field of  $10E_k$ , however, falls above the peak of  $F_D$  and it becomes possible for electrons exposed to a  $10 E_k$  field to be accelerated to energies  $>100 \text{ eV}$ . In view of the electric field configuration shown in Figure 25b, the  $10E_k$  streamer tip field extending over  $1 \text{ m}$  length is solely responsible for all runaway electrons produced during a simulation, and the magnitude of the ambient field  $E_{\text{amb}}$  defines the value  $\varepsilon_{\text{run}}$ . To better understand this relationship, consider a case with  $E_{\text{amb}} = 3 E_k$  depicted in

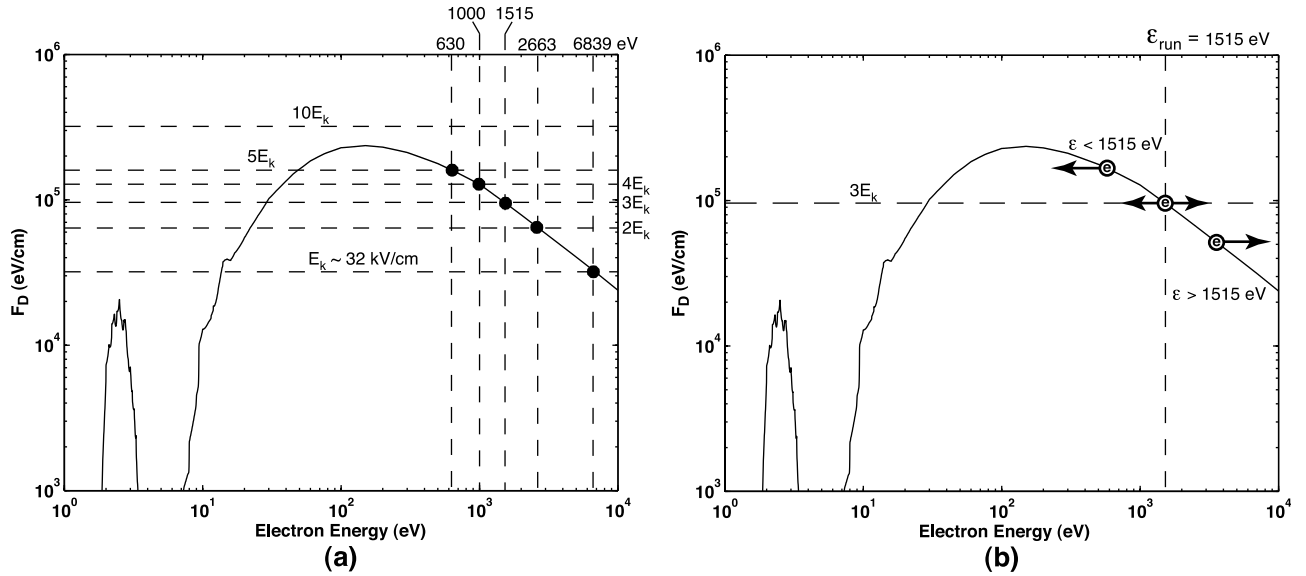


**Figure 27.** (a) The determination of the electron runaway energy  $\varepsilon_{\text{run}}$  using the dynamic friction force and the ambient electric field and (b) the three possible scenarios of an electron exiting the  $10E_k$  streamer tip corresponding to an ambient electric field  $E_{\text{amb}} = 3E_k$ .

Figure 27b. An electron emerging from the  $10E_k$  streamer tip region into the ambient field region may be considered to fall into one of three categories: the electron has an energy  $\varepsilon < \varepsilon_{\text{run}}$ ,  $\varepsilon \sim \varepsilon_{\text{run}}$ , or  $\varepsilon > \varepsilon_{\text{run}}$ . If the electron has not gained sufficient energy from the  $10E_k$  streamer tip ( $\varepsilon < \varepsilon_{\text{run}}$ ), the electron's motion will be dominated by collisions and the friction force will cause the electron to decelerate to low energies. If the electron has gained enough energy from the streamer tip such that  $\varepsilon > \varepsilon_{\text{run}}$ , the probability of the electron colliding with neutral particles has significantly decreased ( $F_D < 3E_k$ ) and the electron will continue to be accelerated to higher energies by the  $3E_k$  ambient field. If the electron has gained an energy  $\varepsilon \sim \varepsilon_{\text{run}}$ , the electron may be accelerated to higher energies by the ambient field or return to low energies depending on the collisions and angular scattering it experiences.

[81] Table 7 lists the values of  $\varepsilon_{\text{run}}$  for various ambient electric fields and the corresponding electron velocities. It should be noted that the maximum energy which an electron experiencing no collisions could gain from the 1 m long streamer tip (see Figure 26) with  $10E_k$  field at 70 km is 2170 eV. We emphasize again that this energy will be exactly the same for similar streamers at any pressure/altitude of interest. This energy corresponds to an ambient field of  $2.32E_k$ . Therefore it is impossible to achieve runaway electrons for ambient fields  $< 2.32E_k$  in the simulations. In reality, when collisions are considered, electrons only gain a fraction of the total 2170 eV and no runaway electrons were observed in any simulations with ambient electric fields  $2.5E_k$ . Simulations were therefore performed for ambient field values ranging from  $2.5E_k$  to  $5E_k$  as shown schematically in Figure 25b.

[82] We emphasize that changes in the width of the model streamer and the magnitude of the tip electric field would affect the numerical values of ambient fields at which runaway electrons can be sustained, and these

values can be easily evaluated using procedures outlined above.

[83] Figures 28 and 29 show simulation results for the runaway production rate  $\nu_{\text{run}}$  and the runaway flux out of the streamer tip  $\Gamma_{\text{run}}$  for various  $E_{\text{amb}}$  values ( $E_{\text{tip}} = 10E_k$  for all simulations). Figure 28a shows results obtained when high-energy angular scattering after all collisions was determined using equation (16), and Figure 28b shows the same case except high-energy scattering after excitation collisions was considered to be forward ( $\chi = 0$ ). Figures 29a and 29b show results for the same scenarios, respectively, utilizing equation (14) to determine high-energy scattering instead of equation (16). The solid lines in both Figures 28 and 29 were obtained using a spline interpolation between Monte Carlo data points.

[84] The variations in  $\nu_{\text{run}}$  and  $\Gamma_{\text{run}}$  at different ambient fields can be largely attributed to the runaway energy  $\varepsilon_{\text{run}}$  being variable with the ambient field (Table 7). For example, consider ambient fields of  $5E_k$  and  $3E_k$  corresponding to  $\varepsilon_{\text{run}} = 630$  eV and  $\varepsilon_{\text{run}} = 1515$  eV, respectively. A much larger fraction of the electron distribution exists at energies  $> 630$  eV than at energies  $> 1515$  eV, thus explaining the notable increase in  $\nu_{\text{run}}$  and  $\Gamma_{\text{run}}$  with the increase in

**Table 7.** Energy and Corresponding Velocity Required for an Electron to Run Away in Various Ambient Electric Fields

$E_{\text{amb}}/E_k$	$\varepsilon_{\text{run}}, \text{eV}$	$\nu_{\text{run}}, \text{m/s}$
1	6839	$4.90 \times 10^7$
1.5	3948	$3.73 \times 10^7$
2	2663	$3.06 \times 10^7$
2.32	2170	$2.76 \times 10^7$
2.5	1960	$2.63 \times 10^7$
3	1515	$2.31 \times 10^7$
3.5	1214	$2.07 \times 10^7$
4	1000	$1.88 \times 10^7$
4.5	788	$1.66 \times 10^7$
5	630	$1.49 \times 10^7$

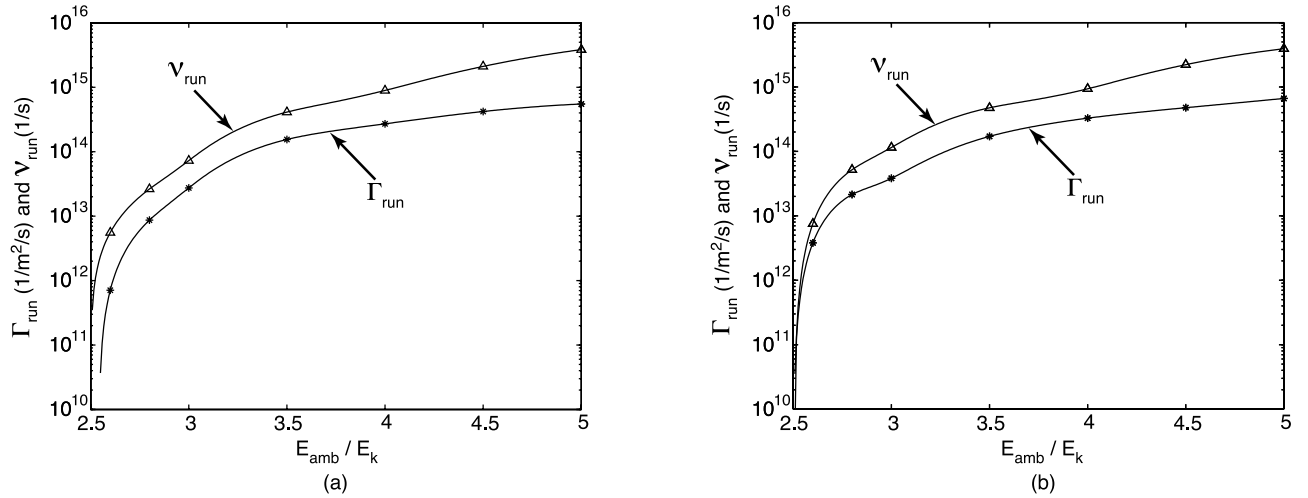


**Figure 28.** The runaway production rate  $\nu_{\text{run}}$  and the runaway flux  $\Gamma_{\text{run}}$  obtained from the Monte Carlo model when equation (16) is used to describe high-energy electron scattering (a) without and (b) with the assumption of forward scattering after excitation collisions.

ambient field. We emphasize again that the generation of runaway electrons is entirely due to the  $10 E_k$  streamer tip field. If  $\varepsilon_{\text{run}}$  were assigned a constant value for all ambient field cases,  $\nu_{\text{run}}$  would also remain constant for all ambient fields since the  $10 E_k$  streamer tip remains unchanged.

[85] It should be noted that not all electrons which achieve energies  $>\varepsilon_{\text{run}}$  can be considered true runaway electrons. The direction in which the electrons are traveling with respect to the electric field also plays a major role in runaway development. Electrons traveling in a direction opposing the applied electric field gain additional energy from the electric field, whereas electrons traveling in the same direction as the electric field lose energy. Therefore it is possible for electrons with energies  $>\varepsilon_{\text{run}}$  to have  $v_{\parallel}$  velocity components in the same direction as the electric field and subsequently be losing energy. Clearly, these

electrons do not fit the definition of runaway electrons since they are in fact losing energy to the electric field. This illustrates the reason why the angular scattering of electrons becomes so important in the development of runaway electrons. When electrons are subject to significant angular scattering, they are more prone to obtain a  $v_{\parallel}$  which is in the same direction as the applied electric field. Adversely, if electrons scatter primarily forward after collisions (in the direction of electron drift and opposing the direction of the electric field), it becomes easier for them to become runaway electrons because they will always be gaining energy from the applied electric field. In order to more accurately differentiate between true runaway electrons which are traveling in the direction opposite to the electric field and high-energy electrons which are traveling in the same direction as the electric field, a filtering procedure must be introduced into the simulations. Figure 30 shows

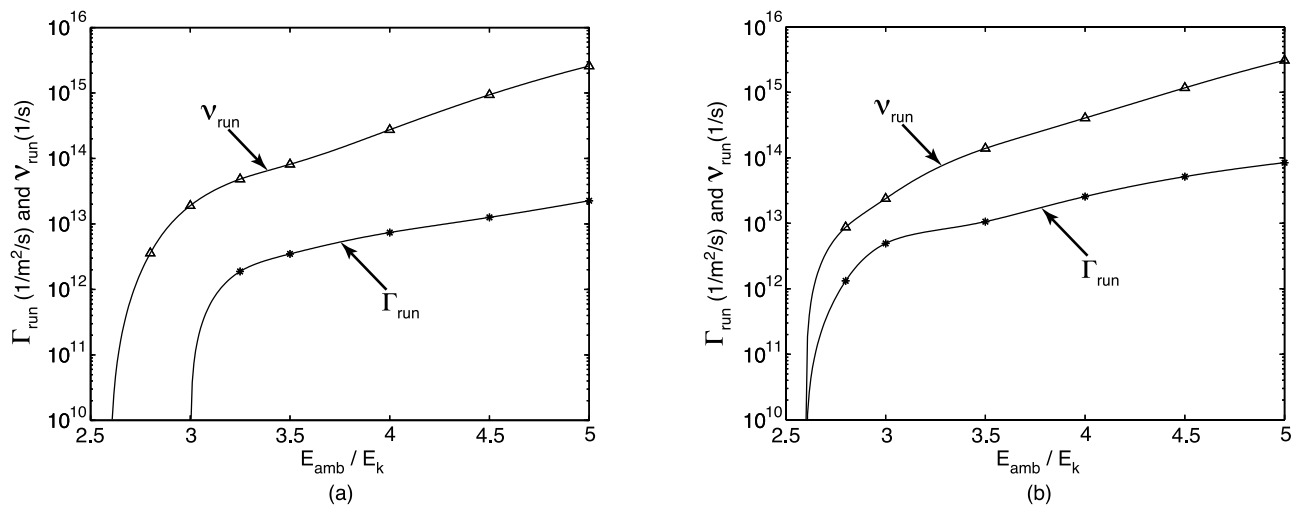
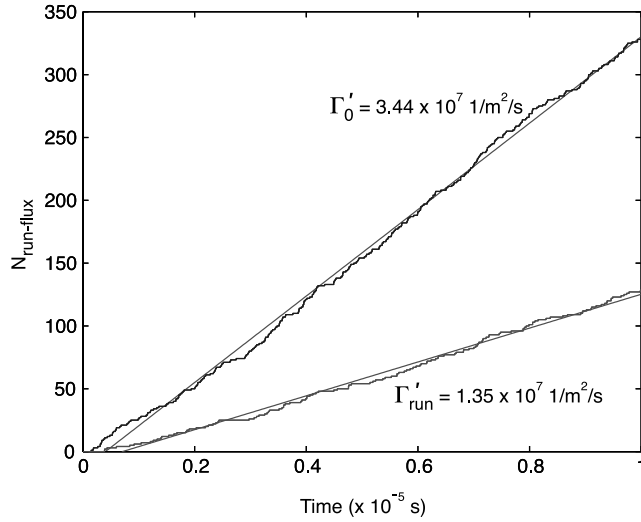


**Figure 29.** The runaway production rate  $\nu_{\text{run}}$  and the runaway flux  $\Gamma_{\text{run}}$  obtained from the Monte Carlo model when equation (14) is used to describe high-energy electron scattering (a) without and (b) with the assumption of forward scattering after excitation collisions.



For  $L = 1\text{m}$ ,  $V = 1\text{m}^3$ ,  $N_{\text{tip}} = 50000$ , and  $n_e = 10^{12}\text{m}^{-3}$  at  $70\text{ km}$ :

$$\Gamma_0 = \frac{n_e}{n_{\text{tip}}} \times \Gamma_0' = 6.88 \times 10^{14} \text{ 1/m}^2/\text{s}$$

$$\Gamma_{\text{run}} = \frac{n_e}{n_{\text{tip}}} \times \Gamma_{\text{run}}' = 2.70 \times 10^{14} \text{ 1/m}^2/\text{s}$$

**Figure 30.** The flux of electrons with energies  $>\varepsilon_{\text{run}}$  at the edge of the streamer tip  $\Gamma_0$  and the runaway flux of electrons  $1\text{ m}$  in front of the streamer tip  $\Gamma_{\text{run}}$  as calculated from a simulation with  $E_{\text{amb}} = 4E_k$ , angular scattering of electrons after all collisions determined by equation (16), and  $N_{\text{tip}} = 50,000$ .

the calculation of two fluxes of high-energy electrons obtained from a model simulation,  $\Gamma_0$  which is leaving the streamer tip at  $z = 1\text{ m}$  and  $\Gamma_{\text{run}}$  which was defined previously. The results shown in Figure 30 are for a case when  $E_{\text{amb}} = 4E_k$ , all angular scattering was determined using equation (16), and  $N_{\text{tip}} = 50,000$ . The difference between  $\Gamma_0$  and  $\Gamma_{\text{run}}$  arises due to the  $1\text{ m}$  ambient field region ahead of the streamer tip and the deceleration of a fraction of high-energy electrons within it. As discussed above, an electron exiting the streamer tip with an energy  $\varepsilon \sim \varepsilon_{\text{run}}$  may either continue to be accelerated to high energies by the ambient electric field or be returned to low energies due to collisions possessing strong backscatter components. Therefore the ambient field region acts as a filter separating the two groups of electrons. An electron which still possesses an energy greater than  $\varepsilon_{\text{run}}$  after traveling  $1\text{ m}$  in the ambient field region continues to gain more energy from the ambient field than it lost to collisions, consequently obeying the definition of a runaway electron as presented in section 1.2. It can be seen from Figure 30 that for this case only 39% of the electrons which achieved energies  $>\varepsilon_{\text{run}}$  at the streamer tip ( $z = 1\text{ m}$ ), still possessed energies  $>\varepsilon_{\text{run}}$  after traveling through the  $1\text{ m}$  ambient field region, the other 61% of electrons being decelerated by collisions in the ambient field region.

[86] Generally, the difference between  $\Gamma_0$  and  $\Gamma_{\text{run}}$  grows larger as the ambient field intensity increases ( $\varepsilon_{\text{run}}$  decreases). At low ambient fields (high  $\varepsilon_{\text{run}}$ ) electrons

which achieve energies  $>\varepsilon_{\text{run}}$  and contribute to  $\Gamma_0$  are at high enough energies such that they scatter predominantly forward after collisions. Therefore a large fraction of electrons achieving these high energies will continue to scatter forward in the ambient field region and accelerate to higher energies, thus contributing to  $\Gamma_{\text{run}}$ . Adversely, for high ambient fields (low  $\varepsilon_{\text{run}}$ ) electrons are counted as runaway within the streamer tip at much lower energies and do not possess the same forward scattering properties. Therefore a large number of these electrons will be subject to significant angular scattering upon entering the ambient field region and will decelerate to low energies bringing about a larger difference in  $\Gamma_0$  and  $\Gamma_{\text{run}}$ .

[87] Table 8 lists the average energies of electrons which were counted in the calculation of  $\Gamma_{\text{run}}$  and the maximum electron energy observed of those electrons. It becomes clear by comparing the values listed in Table 8 with the runaway energies  $\varepsilon_{\text{run}}$  listed in Table 7 that a portion of the electrons which were accelerated to energies  $>\varepsilon_{\text{run}}$  by the streamer tip continued to gain energy from the ambient electric field outside of the streamer tip, thus satisfying the definition of a true runaway electron. For most electric field cases, electron energies  $>2\text{ keV}$  were observed at the left boundary  $1\text{ m}$  ahead of the streamer tip. However, it should be noted that while many electrons counted in the calculation of  $\Gamma_{\text{run}}$  sustained energies significantly greater than  $\varepsilon_{\text{run}}$ , some electrons still possessed energies  $\sim\varepsilon_{\text{run}}$  and therefore may be decelerated to low energies by collisions at distances greater than  $1\text{ m}$  ahead of the streamer tip. The average values listed in Table 8 are dependent on the number of electrons included in the simulation. Since various electron densities were used for different ambient field and scattering cases (i.e., statistics are generally better for higher ambient fields), the accuracy of the values listed in the tables may vary with the ambient field.

[88] One of the most interesting aspects of Figures 28 and 29 is the existence of a cutoff electric field at which  $\nu_{\text{run}}$  and  $\Gamma_{\text{run}}$  rapidly drop to zero. In Figure 28a, in which equation (16) was used to determine all high-energy angular scattering, the cutoff fields are  $E_{\text{amb}} \approx 2.5E_k$  for  $\nu_{\text{run}}$  and  $E_{\text{amb}} \approx 2.55E_k$  for  $\Gamma_{\text{run}}$ . When excitation collisions are assumed to be forward for the same case, the cutoff electric field for both  $\nu_{\text{run}}$  and  $\Gamma_{\text{run}}$  is  $E_{\text{amb}} \approx 2.5E_k$  as can be seen in Figure 28b. This would suggest that the assumption of forward scattering after excitation collisions does not affect the cutoff electric field of the runaway production rate  $\nu_{\text{run}}$  but does impact the cutoff field of the runaway flux  $\Gamma_{\text{run}}$ . It can also be seen from Figures 28a and 29a that at high electric fields ( $>E_{\text{amb}} = 3E_k$ ), the forward scattering assumption has a minimal effect on the magnitude of  $\nu_{\text{run}}$  and  $\Gamma_{\text{run}}$ , possessing a maximum percent difference of  $\approx 14\%$  and  $\approx 19\%$ , respectively. However, for electric fields  $E_{\text{amb}} = 3E_k$ , the percent differences between Figures 28a and 29b are  $\approx 65\%$  for  $\nu_{\text{run}}$  and  $\approx 137\%$  for  $\Gamma_{\text{run}}$ , demonstrating that angular scattering after excitation collisions plays a larger role when lower ambient fields (higher  $\varepsilon_{\text{run}}$ ) are applied.

[89] Similarly, Figure 29a, in which equation (14) was used to determine all high-energy angular scattering, exhibits cutoff electric fields of  $E_{\text{amb}} \approx 2.6E_k$  and  $E_{\text{amb}} \approx 3E_k$  for  $\nu_{\text{run}}$  and  $\Gamma_{\text{run}}$ , respectively. When scattering after

**Table 8.** Average Runaway Electron Energy and Maximum Runaway Electron Energy Observed When Equation (16) and Equation (14) Were Used to Describe High-Energy Angular Scattering

$E_{\text{amb}}/E_k$	Equation (16) <sup>a</sup>		Equation (16) <sup>b</sup>		Equation (14) <sup>a</sup>		Equation (14) <sup>b</sup>	
	$\epsilon_{\text{avg}}$ , eV	$\epsilon_{\text{max}}$ , eV						
2.6	1987	1987	2025	2060	-	-	-	-
2.8	1841	2177	1839	2070	-	-	1744	1744
3	1680	2018	1585	1791	-	-	1665	1797
3.5	1550	2276	1503	2076	1531	1818	1516	1778
4	1388	2092	1466	2222	1480	2282	1350	1827
4.5	1421	2050	1416	2208	1379	1960	1379	2148
5	1462	2415	1460	2484	1393	2346	1383	2384

<sup>a</sup>High-energy angular scattering after all collisions.

<sup>b</sup>High-energy angular scattering after excitation collisions assumed to be forward.

excitation collisions is assumed to be forward, the cutoff field of  $\Gamma_{\text{run}}$  decreases from  $E_{\text{amb}} \approx 3E_k$  to  $E_{\text{amb}} \approx 2.6E_k$  while the cutoff field of  $\nu_{\text{run}}$  remains  $E_{\text{amb}} \approx 2.6E_k$ . Similar to Figure 28, the differences between the  $\nu_{\text{run}}$  values of Figures 29a and 29b are relatively small, with a maximum difference of  $\approx 83\%$ . On the contrary, the difference between the  $\Gamma_{\text{run}}$  values plotted in Figures 29a and 29b is dramatic, possessing percent differences  $>100\%$  at all electric field values. The fact that differences between Figures 29a and 29b are much greater than the differences between Figures 28a and 28b demonstrates that assuming forward scattering after excitation collisions has a much greater effect on runaway electrons when equation (14) is used to calculate high-energy angular scattering and corresponds well with the results reported in Figure 24.

[90] As discussed in section 2.2 and shown in Figure 24, the differential scattering cross section used to describe high-energy electron scattering can have a major impact on the development of runaway electrons. This can further be seen by comparing the results of Figures 28a to 29a and the results of Figures 28b to 29b. As discussed above, the most notable difference is the variation in the cutoff electric field at which  $\nu_{\text{run}}$  and  $\Gamma_{\text{run}}$  rapidly drop to zero. In addition to the variation in the cutoff electric field, the magnitudes of  $\nu_{\text{run}}$  and  $\Gamma_{\text{run}}$  are noticeably greater when the differential cross section of equation (16) is used. Comparing Figures 28a to 29a, at ambient electric fields  $\geq 3.5E_k$ , the values of  $\Gamma_{\text{run}}$  in Figure 28a are  $\approx 25$  to 45 times greater than those of Figure 29a. When scattering after excitation collisions is assumed to be forward, the  $\Gamma_{\text{run}}$  values of Figure 28b at ambient fields  $\geq 2.8E_k$  are  $\approx 8$  to 16 times those of Figure 29b. The differences in  $\nu_{\text{run}}$  are not as drastic, with a maximum percent difference between the values shown in Figure 28a and Figure 29a of  $\approx 150\%$  at  $E_{\text{amb}} = 2.8E_k$  decreasing to  $\approx 40\%$  at  $E_{\text{amb}} = 5E_k$ . Similarly, comparing Figures 28b to 29b results in percent differences of  $\approx 140\%$  at  $E_{\text{amb}} = 2.8E_k$  decreasing to  $\approx 25\%$  at  $E_{\text{amb}} = 5E_k$ . Since the differences in  $\nu_{\text{run}}$  are not as great as those in  $\Gamma_{\text{run}}$ , one may conclude that the angular scattering of electrons once they enter the ambient field region ahead of the streamer tip is much more critical for sustaining runaway electrons than the scattering of electrons within the high field streamer tip.

[91] The difference in  $\nu_{\text{run}}$  between the two cross section cases (equations (14) and (16)) decreases at higher electric field due to the fact that as  $E_{\text{amb}}$  increases,  $\epsilon_{\text{run}}$  decreases. For example, when  $E_{\text{amb}} = 5E_k$ ,  $\epsilon_{\text{run}} = 630$  eV, so recalling

from sections 2.1 and 2.2 that electron scattering from collisions with  $N_2$  at energies  $\epsilon < 500$  eV and from collisions with  $O_2$  and  $Ar$  at energies  $\epsilon < 1000$  eV are treated using experimental cross section data for all simulations, the scattering of electrons which achieve energies  $>\epsilon_{\text{run}}$  has only been determined using equations (14) and (16) over the small energy range of 500 to 630 eV. On the contrary, when  $E_{\text{amb}} = 3E_k$  ( $\epsilon_{\text{run}} = 1515$  eV), scattering of electrons reaching energies  $>\epsilon_{\text{run}}$  have been treated using equations (14) and (16) over much larger energy ranges of 500 to 1515 eV for collisions with  $N_2$  and 1000 to 1515 eV for collisions with  $O_2$  and  $Ar$ , therefore the effect of high-energy scattering approximations is much greater for lower electric fields (higher  $\epsilon_{\text{run}}$ ).

[92] Figure 31 shows the electron energy distribution function, drift velocity, and mean energy as well as an electron position versus electron energy phase space plot for six different regions in the one-dimensional simulation. The ambient electric field was chosen to be  $E_{\text{amb}} = 4E_k$  and equation (16) was used to calculate high-energy electron scattering. It can be seen in Figure 31 that the electron population within the streamer tip maintains a drift velocity  $\sim 10^6$  m/s and a mean energy  $\sim 30$  eV. Just ahead of the streamer tip, the drift velocity and mean energy were found to be  $\approx 5.24 \times 10^5$  m/s and  $\approx 17.0$  eV, respectively, demonstrating a 62% and 57% decrease from just inside the streamer tip. These values continue to decrease to values of  $\approx 3.94 \times 10^5$  m/s and  $\approx 10.6$  eV at a distance  $\approx 1$  m ahead of the streamer tip. From the electron position versus energy phase space plots, it can be seen that while the bulk of the electron population remains at low energies, a small number of electrons are accelerated to runaway energies by the streamer tip and continue to runaway as they travel through the ambient field region. It can also be seen from the phase space plots that a number of electrons exiting the streamer tip with high energies eventually decelerate as they move further away from the streamer tip.

#### 4.2. Self-Acceleration of Electrons

[93] Simulation results in section 4.1 have been presented for a case when the streamer tip was assumed to be stationary for computational simplicity. In reality, streamers can propagate at velocities on the order of one tenth of the speed of light. *Stanley et al.* [1999], *Moudry et al.* [2002, 2003], and *McHarg et al.* [2002] have reported streamer speeds in sprites of  $\sim 1.2 \times 10^7$ ,  $\sim 3 \times 10^7$ , and  $\sim 5.3 \times 10^7$  m/s, respectively. The electron energies

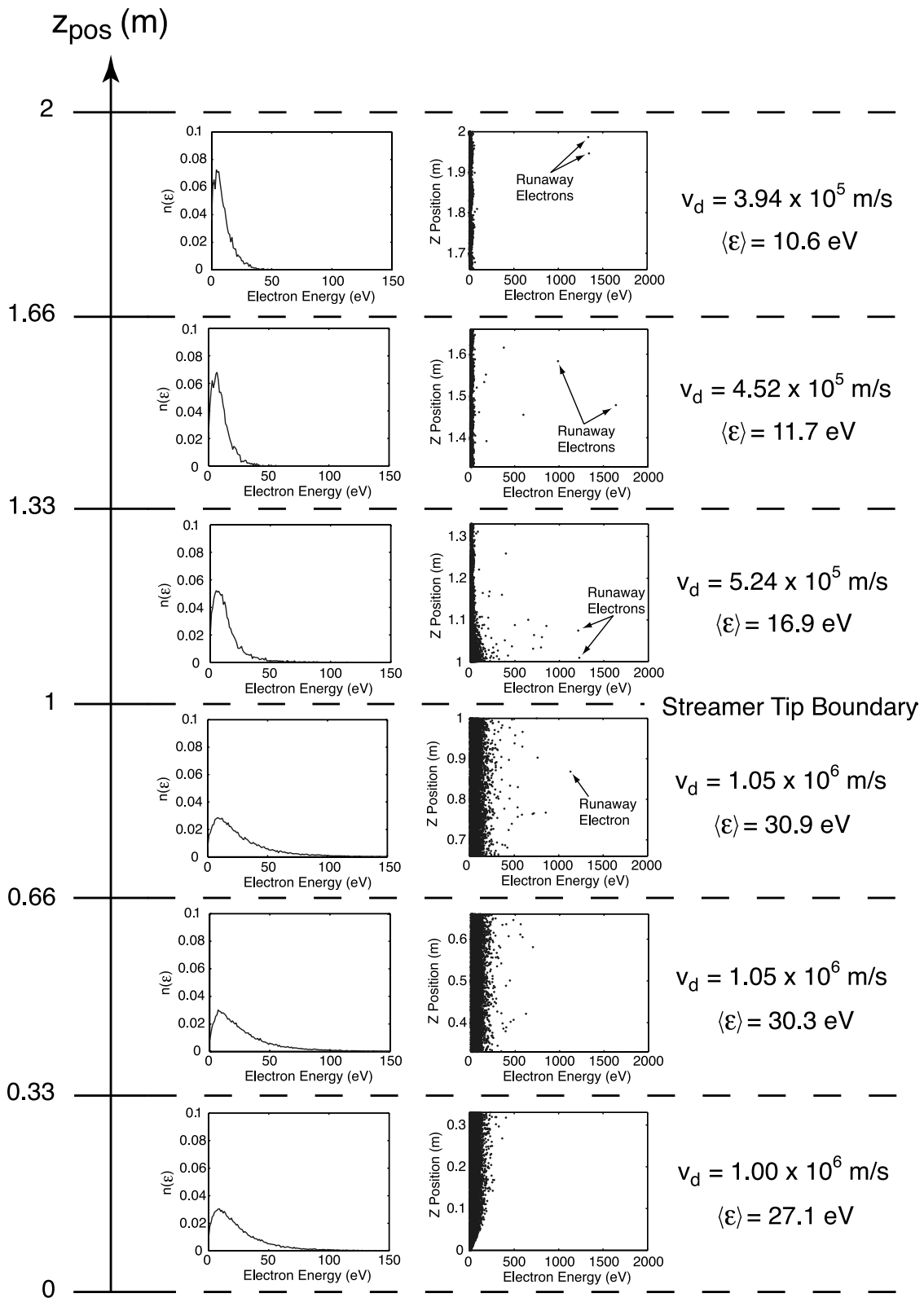


**Figure 31.** The energy distribution function  $n(\epsilon)$ , electron position versus energy phase space, drift velocity  $v_d$ , and electron mean energy  $\langle \epsilon \rangle$  as functions of distance in a one-dimensional simulation with  $E_{\text{amb}} = 3E_k$ .

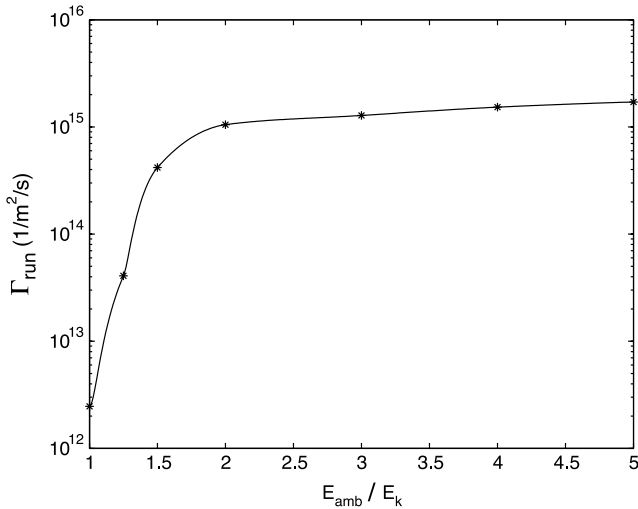


**Figure 32.** The runaway flux  $\Gamma_{\text{run}}$  obtained from the Monte Carlo model when equation (16) is used to describe high-energy electron scattering and assuming a streamer speed of  $v_{\text{str}} = 1.2 \times 10^7$  m/s.

corresponding to these speeds are 409 eV, 2559 eV, and 7985 eV (see Table 7). Therefore for an electron to exit the streamer tip ahead of the propagating streamer it must achieve a velocity greater than that of the streamer's propagation. In view of the simulation setup presented in section 4.1, since the maximum energy an electron can gain in the 1 m streamer tip region is 2170 eV, it would seem to be impossible for an electron to accelerate ahead of streamers propagating at the latter two speeds. However, a situation may arise during the propagation of a negative streamer in which a fraction of the total electron population travels with the propagating streamer tip. This is known as self-acceleration of electrons and was first proposed by *Babich* [1982]. If this were to occur, electrons would be exposed to the high streamer tip field for an extended amount of time and may gain enough additional energy from the high electric field to accelerate ahead of the streamer tip and may make it possible for runaway electrons to be observed for ambient electric fields  $< 2.5E_k$ .

[94] In order to study the effects of self-acceleration of electrons, in this section the simulation setup presented in section 4.1 is modified to account for the motion of the streamer tip. Using the same electric field configuration as discussed in section 4.1 (see Figure 25b), the relative velocity of the streamer tip may be added to the simulation by introducing an extra term to equation (60) as

$$z' = z + v_{\parallel} \cdot \Delta t - v_{\text{str}} \cdot \Delta t, \quad (63)$$

where  $v_{\text{str}}$  is the velocity of the streamer. Therefore in each time step the electrons will travel a distance  $v_{\parallel} \cdot \Delta t$  according to their parallel velocity component but will also be moved a distance  $v_{\text{str}} \cdot \Delta t$  back in the simulation space to reflect the movement of the streamer. Essentially, the electrons are moving at their own speed, and the simulation domain is moving at the speed of the streamer  $v_{\text{str}}$ .

[95] The electron density is initially constant over the entire 2 m span and remains so throughout the simulation without any remapping or repositioning of the electrons being necessary. When runaway electrons are lost from the simulation through the  $1 \text{ m}^2$  area ahead the streamer tip, low-energy electrons are randomly positioned back into the simulation to replace them. When low-energy electrons pass through the  $z = 0$  m left side of the simulation domain (see Figure 25b), they are repositioned at  $z = 2$  m and their energies are reset to the mean energy of electrons corresponding to the  $E_{\text{amb}}$  electric field. Similarly, electrons passing through the  $z = 2$  m boundary are repositioned at  $z = 0$  m and their energies are reset to the mean energy of electrons corresponding to the  $E_{\text{tip}}$  electric field. The simulation may simply be viewed as a 1 m long electric field pulse traveling at a speed  $v_{\text{str}}$  through a constant density of electrons which are traveling at a drift velocity  $v_d$  determined by the applied ambient field  $E_{\text{amb}}$ . Since  $v_d$  is generally much less than  $v_{\text{str}}$ , the bulk of the electron population will simply be passed over by the streamer tip and repositioned at  $z = 2$  m as described above. However, depending on the streamer speed  $v_{\text{str}}$ , it is possible for a small fraction of the total electron population to actually achieve an energy necessary to travel with the streamer tip and experience the self-acceleration phenomenon. As with the stationary streamer tip model, secondary electrons emerging from ionizing collisions were not added to the simulation. If secondary electrons were included, similar increases of  $\Gamma_{\text{run}}$  could be expected as discussed in the previous section.

[96] Simulations were first performed for streamer tip fields of  $10E_k$  and streamer speeds of  $v_{\text{str}} = 3 \times 10^7$  and  $v_{\text{str}} = 5.3 \times 10^7$  m/s. For these streamer speeds no runaway electrons were observed as the streamer propagated too fast to allow adequate time for electrons to gain sufficient energy from the  $10E_k$  electric field and travel with the streamer tip. The electric field pulse essentially flew right by the background electron density. However, when the streamer speed was set to  $v_{\text{str}} = 1.2 \times 10^7$  m/s, the results were drastically different.

[97] Figure 32 shows the runaway flux  $\Gamma_{\text{run}}$  for various ambient electric fields (for all simulations  $E_{\text{tip}} = 10 E_k$  and equation (16) was used to calculate angular scattering of high-energy electrons after all collisions). As can be seen from Figure 32, the ambient fields at which  $10 E_k$  streamer tips can produce thermal runaway electrons extend all the way down to the conventional breakdown field  $E_k$ . Considering the major differences between the values of  $\Gamma_{\text{run}}$  shown in Figure 28a and Figure 32, it can easily be concluded that the self-acceleration of electrons can play a major role in the production of thermal runaway electrons by streamer tips. In addition to the increased fluxes of thermal runaway electrons, the energies achieved by the runaway electrons also increased significantly as can be seen in Table 9. Once again it should be noted that the variation in flux for various ambient fields arises due to the runaway energy  $\epsilon_{\text{run}}$  being defined by the ambient field as discussed in section 4.1. The average runaway electron energies increase for electric fields  $< 2E_k$  due to  $\epsilon_{\text{run}}$  increasing (see Table 7), therefore eliminating lower energy runaway electrons from the averaging which would have been included for

**Table 9.** Average Runaway Electron Energy and Maximum Runaway Electron Energy Observed When Equation (16) Was Used to Describe High-Energy Angular Scattering After All Collisions and Assuming a Streamer Speed of  $v_{\text{str}} = 1.2 \times 10^7$  m/s

$E_{\text{amb}}/E_k$	$\epsilon_{\text{avg}}$ , eV	$\epsilon_{\text{max}}$ , eV
1	7574	8224
1.25	5632	7193
1.5	4447	5656
2	3794	5421
3	3882	6560
4	4111	7201
5	4478	8191

higher ambient fields (lower  $\epsilon_{\text{run}}$ ). The increase in  $\epsilon_{\text{max}}$  for electric fields  $< 2E_k$  can be attributed to increased electron densities used in the simulations which in turn increase the chance that one electron out of the assembly may be accelerated to very high energies.

[98] In addition to the simulations shown in Figure 32, simulations were also performed for a streamer tip field of  $E_{\text{tip}} = 8E_k$  and streamer speed of  $v_{\text{str}} = 1.2 \times 10^7$  m/s. Using the same procedures as outlined above and equation (16) to describe high-energy electron scattering, runaway fluxes of  $\Gamma_{\text{run}} = 6.12 \times 10^{12}$  1/m<sup>2</sup>/s and  $\Gamma_{\text{run}} = 1.17 \times 10^{13}$  1/m<sup>2</sup>/s were obtained for ambient fields of  $E_{\text{amb}} = 2E_k$  and  $E_{\text{amb}} = 3E_k$ , respectively. The average and maximum energies were found to be  $\epsilon_{\text{avg}} = 3707$  eV and  $\epsilon_{\text{max}} = 4681$  eV for  $E_{\text{amb}} = 2E_k$  and  $\epsilon_{\text{avg}} = 3909$  eV and  $\epsilon_{\text{max}} = 4228$  eV for  $E_{\text{amb}} = 3E_k$ . For this  $E_{\text{tip}} = 8E_k$  case, simulations with ambient electric fields  $< 2E_k$  produced no runaway electrons.

[99] The results presented above suggest that there exists a range of streamer propagation speeds and electric field configurations capable of producing a significant number of thermal runaway electrons. Performing simple analytical calculations (with electron-neutral collisions neglected), it can be found that for a 1 m in width streamer tip of  $10E_k$  there exist a cutoff streamer speed  $v_{\text{str}}$  at which electrons cannot experience self-accelerating effects. It can be shown for this streamer configuration that at streamer speeds  $v_{\text{str}} > 2.75 \times 10^7$  m/s no runaway electrons will flux through the tip of streamer since this speed does not allow adequate time for low-energy electrons to gain an energy substantial enough to travel with the propagating streamer. Conversely, self-accelerating effects can be observed for a wide range of lower streamer propagation speeds; however, the maximum energy an electron can gain under the most favorable conditions never exceeds  $\sim 9$  keV. For  $v_{\text{str}} = 1.2 \times 10^7$  m/s (corresponding to the results discussed above), it can be found that the maximum possible energy of an electron leaving the streamer tip after experiencing self-acceleration is  $\sim 4.5$  keV. This value corresponds well with most of the average runaway energy  $\epsilon_{\text{avg}}$  values listed in Table 9. It should be noted that the value of 4.5 keV estimated above from an analytical formulation is calculated for electrons exiting the streamer tip at  $z = 1$  m and does not account for electrons' perpendicular velocity components  $v_{\perp}$ . Electrons which were observed in simulations with energies  $\sim 8$  keV obtained perpendicular velocities  $v_{\perp} > v_{\parallel}$ . These electrons most likely moved in and out of the streamer tip

region several times before finally exiting through the  $z = 2$  m boundary, allowing them to gain additional energy.

### 4.3. Fluxes of Thermal Runaway Electrons in Lightning Leaders

[100] The results for  $v_{\text{run}}$  and  $\Gamma_{\text{run}}$  presented in sections 4.1 and 4.2 are for altitudes of 70 km corresponding to sprites. However, these values may also be scaled using the similarity properties of streamers [e.g., *Liu and Pasko*, 2004, and references therein] to other altitudes of interest such as ground level [*Dwyer et al.*, 2005] and 16 km [*Dwyer*, 2005b], which may correspond to the leader streamer zone of lightning. Assuming the neutral atmospheric densities  $N$  and streamer densities  $n_e$  listed in Table 10 for altitudes of 0, 16, and 70 km, the values of  $v_{\text{run}}$  and  $\Gamma_{\text{run}}$  reported in Figures 28, 29, and 30 may be scaled to 0 and 16 km simply by multiplying the values by scaling factors  $\frac{n_{e0}}{n_{e70}}$  and  $\frac{n_{e16}}{n_{e70}}$ , respectively.

[101] As discussed in section 1.1, a leader fuses the currents of numerous streamers that start from the tip, into a single channel [*Raizer*, 1991, p. 367]. Now, consider a leader with a typical current  $\sim 100$  A [*Raizer*, 1991, p. 372] propagating at an altitude of 16 km. The current of a typical streamer may be approximated by

$$I_s = q_e n_e v_d \pi r_s^2, \quad (64)$$

where  $v_d$  is the drift velocity of electrons ( $v_d = \mu_e |E|$ ) and  $r_s$  is the radius of the streamer. For a streamer radius  $r_s = 2.3 \times 10^{-3}$  m and the streamer channel field  $\sim E_k$ , the typical streamer current would be  $I_s \approx 1.8$  A. Dividing the leader current of 100 A by the individual streamer current of 1.8 A would result in an estimation of 55 streamers ahead of the leader tip. We note that 55 is a very conservative estimate. It is known that up to  $10^5$  streamers can exist at any moment of time in the leader streamer zone during the quasi-stationary stages of leader propagation [*Bazelyan and Raizer*, 2000, p. 70]. The assumed number (55) should adequately represent the total number of streamers attached to the leader head during a transient ( $\sim 1$   $\mu$ s) negative corona flash stage of the negative leader development discussed in section 5.

[102] Scaling the value of  $\Gamma_{\text{run}}$  from Figure 32 at  $E_{\text{amb}} = 1.5E_k$  to 16 km results in  $\Gamma_{\text{run}} = 1.44 \times 10^{21}$  1/m<sup>2</sup>/s and multiplying by 55 streamers gives a total runaway flux of  $\approx 7.92 \times 10^{22}$  1/m<sup>2</sup>/s associated with the leader streamer zone at 16 km. Considering that the cross-sectional area of a streamer with radius  $r_s = 2.3 \times 10^{-3}$  m is  $1.66 \times 10^{-5}$  m<sup>2</sup> and multiplying the cross-sectional area of one streamer by 55 total streamers results in a total area of  $9.14 \times 10^{-4}$  m<sup>2</sup>. The runaway flux  $\Gamma_{\text{run}} = 1.44 \times 10^{21}$  1/m<sup>2</sup>/s may then be multiplied by the total cross-sectional area  $9.14 \times 10^{-4}$  m<sup>2</sup> of the 55 streamers resulting in a total of  $\approx 10^{18}$  runaway electrons emitted by the leader head per

**Table 10.** Neutral Atmospheric Density  $N$  and Streamer Density  $n_e$  at Altitudes of 0, 16, and 70 km

Altitude, km	$N$ , m <sup>3</sup>	$n_e$ , m <sup>3</sup>
0	$2.688 \times 10^{25}$	$2.2 \times 10^{20}$
16	$3.462 \times 10^{24}$	$3.6 \times 10^{18}$
70	$1.823 \times 10^{21}$	$1.0 \times 10^{12}$

second. Noting that the streamer electron number density and the flux  $\Gamma_{\text{run}}$  scale with the atmospheric neutral density as  $\sim N^2$  and the streamer cross-sectional area scales as  $\sim 1/N^2$  (since  $r_s \sim 1/N$ ), the estimate of the total number of runaway electrons produced by the leader tip per second presented above (i.e.,  $10^{18} \text{ s}^{-1}$ ) is valid for a 100 A leader at any other air pressure/altitude of interest.

[103] We emphasize that the calculations above are based on runaway fluxes calculated at a fixed distance ahead of the streamer tips, and at other distances the number of runaway electrons may vary greatly from the values reported in this paper depending on particular details of geometry and time dynamics of the driving electric field. These estimates nevertheless demonstrate that a significant number of thermal runaway electrons may be generated by the leader streamer zone of lightning, which could contribute to the generation of recently reported X-ray and gamma ray bursts observed in association with lightning discharges [Moore *et al.*, 2001; Dwyer *et al.*, 2003, 2004a, 2004b, 2005; Smith *et al.*, 2005].

[104] Concerning the theory of runaway breakdown, the future dynamics of these electrons at greater distances from the streamer tip must be considered. Depending on the geometry and time dynamics of the electric field ahead of the streamer tip, runaway electrons with energies  $\sim 2 \text{ keV}$  generated by the streamer tip may either decelerate to low energies or continue to gain energy  $\sim \text{MeV}$ . These MeV electrons may then contribute to relativistic runaway avalanches, as described by Gurevich *et al.* [1992], Roussel-Dupre *et al.* [1994], Lehtinen *et al.* [1999], Gurevich and Zybin [2001], Dwyer [2003], and references cited therein (see discussion in section 5). A more complex model should be introduced to link thermal runaway electrons generated by streamer tips to the relativistic runaway electron avalanche model proposed by Gurevich *et al.* [1992] and determine the fraction of thermal runaway electrons which obtain energies  $\sim \text{MeV}$  for various electric field configurations.

## 5. Acceleration of Electrons to MeV Energies in Streamer Zones of Lightning Leaders

[105] In this section we discuss a probable scenario of events in which nonrelativistic thermal runaway electrons discussed in the preceding sections can be accelerated to energies of hundreds of keV and even possibly to tens of MeV, leading to the generation of observed hard X-rays [e.g., Dwyer *et al.*, 2005; Smith *et al.*, 2005] through the bremsstrahlung process.

[106] Potential differences due to charge separation in thunderclouds are on the order of  $U = 10\text{--}100 \text{ MV}$ . These charges are normally separated by distances of several kilometers so that average fields typically observed in thunderclouds are on the order of  $0.3 \text{ kV/cm}$  [e.g., Raizer, 1991, p. 370; Marshall *et al.*, 1996, 2001]. Our discussion in this section refers to characteristic field values at ground pressure, and corresponding values at higher altitudes can be obtained by scaling these fields proportionally to the atmospheric neutral density, as was discussed previously. Fields  $\sim 0.3 \text{ kV/cm}$  are not sufficient for the development of runaway electron phenomena since they are lower than both the relativistic  $E_t \simeq 2 \text{ kV/cm}$  and thermal  $E_c \simeq$

$260 \text{ kV/cm}$  runaway thresholds (see Figure 2). However, lightning leaders are known to be able to propagate in such low fields. The leader process itself is quite complex, and its initiation mechanism and internal physics are not yet fully understood [e.g., Uman, 2001, p. 79; Raizer, 1991, p. 370; Bazelyan and Raizer, 1998, p. 203, 253]. The head of the highly ionized and conducting leader channel is normally preceded by a streamer zone looking as a diverging column of diffuse glow which is filled with highly branched streamers [e.g., Bazelyan and Raizer, 1998, p. 203, 253]. Owing to its high conductivity, the leader channel can be considered as equipotential and therefore plays the primary role in the focusing/enhancement of the electric field in the streamer zone where relatively weakly conducting streamer coronas propagate [e.g., Raizer, 1991, p. 364]. Leaders of positive polarity attract electron avalanches, while in those of negative polarity the avalanching electrons move in the same direction as the leader head. In large experimental gaps ( $>100 \text{ m}$ ) and in thunderclouds, the electric fields required for propagation of positive and negative polarity leaders are known to be nearly identical; however, the internal structure of their streamer zones, which is closely associated with the direction of electron avalanches, is very different [Raizer, 1991, p. 375; Bazelyan and Raizer, 1998, p. 253].

[107] Owing to its equipotential properties, the leader head can carry a large portion of the cloud potential  $U = 10\text{--}100 \text{ MV}$  toward the ground. Approximately half of this potential drops in the leader streamer zone [Bazelyan and Raizer, 2000, p. 253]. The electric fields in streamer zones of positive and negative leaders remain constant at  $E_{cr}^+ \simeq 4.4 \text{ kV/cm}$  and  $E_{cr}^- \simeq 12.5 \text{ kV/cm}$ , respectively (see Figure 2). The size of the streamer zone can therefore be simply evaluated as  $R_s \simeq U/2E_{cr}^\pm$  for leaders of different polarities. We note that the value  $E_{cr}^- \simeq 12.5 \text{ kV/cm}$  is not very well established, and different sources list various values ranging from  $7.5 \text{ kV/cm}$  [Gallimberti *et al.*, 2002] to  $10 \text{ kV/cm}$  [Bazelyan and Raizer, 2000, p. 198]. Assuming for numerical estimates that  $U = 20 \text{ MV}$ , the streamer zone size of a negative leader can be evaluated as  $R_s \simeq 10 \text{ m}$ .

[108] Returning to the discussion of runaway phenomena, we note that the fields  $E_{cr}^+$  and  $E_{cr}^-$  in the leader streamer zone are not by themselves sufficient to support thermal runaway phenomenon. Conversely, these fields do appear to be higher than the relativistic runaway threshold field  $E_t \simeq 2 \text{ kV/cm}$  and should be able to support avalanches of relativistic runaway electrons. However, if the avalanche distance of relativistic runaway electrons is considered to be  $l_a \sim 50 \text{ m}$  [e.g., Gurevich and Zybin, 2001], which is greater than the size of the leader streamer zone  $R_s \simeq 10 \text{ m}$ , the multiplication of relativistic (i.e., 1 MeV cosmic ray secondary) electrons can be completely neglected.

[109] The streamers in both positive and negative leaders originate from the surface of the leader head. It is believed that at the surface of a leader head the electric field can reach values comparable to the conventional breakdown threshold field (i.e.,  $\sim 1.5E_k$  [Bazelyan and Raizer, 2000, p. 68]). The frequency with which a leader head emits streamers is estimated to be  $\sim 10^9 \text{ s}^{-1}$ , and about  $10^5$  streamers are present in a leader streamer zone at any given time [Bazelyan and Raizer, 2000, p. 70]. Again, the

field  $1.5E_k$  is not sufficient to directly support the thermal runaway phenomena. Relativistic runaway effects can also be completely ignored due to the very small size  $<1$  cm of the region where the  $1.5E_k$  field is present. Since electrons in positive leaders move in the direction opposite to the streamer propagation, and due to the fact that electric fields in the streamer zone of positive leaders are very low ( $E_{cr}^+ \simeq 4.4$  kV/cm), positive leaders will not be considered as potential producers of thermal runaway electrons of considerable energy.

[110] Considering the negative leader case, we note that the  $1.5E_k$  field is fully sufficient for the fast development, acceleration, expansion, and branching of streamers, as well as the production of  $\sim 2$  keV (and up to  $\sim 8$  keV, when self-acceleration conditions are satisfied, see section 4.3) thermal runaway electrons in streamer tips. These energies, however, are not sufficient for the continuation of electron runaway after electrons exit the streamer tips and appear in streamer zone fields  $\sim 10$  kV/cm. Energies in excess of 30–100 keV (see Figure 2) are needed for continuation of runaway acceleration in this case. From these arguments it becomes clear that although the 10 MV voltage difference is readily available in the streamer zone, thermal runaway electrons are unlikely to be accelerated to MeV energies during the quasi-stationary stages of leader development.

[111] Although details are still not fully understood, laboratory experiments and observations of natural lightning indicate a stepwise development of negative leaders. *Gallimberti et al.* [2002] and *Bazelyan and Raizer* [2000, p. 197] represent two of the best sources, covering the stepping process in sufficient detail and allowing one to appreciate the many complex features of the phenomenon. One of the key components of the stepping process is the formation of a “space leader,” which originates near the external boundary of the negative streamer zone. The space leader propagates as a bidirectional discharge, whose positive end propagates toward the negative leader head. The junction of the space leader with the negative leader head closely resembles a return stroke accompanied by a strong illumination of the entire leader channel. The tip of the main leader “jumps” over to a new space, which was previously occupied by the space leader, and delivers to it the high potential of the previous leader head. The sudden rise of the space leader potential causes the inception of a negative corona flash. *Bazelyan and Raizer* [2000, p. 199] describe this phenomenon as follows: “The tremendous potential difference that arises in the vicinity of the newly formed tip at this moment produces a flash of a powerful negative streamer corona, which transforms to the novel streamer zone of the main leader.” The length of the new streamer zone is determined by exactly the same relationship  $R_s \simeq U/2E_{cr}^-$  as was discussed above.

[112] The new leader tip establishes a high potential at a speed comparable to the speed of light  $c$ , similar to lightning return strokes [*Bazelyan and Raizer*, 2000, p. 116]. The establishment of the new streamer zone, however, does not proceed instantaneously. Even highly overvolted streamers propagating in ambient fields well above the conventional breakdown threshold  $E_k$  are expected to maintain their speed much less than the speed of light due to self-regulating induction effects [*Dyakonov and Kachorovskii*, 1989; *Liu and Pasko*, 2004]. Assuming

very high streamer speeds  $v_{str}$  on the order of  $10^7$  m/s, it is expected that the new streamer zone, with previously evaluated radius  $R_s \simeq 10$  m, would be established on a timescale of  $\tau_{TGF} \sim R_s/v_{str} \sim 1$   $\mu$ s. During this time delay it is expected that electric fields  $>E_k$  would be present well beyond the immediate  $<1$  cm vicinity of the new leader tip, therefore allowing thermal runaway electrons generated in streamer tips constituting the negative corona flash to continue gaining energy in the ambient electric field (as quantitatively demonstrated in sections 4.1 and 4.2 of this paper). Electrons which gain energy above 30–100 keV (see Figure 2) should be able to continue gaining energy in the leader streamer zone up to several MeV energies, depending on the particular magnitude of the leader tip potential. These electrons should also be able to exit the leader streamer zone and avalanche in accordance with the [*Gurevich et al.*, 1992] relativistic runaway theory if significant fields  $>E_t$  are available on large scales ( $\gg l_a \sim 50$  m) in thunderclouds. However, the avalanche multiplication of relativistic electrons can be ignored inside the leader streamer zone due to its very compact size ( $\sim 10$  m). Therefore the large number of relativistic electrons inside the leader streamer zone are expected solely due to the large fluxes of thermal runaway electrons estimated in section 4.3.

[113] *Dwyer et al.* [2005] has reported hard X-ray emissions with energies up to several hundreds of keV. The  $<1$   $\mu$ s emissions occurred in one-to-one correlation with negative leader steps. Assuming a relatively high leader propagation velocity of  $2 \times 10^6$  m/s during its approach to ground stage and the observed 10 steps during a 200  $\mu$ s time interval [*Dwyer et al.*, 2005], we can estimate a leader step length  $\sim 20$  m, which is consistent with a typical leader step length of 3–50 m [*Raizer*, 1991, p. 374]. The duration of the bursts and the step length appear to be consistent with the negative corona flash hypothesis discussed above.

[114] In a general case, the duration  $\tau_{TGF}$  of a negative corona flash and its associated energetic radiation is defined primarily by the pressure independent speed of overvolted streamers  $v_{str} \sim 10^7$  m/s and the size of the leader streamer zone  $R_s$  as  $\tau_{TGF} \sim R_s/v_{str}$ . Assuming typical ground values of  $R_s \sim 3$ –200 m [*Raizer*, 1991, p. 374],  $\tau_{TGF}$  can be found to be  $\sim 0.3$ –20  $\mu$ s and may be extended to a millisecond time scale for streamer zones extending to several kilometers above cloud tops as with blue jet and gigantic jet phenomena [e.g., *Pasko et al.*, 2002].

## 6. Conclusions

[115] The principal results and contributions of this paper can be summarized as follows:

[116] 1. A zero-dimensional Monte Carlo model which is capable of describing electron dynamics in air (including thermal runaway phenomena) under the influence of an external electric field of arbitrary strength has been developed. The model has been validated at high electric fields ( $E > E_k$ ) by comparisons with studies conducted for  $N_2$  by *Kunhardt and Tzeng* [1986a], *Tzeng and Kunhardt* [1986], and more recently by *Bakhov et al.* [2000], and at low electric fields ( $E < E_k$ ) by comparisons with available data from swarm experiments in air [*Davies*, 1983],

solutions of the Boltzmann equation based on the two-term spherical harmonic expansion of the electron distribution function [Morgan and Penetrante, 1990], and analytical models proposed by Aleksandrov et al. [1995] and Morrow and Lowke [1997]. The model is capable of calculating the electron energy distribution function, electron mean energy, and electron drift velocity, as well as attachment, excitation, and ionization rate coefficients at various air pressures and electric field strengths.

[117] 2. A one-dimensional Monte Carlo model for studies of the acceleration of low-energy electrons to runaway energies in highly overvolted streamer tips has been developed. The extremely high electric field associated with a negative streamer tip immediately preceding branching at an altitude of 70 km was approximated by a 1 m square pulse with field magnitude equal to  $10 E_k$ . The runaway production rate  $v_{\text{run}}$  within the streamer tip and the runaway flux through a unit area 1 m ahead of the streamer tip  $\Gamma_{\text{run}}$  were documented for the various ambient field values and four different cases of high-energy electron scattering. Additionally, several case studies were then performed to examine the theory of self-acceleration of electrons in streamer tips. The documented results suggest that streamers, which naturally occur in transient luminous events and streamer zones of conventional lightning leaders, could provide a robust source of thermal runaway electrons. These electrons could provide an alternate source of relativistic seed electrons previously thought to require galactic cosmic rays and may be related to the recent observations of X-ray and gamma ray bursts associated with thunderstorm activity.

[118] 3. The importance of high-energy angular scattering of electrons in the development of thermal runaway electrons has been documented. In order to reliably and fully describe the generation of thermal runaway electrons by overvolted streamer tips in transient luminous events and lightning leaders, an accurate description of the differential scattering cross section at high electron energies must be established.

[119] 4. A probable scenario of events in which non-relativistic thermal runaway electrons emitted from the tips of streamers in the streamer zones of lightning leaders can be accelerated to relativistic energies is presented. With total potential differences on the order of tens of MV available in streamer zones of lightning leaders, it is proposed that during a highly transient negative corona flash stage of the development of negative stepped leader, electrons with energies 2–8 keV ejected from streamer tips near the leader head can be further accelerated to energies of hundreds of keV and possibly to several tens of MeV, depending on particular magnitude of the leader head potential. It is proposed that these energetic electrons may be responsible (through the bremsstrahlung process) for the generation of hard X-rays observed from ground and satellites preceding lightning discharges, or with no association with lightning discharges in cases when the leader process does not culminate in a return stroke [e.g., Fishman et al., 1994; Inan et al., 1996; Moore et al., 2001; Dwyer et al., 2005; Smith et al., 2005; Cummer et al., 2005, and references therein]. For a lightning leader carrying a current of 100 A, an initial flux of  $\sim 2\text{--}8$  keV thermal runaway

electrons integrated over the cross-sectional area of the leader is estimated to be  $10^{18} \text{ s}^{-1}$ , with the number of electrons accelerated to relativistic energies depending on the particular field magnitude and configuration in the leader streamer zone during the negative corona flash stage of the leader development. The duration of the negative corona flash and associated energetic radiation is estimated to be in the range from  $\sim 1 \mu\text{s}$  to  $\sim 1 \text{ms}$  depending mostly on the pressure dependent size of the leader streamer zone.

[120] **Acknowledgments.** This research was supported by the National Science Foundation under grant ATM-0134838 to the Pennsylvania State University. We also thank two reviewers for many useful comments and suggestions.

[121] Arthur Richmond thanks Joseph R. Dwyer and Davis Sentman for their assistance in evaluating this paper.

## References

- Aleksandrov, N. L., A. E. Bazelyan, E. M. Bazelyan, and I. V. Kochetov (1995), Modeling of long streamers in atmospheric-pressure air, *Plasma Phys. Rep.*, 21(1), 57–75.
- Arrayas, M., U. Ebert, and W. Hundsdorfer (2002), Spontaneous branching of anode-directed streamers between planar electrodes, *Phys. Rev. Lett.*, 88, 174502, doi:10.1103/PhysRevLett.88.174502.
- Babich, L. P. (1982), A new type of ionization wave and the mechanism of polarization self-acceleration of electrons in gas discharges at high overvoltages, *Sov. Phys. Dokl.*, 263, 76–79.
- Bakhov, K. I., L. P. Babich, and I. M. Kutsyk (2000), Temporal characteristics of runaway electrons in electron-neutral collision-dominated plasma of dense gases: Monte Carlo calculations, *IEEE Trans. Plasma Sci.*, 28(4), 1254–1262.
- Bazelyan, E. M., and Y. P. Raizer (1998), *Spark Discharge*, Chem. Rubber Co., New York.
- Bazelyan, E. M., and Y. P. Raizer (2000), *Lightning Physics and Lightning Protection*, IOP Publ., Philadelphia, Pa.
- Birdsall, C. K., and A. B. Langdon (1991), *Plasma Physics via Computer Simulation*, IOP Publ., Philadelphia, Pa.
- Blaauw, H. J., R. W. Wagenaar, D. H. Barends, and F. J. de Heer (1980), Total cross sections for electron scattering from N<sub>2</sub> and He, *J. Phys. B*, 13, 359–376, doi:10.1088/0022-3700/13/2/023.
- Chen, F. F. (1984), *Introduction to Plasma Physics and Controlled Fusion*, vol. 1, *Plasma Physics*, Springer, New York.
- Cummer, S. A., Y. Zhai, W. Hu, D. M. Smith, L. I. Lopez, and M. A. Stanley (2005), Measurements and implications of the relationship between lightning and terrestrial gamma ray flashes, *Geophys. Res. Lett.*, 32, L08811, doi:10.1029/2005GL022778.
- Dababneh, M. S., Y. F. Hsieh, W. E. Kaupilla, C. K. Kwan, S. J. Smith, T. S. Stein, and M. N. Uddin (1988), Total-cross-section measurements for positron and electron scattering by O<sub>2</sub>, CH<sub>4</sub> and SF<sub>6</sub>, *Phys. Rev. A*, 38, 1207–1216, doi:10.1103/PhysRevA.38.1207.
- Davies, D. K. (1983), Measurements of swarm parameters in dry air, *Theor. Note 346*, Westinghouse Res. and Dev. Cent., Pittsburgh, Pa.
- Dhali, S. K., and P. F. Williams (1987), Two-dimensional studies of streamers in gases, *J. Appl. Phys.*, 62(12), 4696–4707, doi:10.1063/1.339020.
- Dincer, M. S., and G. R. Govinda Raju (1983), Monte Carlo simulation of electrons in SF<sub>6</sub> in uniform electric fields, *J. Appl. Phys.*, 54(11), 6311–6316, doi:10.1063/1.331904.
- DuBois, R. D., and M. E. Rudd (1976), Differential cross sections for elastic scattering of electrons from argon, neon, nitrogen, and carbon monoxide, *J. Phys. B*, 9, 2657–2667, doi:10.1088/0022-3700/9/15/016.
- Dwyer, J. R. (2003), A fundamental limit on electric fields in air, *Geophys. Res. Lett.*, 30(20), 2055, doi:10.1029/2003GL017781.
- Dwyer, J. R. (2005a), A bolt out of the blue, *Sci. Am.*, 292(5), 64–71.
- Dwyer, J. R. (2005b), Gamma-ray events from thunderclouds, paper presented at 2005 Seminar Series on Terrestrial Gamma Ray Flashes and Lightning Associated Phenomena, Space Science Lab., Univ. of Calif., Berkeley, Calif.
- Dwyer, J. R., et al. (2003), Energetic radiation during rocket-triggered lightning, *Science*, 299(5607), 694–697, doi:10.1126/science.1078940.
- Dwyer, J. R., et al. (2004a), Measurements of X-ray emission from rocket-triggered lightning, *Geophys. Res. Lett.*, 31, L05118, doi:10.1029/2003GL018770.
- Dwyer, J. R., et al. (2004b), A ground level gamma-ray burst observed in association with rocket-triggered lightning, *Geophys. Res. Lett.*, 31, L05119, doi:10.1029/2003GL018771.

- Dwyer, J. R., et al. (2005), X-ray bursts associated with leader steps in cloud-to-ground lightning, *Geophys. Res. Lett.*, *32*, L01803, doi:10.1029/2004GL021782.
- Dyakonov, M. I., and V. Y. Kachorovskii (1989), Streamer discharge in a homogeneous field, *Sov. Phys. JETP. Engl. Transl.*, *68*, 1070–1074.
- Fishman, G. J., et al. (1994), Discovery of intense gamma-ray flashes of atmospheric origin, *Science*, *264*(5163), 1313.
- Fukunishi, H., Y. Takahashi, M. Kubota, K. Sakanoi, U. S. Inan, and W. A. Lyons (1996), Elves: Lightning-induced transient luminous events in the lower ionosphere, *Geophys. Res. Lett.*, *23*(16), 2157–2160.
- Gallimberti, I., G. Bacchiega, A. Bondiou-Clergerie, and P. Lalande (2002), Fundamental processes in long air gap discharges, *Comput. Rend. Phys.*, *3*, 1335–1359.
- Garcia, G., A. Perez, and J. Campos (1988), Total cross sections for electron scattering from N<sub>2</sub> in the energy range 600–5000 eV, *Phys. Rev. A*, *38*, 654–657, doi:10.1103/PhysRevA.38.654.
- Gerken, E. A., and U. S. Inan (2005), Streamers and diffuse glow observed in upper atmospheric electrical discharges, *IEEE Trans. Plasma Sci.*, *33*(2), 282–283, doi:10.1109/TPS.2005.845010.
- Gurevich, A. V. (1961), On the theory of runaway electrons, *Sov. Phys. JETP*, *12*, 904–912.
- Gurevich, A. V., and K. P. Zybin (2001), Runaway breakdown and electric discharges in thunderstorms, *Physics-Uspeski*, *44*(11), 1119–1140.
- Gurevich, A. V., and K. P. Zybin (2005), Runaway breakdown and the mysteries of lightning, *Phys. Today*, *58*(5), 37–43, doi:10.1063/1.1995746.
- Gurevich, A. V., G. M. Milikh, and R. A. Roussel-Dupre (1992), Runaway electron mechanism of air breakdown and preconditioning during a thunderstorm, *Phys. Lett. A*, *165*(5–6), 463–468, doi:10.1016/0375-9601(92)90348-P.
- Iga, I., L. Mu-Tao, J. C. Nogueira, and R. S. Barbieri (1987), Elastic differential cross measurements for electron scattering from Ar and O<sub>2</sub> in the intermediate energy range, *J. Phys. B*, *20*(5), 1095–1104, doi:10.1088/0022-3700/20/5/025.
- Inan, U. S., V. P. Pasko, and T. F. Bell (1996), Sustained heating of the ionosphere above thunderstorms as evidenced in “early/fast” VLF events, *Geophys. Res. Lett.*, *23*(10), 1067–1070.
- Inan, U. S., C. Barrington-Leigh, S. Hansen, V. S. Glukhov, T. F. Bell, and R. Rairden (1997), Rapid lateral expansion of optical luminosity in lightning-induced ionospheric flashes referred to as elves, *Geophys. Res. Lett.*, *24*(5), 583–586, doi:10.1029/97GL00404.
- International Commission on Radiation Units and Measurements (1984), Stopping powers for electrons and positrons, tables 8.1 and 12.4, *ICRU Rep. 37*, Bethesda, Md.
- Jain, A., and K. L. Baluja (1992), Total (elastic plus inelastic) cross sections for electron scattering from diatomic and polyatomic molecules at 10–5000 eV: H<sub>2</sub>, Li<sub>2</sub>, HF, CH<sub>4</sub>, N<sub>2</sub>, CO, C<sub>2</sub>H<sub>2</sub>, HCN, O<sub>2</sub>, HCl, H<sub>2</sub>S, PH<sub>3</sub>, SiH<sub>4</sub>, and CO<sub>2</sub>, *Phys. Rev. A*, *45*, 202–218, doi:10.1103/PhysRevA.45.202.
- Kambara, H., and K. Kuchitsu (1972), Measurement of differential cross sections of low-energy electrons elastically scattered by gas molecules, I. Apparatus, *Jpn. J. Appl. Phys.*, *11*(5), 609–616.
- Karwasz, G. P., M. Barozzi, R. S. Brusa, and A. Zecca (2002), Total cross sections for positron scattering on argon and krypton at intermediate and high energies, *Nucl. Instrum. Methods Phys. Res., Sect. B*, *192*(1–2), 157–161.
- Kol’chuzhkin, A. M., and V. V. Uchaikin (1978), *Introduction to the Theory of Charged Particle Transport Through the Matter*, Atomizdat, Moscow.
- Kunhardt, E. E., and Y. Tzeng (1986a), Role of electron-molecule angular scattering in shaping the electron-velocity distribution, *Phys. Rev. A*, *34*, 2158–2166, doi:10.1103/PhysRevA.34.2158.
- Kunhardt, E. E., and Y. Tzeng (1986b), Monte Carlo technique for simulating the evolution of an assembly of particles increasing in number, *J. Comput. Phys.*, *67*, 279–289.
- Kunhardt, E. E., Y. Tzeng, and J. P. Boeuf (1986), Stochastic development of an electron avalanche, *Phys. Rev. A*, *34*, 440–449, doi:10.1103/PhysRevA.34.440.
- Lawton, S. A., and A. V. Phelps (1978), Excitation of the  $b^1\Sigma_g^+$  state of O<sub>2</sub> by low-energy electrons, *J. Chem. Phys.*, *69*(3), 1055–1068, doi:10.1063/1.436700.
- Lehtinen, N. G., T. F. Bell, and U. S. Inan (1999), Monte Carlo simulation of runaway MeV electron breakdown with application to red sprites and terrestrial gamma ray flashes, *J. Geophys. Res.*, *104*(A11), 24,699–24,712, doi:10.1029/1999JA900335.
- Lieberman, M. A., and A. J. Lichtenberg (1994), *Principles of Plasma Discharges and Materials Processing*, John Wiley, Hoboken, N. J.
- Lin, S. L., and J. N. Bardsley (1977), Monte Carlo simulation of ion motion in drift tubes, *J. Chem. Phys.*, *66*(2), 435–445, doi:10.1063/1.433988.
- Liu, J., and G. R. Govinda Raju (1992), Monte Carlo simulation of electron motion in mercury vapour, *J. Phys. D*, *25*, 167–172, doi:10.1088/0022-3727/25/2/006.
- Liu, N., and V. P. Pasko (2004), Effects of photoionization on propagation and branching of positive and negative streamers in sprites, *J. Geophys. Res.*, *109*, A04301, doi:10.1029/2003JA010064.
- Lyons, W. A. (1996), Sprite observations above the US High Plains, in relation to their parent thunderstorm systems, *J. Geophys. Res.*, *101*(D23), 29,641–29,652.
- Lyons, W. A., T. E. Nelson, R. A. Armstrong, V. P. Pasko, and M. A. Stanley (2003), Upward electrical discharges from thunderstorm tops, *Bull. Am. Meteorol. Soc.*, *84*(4), 445–454, doi:10.1175/BAMS-84-4-445.
- Marshall, R. A., and U. S. Inan (2005), High-speed telescopic imaging of sprites, *Geophys. Res. Lett.*, *32*(5), L05804, doi:10.1029/2004GL021988.
- Marshall, T. C., M. P. McCarthy, and W. D. Rust (1995), Electric-field magnitudes and lightning initiation in thunderstorms, *J. Geophys. Res.*, *100*(D4), 7097–7104.
- Marshall, T. C., M. Stolzenburg, and W. D. Rust (1996), Electric field measurements above mesoscale convective systems, *J. Geophys. Res.*, *101*(D3), 6979–6996.
- Marshall, T. C., M. Stolzenburg, W. D. Rust, E. R. Williams, and R. Boldi (2001), Positive charge in the stratiform cloud of a mesoscale convective system, *J. Geophys. Res.*, *106*(D1), 1157–1164.
- Marshall, T. C., M. Stolzenburg, C. R. Maggio, L. M. Coleman, P. R. Krehbiel, T. Hamlin, R. J. Thomas, and W. Rison (2005), Observed electric fields associated with lightning initiation, *Geophys. Res. Lett.*, *32*(3), L03813, doi:10.1029/2004GL021802.
- McHarg, M. G., R. K. Haaland, D. R. Moudry, and H. C. Stenbaek-Nielson (2002), Altitude-time development of sprites, *J. Geophys. Res.*, *107*(A11), 1364, doi:10.1029/2001JA000283.
- Moore, C. B., K. B. Eack, G. D. Aulich, and W. Rison (2001), Energetic radiation associated with lightning stepped-leaders, *Geophys. Res. Lett.*, *28*(11), 2141–2144.
- Morgan, W. L., and B. M. Penetrante (1990), ELENDF: A timedependent Boltzmann solver for partially ionized plasmas, *Comput. Phys. Comm.*, *58*(1–2), 127–152, doi:10.1016/0010-4655(90)90141-M.
- Morrow, R., and J. J. Lowke (1997), Streamer propagation in air, *J. Phys. D*, *30*, 614–627, doi:10.1088/0022-3727/30/4/017.
- Moudry, D. R., H. C. Stenbaek-Nielson, D. D. Sentman, and E. M. Wescott (2002), Velocities of sprite tendrils, *Geophys. Res. Lett.*, *29*(X), 1992, doi:10.1029/2002GL015682.
- Moudry, D. R., H. C. Stenbaek-Nielson, D. D. Sentman, and E. M. Wescott (2003), Imaging of elves, halos, and sprite initiation at 1 ms time resolution, *J. Atmos. Solar Terr. Phys.*, *65*(5), 509–518.
- Opal, C. B., W. K. Peterson, and E. C. Beaty (1971), Measurements of secondary-electron spectra produced by electron impact ionization of a number of simple gases, *J. Chem. Phys.*, *55*(8), 4100–4106.
- Pasko, V. P. (2006), Theoretical modeling of sprites and jets, in *NATO Advanced Study Institute on Sprites, Elves and Intense Lightning Discharges*, Springer, New York.
- Pasko, V. P., M. A. Stanley, J. D. Mathews, U. S. Inan, and T. G. Wood (2002), Electrical discharge from a thundercloud top to the lower ionosphere, *Nature*, *416*(6877), 152–154.
- Perkins, S. T., and D. E. Cullen (1994), ENDL type formats for the LLNL evaluated atomic data library, EADL, for the evaluated electron data library, EEDL, and for the evaluated photon library EPDL, LLNL, UCRL-ID-117796, sponsor?, Livermore, Calif.
- Phelps, A. V., and L. C. Pitchford (1985), Anisotropic scattering of electrons by N<sub>2</sub> and its effect on electron transport, *Phys. Rev. A*, *31*(5), 2932–2949, doi:10.1103/PhysRevA.31.2932.
- Raizer, Y. P. (1991), *Gas Discharge Physics*, Springer, New York.
- Rocco, A., U. Ebert, and W. Hundsdorfer (2002), Branching of negative streamers in free flight, *Phys. Rev. E*, *66*, 035102 (R), doi:10.1103/PhysRevE.66.035102.
- Roussel-Dupre, R. A., A. V. Gurevich, T. Tunnel, and G. M. Milikh (1994), Kinetic theory of runaway breakdown, *Phys. Rev. E*, *49*(3), 2257–2271, doi:10.1103/PhysRevE.49.2257.
- Sentman, D. D., E. M. Wescott, D. L. Osborne, D. L. Hampton, and M. J. Heavner (1995), Preliminary results from Sprites94 campaign: Red sprites, *Geophys. Res. Lett.*, *22*(10), 1205–1208.
- Shveigert, V. A. (1990), Evolution of the electron-distribution function in strong electric-fields (in Russian), *High Temp.*, *28*, 35–39.
- Shyn, T. W., and W. E. Sharp (1982), Angular distribution of electrons elastically scattered from O<sub>2</sub>: 2.0–200 eV impact energy, *Phys. Rev. A*, *26*(3), 1369–1372, doi:10.1103/PhysRevA.26.1369.
- Shyn, T. W., R. S. Stolarski, and G. R. Carignan (1972), Angular distribution of electrons elastically scattered from N<sub>2</sub>, *Phys. Rev. A*, *6*(3), 1002–1012, doi:10.1103/PhysRevA.6.1002.

- Smith, D. M., L. I. Lopez, R. P. Lin, and C. P. Barrington-Leigh (2005), Terrestrial gamma-ray flashes observed up to 20 MeV, *Science*, 307(5712), 1085–1088, doi:10.1126/science.1107466.
- Srivastava, S. K., H. Tanaka, A. Chutjian, and S. Trajmar (1981), Elastic scattering of intermediate-energy electrons by Ar and Kr, *Phys. Rev. A*, 23, 2156–2166, doi:10.1103/PhysRevA.23.2156.
- Stanley, M., P. Krehbiel, M. Brook, C. Moore, W. Rison, and B. Abrahams (1999), High speed video of initial sprite development, *Geophys. Res. Lett.*, 26(20), 3201–3204.
- Su, H. T., R. R. Hsu, A. B. Chen, Y. C. Wang, W. S. Hsiao, W. C. Lai, L. C. Lee, M. Sato, and H. Fukunishi (2003), Gigantic jets between a thundercloud and the ionosphere, *Nature*, 423(6943), 974–976.
- Surendra, M., D. B. Graves, and G. M. Jellum (1990), Self-consistent model of a direct-current glow discharge: Treatment of fast electrons, *Phys. Rev. A*, 41(2), 1112–1125, doi:10.1103/PhysRevA.41.1112.
- Szmytkowski, C., K. Maciag, and G. Karwasz (1996), Absolute electron-scattering total cross section measurements for noble gas atoms and diatomic molecules, *Phys. Scr.*, 54, 271–280.
- Thomas, W. R. L. (1969), The determination of the total excitation cross section in neon by comparison of theoretical and experimental values of Townsend's primary ionization coefficient, *J. Phys. B*, 2(5), 551–561, doi:10.1088/0022-3700/2/5/308.
- Tzeng, Y., and E. E. Kunhardt (1986), Effect of energy partition in ionizing collisions on the electron-velocity distribution, *Phys. Rev. A*, 34(3), 2148–2157, doi:10.1103/PhysRevA.34.2148.
- Uman, M. A. (2001), *The Lightning Discharge*, Dover, Mineola, N. Y.
- Van Zyl, B., and W. Pendleton Jr. (1995),  $N_2^+$  (X),  $N_2^+$  (A), and  $N_2^+$  (B) production in  $e^- + N_2$  collisions, *J. Geophys. Res.*, 100(A12), 23,755–23,762.
- Vitello, P. A., B. M. Penetrante, and J. N. Bardsley (1994), Simulation of negative-streamer dynamics in nitrogen, *Phys. Rev. E*, 49(6), 5574–5598, doi:10.1103/PhysRevE.49.5574.
- Wescott, E. M., D. Sentman, D. Osbourne, H. Hampton, and M. Heavner (1995), Preliminary results from the Sprites94 aircraft campaign: 2. Blue jets, *Geophys. Res. Lett.*, 22(10), 1209–1212.
- Wescott, E. M., D. D. Sentman, H. C. Stenbaek-Nielson, P. Huet, M. J. Heavner, and D. R. Moudry (2001), New evidence for the brightness and ionization of blue starters and blue jets, *J. Geophys. Res.*, 106(A10), 21,549–21,554.
- Williams, J. F., and B. A. Willis (1975), The scattering of electrons from inert gases. I. Absolute differential elastic cross sections for argon atoms, *J. Phys. B*, 8(10), 1670–1682, doi:10.1088/0022-3700/8/10/017.
- Yamabe, C., S. J. Buckman, and A. V. Phelps (1983), Measurement of free-free emission from low-energy-electron collisions with Ar, *Phys. Rev. A*, 27(3), 1345–1352, doi:10.1103/PhysRevA.27.1345.

---

N. Liu, G. D. Moss, and V. P. Pasko, Department of Electrical Engineering, Communications and Space Sciences Laboratory, Pennsylvania State University, 204 Electrical Engineering East, University Park, PA 16802, USA. (nul105@psu.edu; gdm131@psu.edu; vpasko@psu.edu)  
 G. Veronis, Ginzton Laboratory, AP 124, Stanford, CA 94305, USA. (gveronis@stanford.edu)